

# ANATOMY OF QCD STRINGS AND SATURATION EFFECTS IN HIGH-ENERGY SCATTERING

Dissertation

submitted to the

Combined Faculties for the Natural Sciences and for Mathematics  
of the Ruperto-Carola University of Heidelberg, Germany

for the degree of  
Doctor of Natural Sciences

presented by

**ARIF SHOSHI**

born in Scheßlitz, Germany

Referees: Prof. Dr. Hans-Jürgen Pirner  
Prof. Dr. Jörg Hüfner

Oral examination: February 13, 2003

## Zusammenfassung

Wir erstellen ein Modell, um Hochenergiereaktionen von Hadronen und Photonen zu berechnen. Der Gluon-Austausch beschreibt die perturbative und das Modell des Stochastischen Vakuums die nichtperturbative Wechselwirkung. Letzteres führt zum Quark-Confinement in Dipolen via eines Strings von Farbfeldern. Wir erforschen die QCD-Struktur der Dipol-Dipol Wechselwirkung im Impulsraum, vor allem die Wechselwirkung zwischen den Strings. Wir stellen den String als eine Ansammlung von stringlosen Dipoles dar, zeigen Confinement-Effekte in der Hochenergiestreuung und berechnen die unintegrierte Gluonverteilung von Hadronen und Photonen. Im Stoßparameterraum des Streuprozesses untersuchen wir das Unitaritätslimit der  $S$ -matrix. Wir berechnen die Stoßparameter-Profile der Hadron-Hadron und Photon-Hadron Streuung, bestimmen die Energiewerte bei welchen die Profile das Black-Disc-Limit erreichen, schätzen die stoßparameterabhängige Gluonverteilung des Protons ab und diskutieren die Gluonsättigung. Wir vergleichen die Resultate des Modells für  $pp$ ,  $\pi p$ ,  $Kp$ ,  $\gamma^*p$  und  $\gamma\gamma$  Reaktionen mit experimentellen Daten und identifizieren Sättigungseffekte in experimentellen Messgrößen.

## Abstract

We develop a model to compute high-energy reactions of hadrons and photons. The perturbative interaction is described by gluon exchange and the non-perturbative interaction by the stochastic vacuum model which leads to quark-confinement in dipoles via a string of color fields. We study the QCD structure of the dipole-dipole scattering in momentum space focussing especially on interactions between strings. We represent the string as a collection of stringless dipoles, show confinement effects in high-energy scattering and calculate unintegrated gluon distributions of hadrons and photons. In the impact parameter space of the scattering process we investigate the unitarity limit of the  $S$ -matrix. We calculate the impact parameter profiles for proton-proton and photon-proton scattering, determine the energy values at which the profiles saturate at the black disc limit, estimate the impact parameter dependent gluon distribution of the proton and discuss gluon saturation. We compare the model results for  $pp$ ,  $\pi p$ ,  $Kp$ ,  $\gamma^*p$  and  $\gamma\gamma$  reactions with experimental data and identify saturation effects in experimental observables.

# Contents

<b>1</b>	<b>Introduction</b>	<b>1</b>
<b>2</b>	<b>The Loop-Loop Correlation Model</b>	<b>7</b>
2.1	Functional Integral Approach to High-Energy Scattering . . . . .	7
2.2	Vacuum Expectation Value of one Wegner-Wilson Loop . . . . .	11
2.3	The Loop-Loop Correlation Function . . . . .	13
2.4	Perturbative and Non-Perturbative QCD Components . . . . .	17
2.5	Evaluation of the $\chi$ -Function with Minimal Surfaces . . . . .	22
2.6	Energy Dependence . . . . .	28
2.7	Model Parameters . . . . .	31
<b>3</b>	<b>Anatomy of QCD Strings and Unintegrated Gluon Distributions</b>	<b>33</b>
3.1	QCD Structure of Dipole-Dipole Scattering in Momentum Space . .	34
3.2	Decomposition of the QCD String into Dipoles and Unintegrated Gluon Distributions . . . . .	42
3.3	Numerical Results for Unintegrated Gluon Distributions in Hadrons and Photons . . . . .	47
3.4	Comparison with Other Work . . . . .	55

<b>4 Impact Parameter Profiles and Gluon Saturation</b>	<b>61</b>
4.1 <i>S</i> -Matrix Unitarity and Impact Parameter Profiles . . . . .	62
4.2 Profile Function for Hadron-Hadron Scattering . . . . .	63
4.3 Profile Function for Photon-Proton Scattering . . . . .	68
4.4 A Scenario for Gluon Saturation . . . . .	72
<b>5 Comparison with Data and Saturation Effects in Observables</b>	<b>77</b>
5.1 Total Cross Sections . . . . .	78
5.2 Proton Structure Function . . . . .	81
5.3 Slope Parameter $B$ of Elastic Forward Scattering . . . . .	85
5.4 Differential Elastic Cross Sections . . . . .	87
5.5 Elastic Cross Sections $\sigma^{el}$ , $\sigma^{el}/\sigma^{tot}$ , and $\sigma^{tot}/B$ . . . . .	91
<b>6 Conclusions and Outlook</b>	<b>95</b>
<b>A Conventions</b>	<b>101</b>
A.1 Units . . . . .	101
A.2 Lorentz Vectors . . . . .	101
A.3 Light-Cone Coordinates . . . . .	102
<b>B Wave Functions</b>	<b>103</b>
B.1 Hadron Wave Function . . . . .	103
B.2 Photon Wave Function . . . . .	104
<b>C Correlation Functions</b>	<b>107</b>
<b>D Non-Forward <i>T</i>-Matrix Element</b>	<b>109</b>

# Chapter 1

## Introduction

On the basis of the numerous tests in experiments, one can confidently say that Quantum Chromodynamics (QCD) is the correct theory of strong interactions. The asymptotic freedom of QCD has allowed us to understand the interaction of particles at high momentum transfers. The non-Abelian nature of QCD leading to color confinement prevents first-principle calculations of hadronic interactions in the non-perturbative region. In fact, it is a key issue in high-energy physics to understand and describe the non-perturbative structure of hadronic scattering processes. The unravelling of confinement effects in such interactions would be especially important.

So far Lattice Gauge Theory [1] constitutes the only access to non-perturbative QCD physics from first principles. Numerical simulations of QCD on Euclidean lattices [2] give strong evidence not only for color confinement but also for chiral symmetry breaking and dynamical mass generation from the QCD Lagrangian. Unfortunately, lattice QCD cannot be applied in Minkowskian space-time to simulate high-energy reactions since it is limited to the Euclidean formulation of QCD.

Experiments show a rise of high-energy total cross sections with increasing center-of-mass (c.m.) energy. The rise is slow for large-size particles (protons, pions, kaons, or real photons [3]) and becomes steep for small-size particles (highly virtual photons [4, 5] or charmonia [6]) involved in the scattering process. It is highly unsatisfactory that we do not have a genuine understanding of the growing cross sections on the basis of the QCD Lagrangian. The most rigorous result we have is the Froissart bound [7] stating that hadronic cross sections cannot grow faster than  $\ln^2(s/s_0)$  for asymptotic c.m. energies  $\sqrt{s}$ . It is derived on the basis of very general principles such as unitarity and analyticity of the scattering matrix. Its derivation, however, does not provide any physical mechanism realizing the squared logarithmic increase. At present no quantum field theoretical understanding of the rising hadron

extension at high energies is available.

It is hopelessly difficult to solve any of the mentioned problems of high-energy scattering from first principles alone. Consequently, models that approximate quantum chromodynamics are required. To be convincing, however, the proposed models should include the basic features of QCD, reproduce many experimental high-energy data and agree with lattice QCD simulations.

In this work we develop a model to describe the high-energy scattering of hadrons and photons in the eikonal approximation [8]. Its central element is the gauge-invariant light-like *Wegner-Wilson loop*  $W_r[C]$  with the boundary  $C$  and the representation  $r$  of  $SU(N_c)$  [1, 9]. The scattering amplitude factorizes into the vacuum expectation value of two correlated Wegner-Wilson loops  $\langle W_{r_1}[C_1]W_{r_2}[C_2] \rangle$  and reaction-specific wave functions [10–13]. The Wegner-Wilson loops describe the path of color-dipoles and the *loop-loop correlation function*  $\langle W_{r_1}[C_1]W_{r_2}[C_2] \rangle$  the dipole-dipole scattering. The most interesting are Wegner-Wilson loops in the fundamental and adjoint representation of  $SU(3)$  which represent color-singlet quark-antiquark dipoles and glueballs (adjoint dipoles), respectively. In our framework color-dipoles are given by the quark and antiquark in mesons or photons and in a simplified picture by a quark and diquark in baryons. The size and orientation of the color-dipoles in the hadrons and photons are determined by appropriate light-cone wave functions. In this sense the loop-loop correlation function constitutes the basis for a unified description of hadrons and photons.

We evaluate the loop-loop correlation function  $\langle W_{r_1}[C_1]W_{r_2}[C_2] \rangle$  in the approach of Berger and Nachtmann [14] which resumes gluonic exchanges in the scattering process using a matrix cumulant expansion and the Gaussian approximation of the functional integrals in the gluon field strengths. The resummation is crucial to guarantee the  $S$ -matrix unitarity and to investigate saturation effects in high-energy reactions. In addition to the interaction of two dipoles in the fundamental representation of  $SU(3)$  considered by Berger and Nachtmann [14], we compute also the interaction of a fundamental with an adjoint dipole in the representation of  $SU(N_c)$ .

We express the loop-loop correlation function  $\langle W_{r_1}[C_1]W_{r_2}[C_2] \rangle$  in terms of the bilocal gluon field strength correlators integrated over two connected surfaces. The surfaces enter by using the non-Abelian Stokes' theorem [11, 15] to transform the line integrals over the gluon potentials in the Wegner-Wilson loops of the functional integral approach [10–13] into surface integrals over gluon field strengths. We use for the first time explicitly *minimal surfaces*, i.e., planar surfaces bounded by the Wegner-Wilson loops. In Euclidean space-time, this surface choice is usually used to obtain Wilson's area law [16]. We have recently shown that minimal surfaces are actually required to ensure the consistency of our results for  $\langle W_r[C] \rangle$  and

$\langle W_{r_1}[C_1]W_{r_2}[C_2] \rangle$  by using low-energy theorems [17]. The simplicity of the minimal surfaces is appealing: It allows us to show for the first time the analytic structure of non-perturbative interactions in momentum space. The previous pyramid mantle choice for the surfaces [13, 14, 18–23] did not allow such an analysis.

We use in the gluon field strength correlator perturbative and non-perturbative correlations as needed to describe interactions of small and large-size particles. The perturbative correlator results from QCD while the non-perturbative correlator is modelled by the stochastic vacuum model (SVM) [16]. This combination allows us to describe short and long distance correlations in agreement with lattice calculations of the gluon field strength correlator [24, 25]. Moreover, this two component ansatz leads to the static quark-antiquark potential with color-Coulomb behavior for small and confining linear rise for large quark-antiquark separations as expected [26].

We use in the non-perturbative correlator the *exponential correlation function* advised by lattice QCD investigations of long-distance correlations [25]. This correlation function stays positive for all Euclidean distances and, thus, is compatible with a spectral representation of the correlation function [27]. This represents a conceptual improvement since the correlation function that has been used in earlier applications of the SVM becomes negative at large distances [13, 14, 18, 20–23].

In spite of the numerous improvements our approach is still incomplete as it leads to energy-independent cross sections in contradiction to the experimental observation. This is because of the missed gluon radiation in the present model. In this work, however, the energy dependence is introduced phenomenologically. In line with the experimental observation mentioned above, we ascribe a strong and weak energy dependence, respectively, to the perturbative and non-perturbative component. Assuming the same mechanism for the energy dependence of hadron and photon interactions (motivated by the successful two-pomeron fit of Donnachie and Landshoff [28, 29]) we implement a *powerlike energy dependence* in the loop-loop correlation function  $\langle W_{r_1}[C_1]W_{r_2}[C_2] \rangle$ . In this way a unified description of the energy behaviour of hadron-hadron, photon-hadron, and photon-photon reactions is obtained. The powerlike ansatz in combination with the *multiple gluonic interactions* resulting from the resummation method of Berger and Nachtmann is crucial to guarantee the Froissart bound [7]. The phenomenological energy dependence, of course, can only be an intermediate step. For a fundamental understanding of the energy dependence of cross sections quantum evolution has to be incorporated in our model.

We adjust the model parameters to reproduce a wealth of high-energy scattering data, i.e. total, differential and elastic cross sections, structure functions and slope parameters for many different reactions over a large range of c.m. energies. In

this way we have confidence in our model predictions for future experiments (LHC, THERA) and for energies beyond the experimentally accessible range.

The non-perturbative component of our model gives confinement [16] due to flux-tube formation of color-electric fields between the color-sources in the dipole [17, 30, 31]. The thickness of flux-tubes or confining QCD strings saturates for large dipole-sizes at the value of about one Fermi [17]. The general representation  $r$  of  $SU(N_c)$  kept for all computations leads to an exact Casimir scaling for static color-dipole potentials and QCD strings [17] in agreement with lattice QCD simulations [32, 33]. In this work we show the intrinsic composition of QCD strings, the structure of string interactions, and manifestations of strings in high-energy scattering.

We show for the first time the QCD structure of the perturbative and non-perturbative dipole-dipole interaction in momentum space within our model. We reproduce the known results for perturbative interactions between the dipoles, the two-gluon exchange [34, 35], and give new insights into the non-perturbative dipole-dipole scattering process. This comes out as a sum of two parts: The first part describes the non-perturbative interaction between the quarks and antiquarks of the two dipoles and exhibits the same structure as the perturbative contribution. The second part represents the interaction between the strings of the two dipoles. The latter shows a new structure different from the perturbative two-gluon exchange.

We find an extremely nice feature for the QCD string that confines the quark and antiquark in the dipole: The QCD string of length  $|\vec{r}_D|$  can be exactly represented as an integral over stringless dipoles of sizes  $\xi|\vec{r}_D|$  with  $0 \leq \xi \leq 1$  and dipole number density  $n(\xi) = 1/\xi^2$ . This outstanding result is very similar to the perturbatively computed wave function of a  $q\bar{q}$  onium state in the large-  $N_c$  limit where the numerous emitted gluons inside the onium state are considered as dipoles [36, 37].

The decomposition of the QCD string into stringless dipoles allows us for the first time to extract the microscopic structure of the unintegrated gluon distribution of hadrons and photons  $\mathcal{F}_h(x, k_\perp^2)$  from our dipole-hadron and dipole-photon cross section via  $|\vec{k}_\perp|$ -factorization. We compare the unintegrated gluon distribution of the proton with those obtained in other approaches.

The unintegrated gluon distribution of hadrons and photons  $\mathcal{F}_h(x, k_\perp^2)$  is a basic, universal quantity convenient for the computation of many scattering observables at small  $x$ . It is crucial to describe processes in which transverse momenta are explicitly exposed such as dijet [38] or vector meson [39] production at HERA. Its explicit  $|\vec{k}_\perp|$ -dependence is particularly suited to study the interplay between soft and hard physics. Moreover, the unintegrated gluon distribution is the central object in the BFKL [40] and CCFM [41] evolution equations. Upon integration over

the transverse gluon momentum  $|\vec{k}_\perp|$  it leads to the conventional gluon distribution  $xG_h(x, Q^2)$  used in the DGLAP evolution equation [42].

We show the manifestations of the QCD string explicitly in dipole-hadron cross sections at large dipole sizes and in unintegrated gluon distributions at small transverse momenta. We find further that the  $|\vec{k}_\perp|$ -factorization which is known in perturbative physics can be extended also to non-perturbative dipole-hadron interactions within our model.

To study saturation effects that manifest the  $S$ -matrix unitarity, we investigate the scattering amplitude in impact parameter space where the  $S$ -matrix unitarity imposes the rigid black disc limit on the height of impact parameter profiles. We show explicitly that our profiles respect the black disc limit. Furthermore, the width of the impact parameter profiles is shown to increase logarithmically at asymptotic energies as needed to guarantee the Froissart bound [7].

We compute the impact parameter profiles for hadron-hadron and longitudinal photon-proton scattering for different c.m. energies. We determine the energy values at which the impact parameter profiles saturate at the black disc limit for small impact parameters. The impact parameter profiles provide an intuitive geometrical picture for the energy dependence of the scattering process as they illustrate the evolution of the size and opacity of the interacting particles with increasing energy.

We estimate the impact parameter dependent gluon distribution of the proton  $xG(x, Q^2, |\vec{b}_\perp|)$  using its relation to the impact parameter profile for longitudinal photon-proton scattering. We find a low- $x$  saturation of  $xG(x, Q^2, |\vec{b}_\perp|)$  as a manifestation of the  $S$ -matrix unitarity. Consequently, the  $x$ -dependence of the integrated gluon distribution  $xG(x, Q^2)$  slows down from a powerlike to a squared logarithmic rise in agreement with complementary investigations of gluon saturation at low  $x$ .

We compare the model results with experimental data and provide predictions for future experiments. We compute total cross sections  $\sigma^{tot}$ , the structure function of the proton  $F_2$ , slope parameters  $B$ , differential elastic cross sections  $d\sigma^{el}/dt$ , elastic cross sections  $\sigma^{el}$ , and the ratios  $\sigma^{el}/\sigma^{tot}$  and  $\sigma^{tot}/B$  for proton-proton, pion-proton, kaon-proton, photon-proton, and photon-photon reactions involving real and virtual photons as well. The successful unified description of all these reactions indicates indeed the assumed universal pomeron contribution to the above reactions.

Making use of the explicit saturation of the impact parameter profiles at the black disc limit, the energy values at which it is reached, and the logarithmic rise of the black disc radius, we show explicitly manifestations of  $S$ -matrix unitarity limits in experimental observables. A squared logarithmic behavior of total cross sections of hadrons and photons is found to set in for c.m. energies  $\sqrt{s} \geq 10^6$  GeV. The

ratios  $\sigma^{el}/\sigma^{tot}$  and  $\sigma^{tot}/B$  become universal for such energies, i.e., independent of the hadron species considered. For asymptotic energies, also the total hadronic cross sections become universal and increase in agreement with the Froissart bound [7].

The outline of the work is as follows: In chapter 2 we present the model and give the model parameters. In transverse momentum space considered in chapter 3 we show the structure of QCD string interactions, decompose the string into stringless dipoles, elaborate the total dipole-hadron cross section, and extract the unintegrated gluon distribution. We compare the latter with ones obtained from other approaches and use it also to compute the integrated gluon distribution of the proton. In impact parameter space investigated in chapter 4 we study the  $S$ -matrix unitarity limits, calculate the impact parameter profiles for proton-proton and photon-proton scattering, determine the energy values at which the profiles saturate at the black disc limit, estimate the impact parameter dependent gluon distribution of the proton, and discuss gluon saturation. Finally, in chapter 5 we compare the model results with experimental data and identify saturation effects in experimental observables. The appendices contain conventions, hadron and photon wave functions, the analytic continuation of the non-perturbative correlation functions from Euclidean to Minkowski space-time, and the non-forward scattering amplitude.

# Chapter 2

## The Loop-Loop Correlation Model

In this chapter we present the loop-loop correlation model. We describe briefly the functional integral approach to high-energy scattering in the eikonal approximation and compute in detail the expectation value of one Wegner-Wilson loop and the correlation of two Wegner-Wilson loops within a Gaussian approximation in the gluon field strengths. Perturbative dipole-dipole interactions (long-distance correlations) are described by perturbative gluon exchange and non-perturbative dipole-dipole interactions (short-distance correlations) are modelled by the stochastic vacuum model (SVM) [16]. We use the minimal surfaces to calculate the  $S$ -matrix element. Finally, we introduce the energy dependence in a phenomenological way and specify the parameter values.

### 2.1 Functional Integral Approach to High-Energy Scattering

The  $T$ -matrix is the central quantity in scattering processes. It enters every observable we intend to look at and is obtained from the  $S$ -matrix by subtracting the trivial case in which the final state equals the initial state,

$$S_{fi} = \delta_{fi} + i(2\pi)^4 \delta^4(P_f - P_i) T_{fi} , \quad (2.1.1)$$

where  $P_i$  and  $P_f$  represent the sum of incoming and outgoing momenta, respectively. Based on the functional integral approach to high-energy loop-loop scattering in the eikonal approximation [10–13], the  $T$ -matrix element for the reaction  $ab \rightarrow cd$  at

transverse momentum transfer  $\vec{q}_\perp$  ( $t = -\vec{q}_\perp^2$ ) and c.m. energy squared  $s$  reads

$$T_{ab \rightarrow cd}(s, t) = 2is \int d^2 b_\perp e^{i\vec{q}_\perp \cdot \vec{b}_\perp} \int dz_1 d^2 r_1 \int dz_2 d^2 r_2 \times \psi_c^*(z_1, \vec{r}_1) \psi_d^*(z_2, \vec{r}_2) \left[ 1 - S_{r_1 r_2}(s, \vec{b}_\perp, z_1, \vec{r}_1, z_2, \vec{r}_2) \right] \psi_a(z_1, \vec{r}_1) \psi_b(z_2, \vec{r}_2) , \quad (2.1.2)$$

with the  $S_{r_1 r_2}$  matrix element

$$S_{r_1 r_2}(s, \vec{b}_\perp, z_1, \vec{r}_1, z_2, \vec{r}_2) = \frac{\left\langle W_{r_1}[C_1] W_{r_2}[C_2] \right\rangle_G}{\left\langle W_{r_1}[C_1] \right\rangle_G \left\langle W_{r_2}[C_2] \right\rangle_G} . \quad (2.1.3)$$

The crucial quantity in (2.1.3) is the light-like QCD Wegner-Wilson loop [1, 9]

$$W_r[C] = \tilde{\text{Tr}}_r \mathcal{P} \exp \left[ -ig \oint_C dz^\mu \mathcal{G}_\mu^a(z) t_r^a \right] , \quad (2.1.4)$$

where the subscript  $r$  indicates a representation of  $SU(N_c)$ ,  $N_c$  is the number of colors,  $\tilde{\text{Tr}}_r = \text{Tr}_r(\cdots)/\text{Tr} \mathbb{1}_r$  is the normalized trace in the corresponding color-space with unit element  $\mathbb{1}_r$ ,  $g$  is the strong coupling, and  $\mathcal{G}_\mu(z) = \mathcal{G}_\mu^a(z) t_r^a$  represents the gluon field with the  $SU(N_c)$  group generators in the corresponding representation,  $t_r^a$ , that demand the path ordering indicated by  $\mathcal{P}$  on the closed path  $C$  in space-time. A distinguishing theoretical feature of the Wegner-Wilson loop is its invariance under local gauge transformations in color-space. Therefore, it is the basic object in lattice gauge theories [1, 2, 9] and has been considered as the fundamental building block for a gauge theory in terms of gauge invariant variables [43]. Physically, the Wegner-Wilson loop represents the phase factor acquired by a color-charge in the  $SU(N_c)$  representation  $r$  along the light-like trajectory  $C$  in the background field. In other words, the Wegner-Wilson loop describes a color-singlet dipole in the representation  $r$  of  $SU(N_c)$ .

Wegner-Wilson loops in the fundamental representation of  $SU(N_c = 3)$  are especially important since they represent color-singlet quark-antiquark dipoles. In this representation, the  $S_{r_1 r_2}$  matrix element (2.1.3) describes the elastic scattering of two quark-antiquark dipoles with transverse size and orientation  $\vec{r}_i$ . The longitudinal momentum fraction of color-dipole  $i$  carried by the quark is  $z_i$ . The impact parameter between the dipoles is [19]

$$\vec{b}_\perp = \vec{r}_{1q} + (1 - z_1) \vec{r}_1 - \vec{r}_{2q} - (1 - z_2) \vec{r}_2 = \vec{r}_{1cm} - \vec{r}_{2cm} , \quad (2.1.5)$$

where  $\vec{r}_{iq}$  ( $\vec{r}_{i\bar{q}}$ ) is the transverse position of the quark (antiquark),  $\vec{r}_i = \vec{r}_{i\bar{q}} - \vec{r}_{iq}$ , and  $\vec{r}_{icm} = z_i \vec{r}_{iq} + (1 - z_i) \vec{r}_{i\bar{q}}$  is the center of light-cone momenta. In the eikonal

approximation to high-energy scattering the  $q$  and  $\bar{q}$  paths form straight light-like trajectories. Figure 2.1 illustrates the (a) space-time and (b) transverse arrangement of the loops.

The  $\vec{r}_i$  and  $z_i$  distribution of the color-dipoles is given by the *wave functions*  $\psi_{a,b}$  and  $\psi_{c,d}$  that characterize the interacting particles. In this framework, the color-dipoles are given by the quark and antiquark in the meson or photon and in a simplified picture by a quark and diquark in the baryon. Concentrating in this work on reactions with  $a = c$  and  $b = d$ , only squared wave functions  $|\psi_1(z_1, \vec{r}_1)|^2 := \psi_c^*(z_1, \vec{r}_1) \psi_a(z_1, \vec{r}_1)$  and  $|\psi_2(z_2, \vec{r}_2)|^2 := \psi_d^*(z_2, \vec{r}_2) \psi_b(z_2, \vec{r}_2)$  are needed. We use for hadrons the phenomenological Gaussian wave function [23, 44] and for photons the perturbatively derived wave functions with running quark masses  $m_f(Q^2)$  to account for non-perturbative effects at low photon virtuality  $Q^2$  [20] as discussed explicitly in Appendix B.

The QCD vacuum expectation value  $\langle \dots \rangle_G$  in the  $S_{r_1 r_2}$  matrix element (2.1.3) represents functional integrals [11] in which the functional integration over the fermion fields has already been carried out as indicated by the subscript  $G$ . The model we use for the QCD vacuum works in the *quenched approximation* that does not allow string breaking through dynamical quark-antiquark production in color-dipoles in the fundamental representation of  $SU(3)$ . The linear rise of static color-dipole potentials [16, 17] and dipole-hadron cross-sections at large dipole sizes as well as the  $1/|\vec{k}_\perp|$  behavior of unintegrated gluon distributions at small transverse momenta  $|\vec{k}_\perp|$  display explicitly the quenched approximation as shown in this work.

In this work we perform computations with Wegner-Wilson loops in a general representation  $r$  of  $SU(N_c)$ . This allows several investigations: (a) The *large- $N_c$  limit* of our scattering amplitudes can be examined which may give additional insights into the scattering process. (b) The high-energy scattering of color-dipoles in different representations describing different physical objects can be studied. (c) In Euclidean space-time, different representations of the Wegner-Wilson loop are appropriate to study the Casimir scaling hypothesis of static potentials or chromo-field distributions of color-dipoles [17, 45]. (d) Since our model works in the quenched approximation, the investigation of the string breaking behavior of the static potential for color-dipoles in the fundamental and adjoint (glueballs) representation of  $SU(N_c)$  is possible: *string breaking* cannot occur in fundamental dipoles as dynamical quark-antiquark production is excluded but should be present for adjoint dipoles because of gluonic vacuum polarization [17, 46].

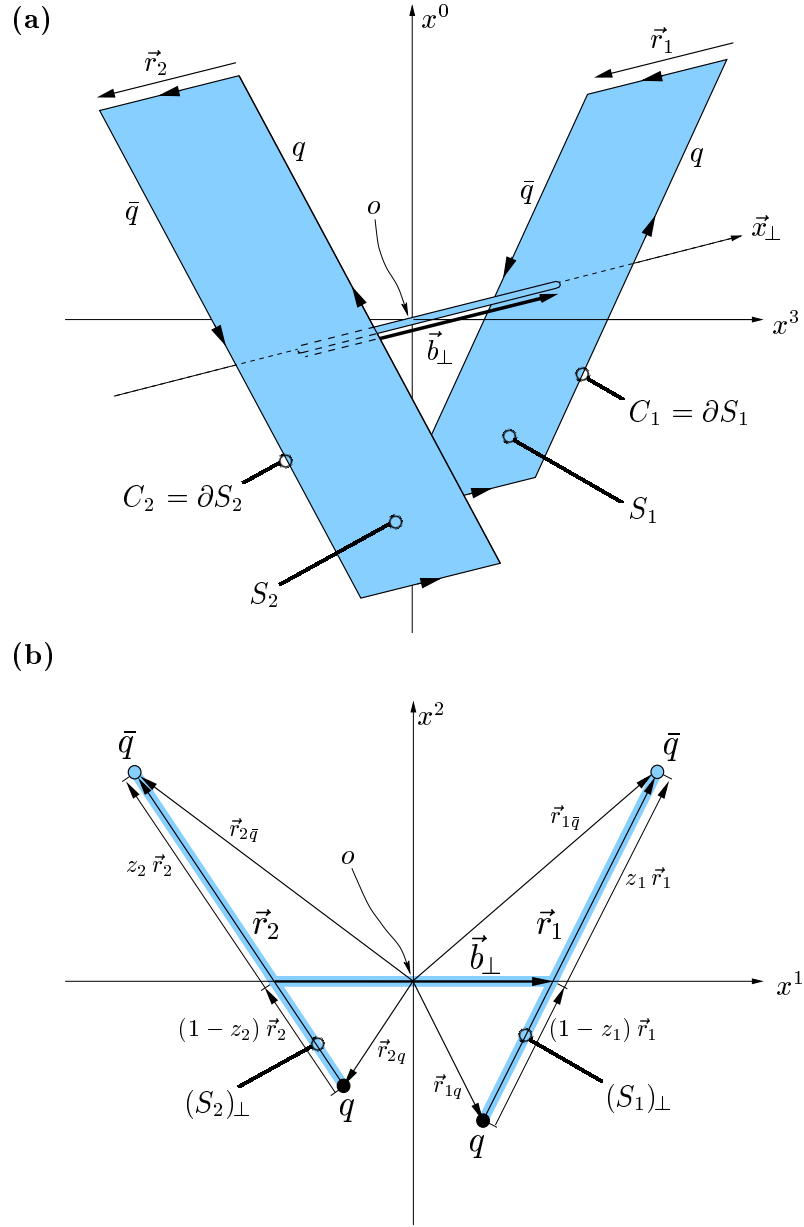


Figure 2.1: High-energy dipole-dipole scattering in the eikonal approximation represented by Wegner-Wilson loops in the fundamental representation of  $SU(3)$ : (a) space-time and (b) transverse arrangement of the Wegner-Wilson loops. The shaded areas represent the strings extending from the quark to the antiquark path in each color dipole. The thin tube allows to compare the field strengths in surface  $S_1$  with the field strengths in surface  $S_2$ . The impact parameter  $\vec{b}_\perp$  connects the centers of light-cone momenta of the dipoles.

## 2.2 Vacuum Expectation Value of one Wegner-Wilson Loop

To compute the expectation value of a Wegner-Wilson loop (2.1.4) in the QCD vacuum

$$\langle W_r[C] \rangle_G = \left\langle \tilde{\text{Tr}}_r \mathcal{P} \exp \left[ -i g \oint_C dz^\mu \mathcal{G}_\mu^a(z) t_r^a \right] \right\rangle_G, \quad (2.2.1)$$

we transform the line integral over the loop  $C$  into an integral over the surface  $S$  with  $\partial S = C$  by applying the *non-Abelian Stokes' theorem* [11, 15]

$$\langle W_r[C] \rangle_G = \left\langle \tilde{\text{Tr}}_r \mathcal{P}_S \exp \left[ -i \frac{g}{2} \int_S d\sigma^{\mu\nu}(z) \mathcal{G}_{\mu\nu}^a(o, z; C_{zo}) t_r^a \right] \right\rangle_G, \quad (2.2.2)$$

where  $\mathcal{P}_S$  indicates surface ordering and  $o$  is an arbitrary reference point on the surface  $S$ . In Eq. (2.2.2), the gluon field strength tensor,  $\mathcal{G}_{\mu\nu}(z) = \mathcal{G}_{\mu\nu}^a(z) t^a$ , is parallel transported to the reference point  $o$  along the path  $C_{zo}$

$$\mathcal{G}_{\mu\nu}(o, z; C_{zo}) = \Phi(o, z; C_{zo})^{-1} \mathcal{G}_{\mu\nu}(z) \Phi(o, z; C_{zo}) \quad (2.2.3)$$

with the QCD Schwinger string

$$\Phi(o, z; C_{zo}) = \mathcal{P} \exp \left[ -i g \int_{C_{zo}} dz^\mu \mathcal{G}_\mu^a(z) t_r^a \right]. \quad (2.2.4)$$

Due to the linearity of the functional integral,  $\langle \tilde{\text{Tr}}_r \dots \rangle = \tilde{\text{Tr}}_r \langle \dots \rangle$ , Eq. (2.2.2) reduces to

$$\langle W_r[C] \rangle_G = \tilde{\text{Tr}}_r \left\langle \mathcal{P}_S \exp \left[ -i \frac{g}{2} \int_S d\sigma^{\mu\nu}(z) \mathcal{G}_{\mu\nu}^a(o, z; C_{zo}) t_r^a \right] \right\rangle_G. \quad (2.2.5)$$

For the evaluation of (2.2.5), a *matrix cumulant expansion* is used as explained in [11] (cf. also [47])

$$\begin{aligned} & \left\langle \mathcal{P}_S \exp \left[ -i \frac{g}{2} \int_S d\sigma(z) \mathcal{G}(o, z; C_{zo}) \right] \right\rangle_G \\ &= \exp \left[ \sum_{n=1}^{\infty} \frac{1}{n!} \left( -i \frac{g}{2} \right)^n \int d\sigma(x_1) \cdots d\sigma(x_n) K_n(x_1, \dots, x_n) \right], \end{aligned} \quad (2.2.6)$$

where space-time indices are suppressed to lighten notation. The cumulants  $K_n$  consist of expectation values of *ordered* products of the non-commuting matrices  $\mathcal{G}(o, z; C_{zo})$ . The leading matrix cumulants are

$$K_1(x) = \langle \mathcal{G}(o, x; C_x) \rangle_G, \quad (2.2.7)$$

$$\begin{aligned} K_2(x_1, x_2) &= \langle \mathcal{P}_S [\mathcal{G}(o, x_1; C_{x_1}) \mathcal{G}(o, x_2; C_{x_2})] \rangle_G \\ &\quad - \frac{1}{2} (\langle \mathcal{G}(o, x_1; C_{x_1}) \rangle_G \langle \mathcal{G}(o, x_2; C_{x_2}) \rangle_G + (1 \leftrightarrow 2)). \end{aligned} \quad (2.2.8)$$

Since the vacuum does not prefer a specific color direction,  $K_1$  vanishes and  $K_2$  becomes

$$K_2(x_1, x_2) = \langle \mathcal{P}_S[\mathcal{G}(o, x_1; C_{x_1}) \mathcal{G}(o, x_2; C_{x_2})] \rangle_G . \quad (2.2.9)$$

Now, we approximate the functional integral associated with the expectation values  $\langle \dots \rangle_G$  as a *Gaussian integral* in the gluon field strength. Consequently, the cumulants factorize into two-point field correlators such that all higher cumulants,  $K_n$  with  $n > 2$ , vanish<sup>1</sup> and  $\langle W_r[C] \rangle_G$  can be expressed in terms of  $K_2$

$$\begin{aligned} \langle W_r[C] \rangle_G &= \tilde{\text{Tr}}_r \exp \left[ -\frac{g^2}{8} \int_S d\sigma^{\mu\nu}(x_1) \int_S d\sigma^{\rho\sigma}(x_2) \right. \\ &\quad \left. \langle \mathcal{P}_S [\mathcal{G}_{\mu\nu}^a(o, x_1; C_{x_1 o}) t_r^a \mathcal{G}_{\rho\sigma}^b(o, x_2; C_{x_2 o}) t_r^b] \rangle_G \right] \end{aligned} \quad (2.2.10)$$

Due to the color-neutrality of the vacuum, the gauge-invariant bilocal gluon field strength correlator contains a  $\delta$ -function in color-space,

$$\left\langle \frac{g^2}{4\pi^2} [\mathcal{G}_{\mu\nu}^a(o, x_1; C_{x_1 o}) \mathcal{G}_{\rho\sigma}^b(o, x_2; C_{x_2 o})] \right\rangle_G =: \frac{1}{4} \delta^{ab} F_{\mu\nu\rho\sigma}(x_1, x_2, o; C_{x_1 o}, C_{x_2 o}) \quad (2.2.11)$$

which makes the surface ordering  $\mathcal{P}_S$  in (2.2.10) irrelevant. The quantity  $F_{\mu\nu\rho\sigma}$  will be specified in Sec. 2.4. With (2.2.11) and the quadratic Casimir operator  $C_2(r)$ ,

$$t_r^a t_r^a = t_r^2 = C_2(r) \mathbb{1}_r , \quad (2.2.12)$$

Eq. (2.2.10) reads

$$\langle W_r[C] \rangle_G = \tilde{\text{Tr}}_r \exp [-C_2(r) \chi_{SS} \mathbb{1}_r] = \exp \left[ -i \frac{C_2(r)}{2} \chi_{SS} \right] , \quad (2.2.13)$$

where

$$\chi_{SS} := -i \frac{\pi^2}{4} \int_S d\sigma^{\mu\nu}(x_1) \int_S d\sigma^{\rho\sigma}(x_2) F_{\mu\nu\rho\sigma}(x_1, x_2, o; C_{x_1 o}, C_{x_2 o}) . \quad (2.2.14)$$

Our ansatz for the tensor structure of  $F_{\mu\nu\rho\sigma}$  in Minkowski space-time – see (2.4.1), (2.4.6), and (2.4.3) – leads to  $\chi_{SS} = 0$  for light-like loops, as explained in Sec. 2.5. Consequently, the vacuum expectation value of the Wegner-Wilson loop becomes

$$\langle W_r[C] \rangle_G = 1 . \quad (2.2.15)$$

The deviation of  $\langle W_r[C] \rangle_G$  from one is just a measure of the strength of parton splitting processes, e.g.,  $q \rightarrow q + G$ . Our result (2.2.15) is consistent with the quenched approximation and remains valid for arbitrary surface choices.

---

<sup>1</sup>We are going to use the cumulant expansion in the Gaussian approximation also for perturbative gluon exchange. Here certainly the higher cumulants are non-zero.

In Euclidean space-time one obtaines  $\chi_{SS}^E \neq 0$  since the loops are not light-like and  $F_{\mu\nu\rho\sigma}^E$  is different from the Minkowskian one. This allows one to compute the potential of static color-dipoles [16, 17] from the expectation value of one Wegner-Wilson loop in Euclidean space-time as discussed briefly at the end of this chapter.

## 2.3 The Loop-Loop Correlation Function

The computation of the *loop-loop correlation function*  $\langle W_{r_1}[C_1]W_{r_2}[C_2] \rangle_G$  starts also with the application of the the *non-Abelian Stokes' theorem* [11, 15] that is used to transform the line integrals over the loops  $C_{1,2}$  into integrals over surfaces  $S_{1,2}$  with  $\partial S_{1,2} = C_{1,2}$  as in the previous section

$$\begin{aligned} \langle W_{r_1}[C_1]W_{r_2}[C_2] \rangle_G &= \left\langle \tilde{\text{Tr}}_{r_1} \mathcal{P}_S \exp \left[ -i \frac{g}{2} \int_{S_1} d\sigma^{\mu\nu}(x_1) \mathcal{G}_{\mu\nu}^a(o_1, x_1; C_{x_1 o_1}) t_{r_1}^a \right] \right. \\ &\quad \left. \times \tilde{\text{Tr}}_{r_2} \mathcal{P}_S \exp \left[ -i \frac{g}{2} \int_{S_2} d\sigma^{\rho\sigma}(x_2) \mathcal{G}_{\rho\sigma}^b(o_2, x_2; C_{x_2 o_2}) t_{r_2}^b \right] \right\rangle_G \quad (2.3.1) \end{aligned}$$

where  $o_1$  and  $o_2$  are the reference points on the surfaces  $S_1$  and  $S_2$ , respectively, that enter through the non-Abelian Stokes' theorem. In order to ensure gauge invariance in our model, the gluon field strengths associated with the loops must be compared at *one* reference point  $o$ . Therefore, we require the surfaces  $S_1$  and  $S_2$  to touch at a common reference point  $o_1 = o_2 = o$ .

Following the Berger-Nachtmann approach [14], the product of the two traces,  $\tilde{\text{Tr}}_{r_1}(\dots) \tilde{\text{Tr}}_{r_2}(\dots)$ , over  $SU(N_c)$  matrices in the  $r_1$  and  $r_2$  representation, respectively, is interpreted as one trace  $\tilde{\text{Tr}}_{r_1 \otimes r_2}(\dots) := \text{Tr}_{r_1 \otimes r_2}(\dots) / \text{Tr}_{r_1 \otimes r_2}(\mathbb{1}_{r_1 \otimes r_2})$  that acts in the tensor product space built from the  $r_1$  and  $r_2$  representations

$$\begin{aligned} \langle W_{r_1}[C_1]W_{r_2}[C_2] \rangle_G &= \left\langle \tilde{\text{Tr}}_{r_1 \otimes r_2} \left\{ \left[ \mathcal{P}_S \exp \left[ -i \frac{g}{2} \int_{S_1} d\sigma^{\mu\nu}(x_1) \mathcal{G}_{\mu\nu}^a(o, x_1; C_{x_1 o}) t_{r_1}^a \right] \otimes \mathbb{1}_{r_2} \right] \right. \right. \\ &\quad \left. \left. \times \left[ \mathbb{1}_{r_1} \otimes \mathcal{P}_S \exp \left[ -i \frac{g}{2} \int_{S_2} d\sigma^{\rho\sigma}(x_2) \mathcal{G}_{\rho\sigma}^b(o, x_2; C_{x_2 o}) t_{r_2}^b \right] \right] \right\} \right\rangle_G \quad (2.3.2) \end{aligned}$$

Using the identities

$$\exp(t_{r_1}^a) \otimes \mathbb{1}_{r_2} = \exp(t_{r_1}^a \otimes \mathbb{1}_{r_2}) \quad (2.3.3)$$

$$\mathbb{1}_{r_1} \otimes \exp(t_{r_2}^a) = \exp(\mathbb{1}_{r_1} \otimes t_{r_2}^a) \quad (2.3.4)$$

the tensor products can be shifted into the exponents. With matrix multiplication in the tensor product space

$$\begin{aligned} (t_{r_1}^a \otimes \mathbb{1}_{r_2})(t_{r_1}^b \otimes \mathbb{1}_{r_2}) &= t_{r_1}^a t_{r_1}^b \otimes \mathbb{1}_{r_2} \\ (t_{r_1}^a \otimes \mathbb{1}_{r_2})(\mathbb{1}_{r_1} \otimes t_{r_2}^b) &= t_{r_1}^a \otimes t_{r_2}^b \end{aligned} \quad (2.3.5)$$

and the vanishing commutator

$$[t_{r_1}^a \otimes \mathbb{1}_{r_2}, \mathbb{1}_{r_1} \otimes t_{r_2}^b] = 0 \quad (2.3.6)$$

the two exponentials in (2.3.2) commute and can be written as one exponential

$$\langle W[C_1]W[C_2] \rangle_G = \left\langle \tilde{\text{Tr}}_{r_1 \otimes r_2} \mathcal{P}_S \exp \left[ -i \frac{g}{2} \int_S d\sigma^{\mu\nu}(x) \hat{\mathcal{G}}_{\mu\nu}(o, x; C_{xo}) \right] \right\rangle_G \quad (2.3.7)$$

with the following gluon field strength tensor acting in the tensor product space

$$\hat{\mathcal{G}}_{\mu\nu}(o, x; C_{xo}) := \begin{cases} \mathcal{G}_{\mu\nu}^a(o, x; C_{xo})(t_{r_1}^a \otimes \mathbb{1}_{r_2}) & \text{for } x \in S_1 \\ \mathcal{G}_{\mu\nu}^a(o, x; C_{xo})(\mathbb{1}_{r_1} \otimes t_{r_2}^a) & \text{for } x \in S_2 \end{cases} . \quad (2.3.8)$$

In Eq. (2.3.7), the surface integrals over  $S_1$  and  $S_2$  are written as one integral over the combined surface  $S = S_1 + S_2$  so that the right-hand side (rhs) of (2.3.7) becomes very similar to the rhs of (2.2.2). This allows us to proceed analogously to the computation of  $\langle W_r[C] \rangle_G$  in the previous section: With the linearity of the functional integral, the matrix cumulant expansion, the color-neutrality of the vacuum, and the Gaussian approximation now in the color components of the gluon field strength tensor  $\hat{\mathcal{G}}_{\mu\nu}(o, x; C_{xo})$ , only the  $n = 2$  term of the matrix cumulant expansion survives, which leads to

$$\begin{aligned} & \left\langle W_{r_1}[C_1]W_{r_2}[C_2] \right\rangle_G \\ &= \tilde{\text{Tr}}_{r_1 \otimes r_2} \exp \left[ -\frac{g^2}{8} \int_S d\sigma^{\mu\nu}(x_1) \int_S d\sigma^{\rho\sigma}(x_2) \left\langle \mathcal{P}_S [\hat{\mathcal{G}}_{\mu\nu}(o, x_1; C_{x_1 o}) \hat{\mathcal{G}}_{\rho\sigma}(o, x_2; C_{x_2 o})] \right\rangle_G \right] . \end{aligned} \quad (2.3.9)$$

Note that the Gaussian approximation on the level of the color components of the gluon field strength tensor (component factorization) differs from the one on the level of the gluon field strength tensor (matrix factorization) used to compute  $\langle W_r[C] \rangle$  in the original version of the SVM [16]. Nevertheless, with the additional ordering rule [48] explained in detail in Sec. 2.4 of [49], a modified component factorization is obtained that leads to the same area law as the matrix factorization.

Using definition (2.3.8) and relations (2.3.5), we now redivide the exponent in (2.3.10) into integrals of the ordinary parallel transported gluon field strengths over the separate surfaces  $S_1$  and  $S_2$

$$\begin{aligned}
& \left\langle W_{r_1}[C_1]W_{r_2}[C_2] \right\rangle_G = \tilde{\text{Tr}}_{r_1 \otimes r_2} \exp \left[ \right. \\
& \left. -\frac{g^2}{8} \int_{S_1} d\sigma^{\mu\nu}(x_1) \int_{S_2} d\sigma^{\rho\sigma}(x_2) \mathcal{P}_S \left[ \left\langle \mathcal{G}_{\mu\nu}^a(o, x_1; C_{x_1 o}) \mathcal{G}_{\rho\sigma}^b(o, x_2; C_{x_2 o}) \right\rangle_G (t_{r_1}^a \otimes t_{r_2}^b) \right] \right. \\
& \left. -\frac{g^2}{8} \int_{S_2} d\sigma^{\mu\nu}(x_1) \int_{S_1} d\sigma^{\rho\sigma}(x_2) \mathcal{P}_S \left[ \left\langle \mathcal{G}_{\mu\nu}^a(o, x_1; C_{x_1 o}) \mathcal{G}_{\rho\sigma}^b(o, x_2; C_{x_2 o}) \right\rangle_G (t_{r_1}^a \otimes t_{r_2}^b) \right] \right. \\
& \left. -\frac{g^2}{8} \int_{S_1} d\sigma^{\mu\nu}(x_1) \int_{S_1} d\sigma^{\rho\sigma}(x_2) \mathcal{P}_S \left[ \left\langle \mathcal{G}_{\mu\nu}^a(o, x_1; C_{x_1 o}) \mathcal{G}_{\rho\sigma}^b(o, x_2; C_{x_2 o}) \right\rangle_G (t_{r_1}^a t_{r_1}^b \otimes \mathbb{1}_{r_2}) \right] \right. \\
& \left. \left. -\frac{g^2}{8} \int_{S_2} d\sigma^{\mu\nu}(x_1) \int_{S_2} d\sigma^{\rho\sigma}(x_2) \mathcal{P}_S \left[ \left\langle \mathcal{G}_{\mu\nu}^a(o, x_1; C_{x_1 o}) \mathcal{G}_{\rho\sigma}^b(o, x_2; C_{x_2 o}) \right\rangle_G (\mathbb{1}_{r_1} \otimes t_{r_2}^a t_{r_2}^b) \right] \right] . \quad (2.3.10)
\end{aligned}$$

Here the surface ordering  $\mathcal{P}_S$  is again irrelevant due to the color-neutrality of the vacuum (2.2.11), and (2.3.11) becomes

$$\begin{aligned}
& \left\langle W_{r_1}[C_1]W_{r_2}[C_2] \right\rangle_G = \tilde{\text{Tr}}_{r_1 \otimes r_2} \exp \left[ -i \frac{1}{2} \left\{ (\chi_{S_1 S_2} + \chi_{S_2 S_1}) (t_{r_1}^a \otimes t_{r_2}^a) \right. \right. \\
& \left. \left. + \chi_{S_1 S_1} (t_{r_1}^a t_{r_1}^a \otimes \mathbb{1}_{r_2}) + \chi_{S_2 S_2} (\mathbb{1}_{r_1} \otimes t_{r_2}^a t_{r_2}^a) \right\} \right] \quad (2.3.11)
\end{aligned}$$

with

$$\chi_{S_i S_j} := -i \frac{\pi^2}{4} \int_{S_i} d\sigma^{\mu\nu}(x_1) \int_{S_j} d\sigma^{\rho\sigma}(x_2) F_{\mu\nu\rho\sigma}(x_1, x_2, o; C_{x_1 o}, C_{x_2 o}) . \quad (2.3.12)$$

The symmetries in the tensor structure of  $F_{\mu\nu\rho\sigma}$  in Minkowski space-time – see (2.4.1), (2.4.6), and (2.4.3) – lead to  $\chi_{S_1 S_1} = \chi_{S_2 S_2} = 0$  for light-like loops as explained in Sec. 2.5, and also to  $\chi_{S_1 S_2} = \chi_{S_2 S_1} =: \chi$ .<sup>2</sup> Our final Minkowskian result for general  $SU(N_c)$  representations  $r_1$  and  $r_2$  becomes

$$\left\langle W_{r_1}[C_1]W_{r_2}[C_2] \right\rangle_G = \tilde{\text{Tr}}_{r_1 \otimes r_2} \exp \left[ -i \chi (t_{r_1}^a \otimes t_{r_2}^a) \right] . \quad (2.3.13)$$

After specifying the representations  $r_1$  and  $r_2$ , the tensor product  $t_{r_1 \otimes r_2} := t_{r_1}^a \otimes t_{r_2}^a$  can be expressed as a sum of projection operators  $P_i$  with the property  $P_i t_{r_1 \otimes r_2} = \lambda_i P_i$  where

$$t_{r_1 \otimes r_2} = \sum \lambda_i P_i \quad \text{with} \quad \lambda_i = \frac{\tilde{\text{Tr}}_{r_1 \otimes r_2}(P_i t_{r_1 \otimes r_2})}{\tilde{\text{Tr}}_{r_1 \otimes r_2}(P_i)} , \quad (2.3.14)$$

---

<sup>2</sup>In Euclidean space-time a different result is obtained since  $\chi_{S_i S_i} \neq 0$  as shown in [17].

which corresponds to the decomposition of the tensor product space into irreducible representations.

For two Wegner-Wilson-loops in the *fundamental representation* of  $SU(N_c)$ ,  $r_1 = r_2 = N_c$ , that describe the trajectories of two quark-antiquark dipoles, the decomposition (2.3.14) becomes trivial

$$t_{N_c}^a \otimes t_{N_c}^a = \frac{N_c - 1}{2N_c} P_s - \frac{N_c + 1}{2N_c} P_a , \quad (2.3.15)$$

with the projection operators

$$(P_s)_{(\alpha_1\alpha_2)(\beta_1\beta_2)} = \frac{1}{2}(\delta_{\alpha_1\beta_1}\delta_{\alpha_2\beta_2} + \delta_{\alpha_1\beta_2}\delta_{\alpha_2\beta_1}) \quad (2.3.16)$$

$$(P_a)_{(\alpha_1\alpha_2)(\beta_1\beta_2)} = \frac{1}{2}(\delta_{\alpha_1\beta_1}\delta_{\alpha_2\beta_2} - \delta_{\alpha_1\beta_2}\delta_{\alpha_2\beta_1}) \quad (2.3.17)$$

that decompose the direct product space of two fundamental  $SU(N_c)$  representations into the irreducible representations

$$N_c \otimes N_c = (N_c + 1)N_c/2 \oplus \overline{N_c(N_c - 1)/2} . \quad (2.3.18)$$

Using  $\text{Tr}_{N_c \otimes N_c} 1\!\!1_{N_c \otimes N_c} = N_c^2$  and the projector properties

$$P_{s,a}^2 = P_{s,a} , \quad \text{Tr}_{N_c \otimes N_c} P_s = (N_c + 1)N_c/2 , \quad \text{and} \quad \text{Tr}_{N_c \otimes N_c} P_a = (N_c - 1)N_c/2 , \quad (2.3.19)$$

we find a simple expression for the loop-loop correlation function with both loops in the fundamental  $SU(N_c)$  representation

$$\left\langle W_{N_c}[C_1]W_{N_c}[C_2] \right\rangle_G = \frac{N_c + 1}{2N_c} \exp\left[-i\frac{N_c - 1}{2N_c}\chi\right] + \frac{N_c - 1}{2N_c} \exp\left[i\frac{N_c + 1}{2N_c}\chi\right] \quad (2.3.20)$$

and recover, of course, for  $N_c = 3$  the result from [14].

For one Wegner-Wilson-loop in the *fundamental* and one in the *adjoint representation* of  $SU(N_c)$ ,  $r_1 = N_c$  and  $r_2 = N_c^2 - 1$ , that can be used to describe the scattering of a quark-antiquark dipole with a glueball, the decomposition (2.3.14) reads

$$t_{N_c}^a \otimes t_{N_c^2-1}^a = -\frac{N_c}{2} P_1 + \frac{1}{2} P_2 - \frac{1}{2} P_3 \quad (2.3.21)$$

with the projection operators<sup>3</sup>  $P_1$ ,  $P_2$ , and  $P_3$  that decompose the direct product

---

<sup>3</sup>The explicit form of the projection operators  $P_1$ ,  $P_2$ , and  $P_3$  can be found in [50] but note that we use the Gell-Mann (conventional) normalization of the gluons. The eigenvalues,  $\lambda_i$ , of the projection operators in (2.3.21) can be evaluated conveniently with the computer program “Colour” [51].

space of one fundamental and one adjoint  $SU(N_c)$  representation into the the irreducible representations

$$N_c \otimes N_c^2 - 1 = N_c \oplus \frac{1}{2} N_c(N_c - 1)(N_c + 2) \oplus \frac{1}{2} N_c(N_c + 1)(N_c - 2) \quad (2.3.22)$$

which reduces for  $N_c = 3$  to the well-known  $SU(3)$  decomposition

$$3 \otimes 8 = 3 \oplus 15 \oplus 6. \quad (2.3.23)$$

With  $\text{Tr}_{N_c \otimes N_c^2 - 1} \mathbb{1}_{N_c \otimes N_c^2 - 1} = N_c(N_c^2 - 1)$  and projector properties analogous to (2.3.19), we obtain the loop-loop correlation function for one loop in the fundamental and one in the adjoint representation of  $SU(N_c)$

$$\begin{aligned} & \left\langle W_{N_c}[C_1] W_{N_c^2 - 1}[C_2] \right\rangle_G \\ &= \frac{1}{N_c^2 - 1} \exp\left[i \frac{N_c}{2} \chi\right] + \frac{N_c + 2}{2(N_c + 1)} \exp\left[-i \frac{1}{2} \chi\right] + \frac{N_c - 2}{2(N_c - 1)} \exp\left[i \frac{1}{2} \chi\right]. \end{aligned} \quad (2.3.24)$$

Note that our results given in Eqs. (2.3.20) and (2.3.24) are quite general since they are obtained directly from the color-neutrality of the QCD vacuum and the Gaussian approximation of the functional integrals. For the explicit computation of  $\chi$ -function in Eqs. (2.3.20) and (2.3.24) one has to specify the gluon field strength correlator  $F_{\mu\nu\rho\sigma}$  and the surfaces  $S_{1,2}$  with the restriction  $\partial S_{1,2} = C_{1,2}$  that appear in the  $\chi$ -function (2.3.12). This we do in the following sections. Furthermore, we concentrate in the following on the dipole-dipole scattering (2.3.20) as the relevant case and postpone the dipole-glueball scattering (2.3.24) for future investigations.

## 2.4 Perturbative and Non-Perturbative QCD Components

We decompose the gauge-invariant bilocal gluon field strength correlator (2.2.11) into a perturbative ( $P$ ) and non-perturbative ( $NP$ ) component

$$F_{\mu\nu\rho\sigma} = F_{\mu\nu\rho\sigma}^P + F_{\mu\nu\rho\sigma}^{NP}, \quad (2.4.1)$$

where  $F_{\mu\nu\rho\sigma}^P$  gives the perturbative physics (short-range correlations) described by *perturbative gluon exchange* and  $F_{\mu\nu\rho\sigma}^{NP}$  the non-perturbative physics (long-range correlations) modelled by the *stochastic vacuum model* (SVM) [16]. This combination allows us to describe long and short distance correlations in agreement with lattice calculations of the Euclidean gluon field strength correlator [24, 25]. Moreover, this two component ansatz leads to the static quark-antiquark potential with color-Coulomb behavior for small and confining linear rise for large source separations in

good agreement with lattice data as shown in our recent work [17]. Note that besides our two component ansatz an ongoing effort to reconcile the non-perturbative SVM with perturbative gluon exchange that has led to complementary methods [52–54].

We compute the perturbative gluon field strength correlator  $F_{\mu\nu\rho\sigma}^P$  from the gluon propagator in Feynman-’t Hooft gauge

$$\left\langle \mathcal{G}_\mu^a(x_1) \mathcal{G}_\nu^b(x_2) \right\rangle = \int \frac{d^4 k}{(2\pi)^4} \frac{-i\delta^{ab}g_{\mu\nu}}{k^2 - m_G^2} e^{-ik(x_1 - x_2)}, \quad (2.4.2)$$

where we introduce an *effective gluon mass*  $m_G$  to limit the range of the perturbative interaction in the infrared (IR) region. In leading order in the strong coupling  $g$ , the perturbative correlator is gauge-invariant already without the parallel transport to a common reference point and depends only on the difference  $z := x_1 - x_2$ ,

$$\begin{aligned} F_{\mu\nu\rho\sigma}^P(z) &= \frac{g^2}{\pi^2} \frac{1}{2} \left[ \frac{\partial}{\partial z_\nu} (z_\sigma g_{\mu\rho} - z_\rho g_{\mu\sigma}) + \frac{\partial}{\partial z_\mu} (z_\rho g_{\nu\sigma} - z_\sigma g_{\nu\rho}) \right] D_P(z^2) \\ &= -\frac{g^2}{\pi^2} \int \frac{d^4 k}{(2\pi)^4} e^{-ikz} \left[ k_\nu k_\sigma g_{\mu\rho} - k_\nu k_\rho g_{\mu\sigma} + k_\mu k_\rho g_{\nu\sigma} - k_\mu k_\sigma g_{\nu\rho} \right] \tilde{D}'_P(k^2) \end{aligned} \quad (2.4.3)$$

with the *perturbative correlation function*

$$\tilde{D}'_P(k^2) := \frac{d}{dk^2} \int d^4 z D_P(z^2) e^{ikz} = \frac{i}{k^2 - m_G^2}. \quad (2.4.4)$$

We take into account radiative corrections in perturbative correlations by replacing the constant coupling  $g^2$  with the *running coupling*

$$g^2(\vec{z}_\perp) = 4\pi\alpha_s(\vec{z}_\perp) = \frac{48\pi^2}{(33 - 2N_f) \ln \left[ (|\vec{z}_\perp|^{-2} + M^2)/\Lambda_{QCD}^2 \right]} \quad (2.4.5)$$

in the final step of the computation of the eikonal function  $\chi$ . Here the renormalization scale is provided by  $|\vec{z}_\perp|$  that represents the spatial separation of the interacting dipoles in transverse space<sup>4</sup>. In (2.4.5)  $N_f$  denotes the number of dynamical quark flavors, which is set to  $N_f = 0$  in agreement with the quenched approximation,  $\Lambda_{QCD} = 0.25$  GeV, and  $M^2$  allows us to freeze  $g^2$  for  $|\vec{z}_\perp| \rightarrow \infty$ .

If the path connecting the points  $x_1$  and  $x_2$  is a straight line, the non-perturbative correlator  $F_{\mu\nu\rho\sigma}^{NP}$  depends also only on the difference  $z := x_1 - x_2$ . Then, the most general form of the correlator in four-dimensional Minkowski space-time that respects

---

<sup>4</sup>Only transverse separations appear in the final expression of  $\chi$  as explained in Sec. 2.5.

translational, Lorentz, and parity invariance reads [12, 13]

$$F_{\mu\nu\rho\sigma}^{NP}(z) := F_{\mu\nu\rho\sigma}^{NP(nc)}(z) + F_{\mu\nu\rho\sigma}^{NP(c)}(z) \quad (2.4.6)$$

$$\begin{aligned} F_{\mu\nu\rho\sigma}^{NP(nc)}(z) &= \frac{G_2(1-\kappa)}{6(N_c^2-1)} \left( \frac{\partial}{\partial z_\nu} (z_\sigma g_{\mu\rho} - z_\rho g_{\mu\sigma}) + \frac{\partial}{\partial z_\mu} (z_\rho g_{\nu\sigma} - z_\sigma g_{\nu\rho}) \right) D_1(z^2) \quad (2.4.7) \\ &= -\frac{G_2(1-\kappa)}{6(N_c^2-1)} \int \frac{d^4k}{(2\pi)^4} e^{-ikz} \left( k_\nu k_\sigma g_{\mu\rho} - k_\nu k_\rho g_{\mu\sigma} + k_\mu k_\rho g_{\nu\sigma} - k_\mu k_\sigma g_{\nu\rho} \right) \tilde{D}'_1(k^2) \end{aligned}$$

$$\begin{aligned} F_{\mu\nu\rho\sigma}^{NP(c)}(z) &= \frac{G_2 \kappa}{3(N_c^2-1)} (g_{\mu\rho} g_{\nu\sigma} - g_{\mu\sigma} g_{\nu\rho}) D(z^2) \\ &= \frac{G_2 \kappa}{3(N_c^2-1)} (g_{\mu\rho} g_{\nu\sigma} - g_{\mu\sigma} g_{\nu\rho}) \int \frac{d^4k}{(2\pi)^4} e^{-ikz} \tilde{D}(k^2) . \quad (2.4.8) \end{aligned}$$

and was originally constructed in Euclidean space-time [16]. In all previous applications of the SVM, this form depending only on  $x_1$  and  $x_2$  has been used. New lattice results on the path dependence of the correlator [55] show a dominance of the shortest path. This result is effectively incorporated in the model since the straight paths dominate in the average over all paths.

In (2.4.7) and (2.4.8),  $a$  is the *correlation length*,  $G_2 := \langle \frac{g^2}{4\pi^2} \mathcal{G}_{\mu\nu}^a(0) \mathcal{G}_{\mu\nu}^a(0) \rangle$  is the *gluon condensate* [56],  $\kappa$  determines the relative weight of the two different tensor structures,  $D$  and  $D_1$  are the *non-perturbative correlation functions* in four dimensional Minkowski space-time, and

$$\tilde{D}'_1(k^2) := \frac{d}{dk^2} \int d^4z D_1(z^2/a^2) e^{ikz} . \quad (2.4.9)$$

Euclidean correlation functions are accessible together with the Euclidean correlator in lattice QCD [24, 25]. We adopt for our calculations the simple *exponential correlation functions* specified in four dimensional Euclidean space-time

$$D^E(Z^2/a^2) = D_1^E(Z^2/a^2) = \exp(-|Z|/a) , \quad (2.4.10)$$

that are motivated by lattice QCD measurements of the gluon field strength correlator  $F_{\mu\nu\rho\sigma}^{NP}(Z)$  [24, 25]. This correlation function stays positive for all Euclidean distances  $Z$  and, thus, is compatible with a spectral representation of the correlation function [27]. This means a conceptual improvement as compared with the correlation function used in earlier applications of the SVM which becomes negative at large distances [13, 14, 18, 20–23]. By analytic continuation of (2.4.10) we obtain the Minkowski correlation functions in (2.4.7) and (2.4.8) as shown in Appendix C.

The perturbative and non-perturbative gluon field strength correlators can be analytically continued from Euclidean to Minkowski space-time by the substitution

$\delta_{\mu\rho} \rightarrow -g_{\mu\rho}$  and the analytic continuation of the Euclidean correlation functions to real time,  $D_x^E(Z^2) \rightarrow D_x^M(z^2)$ , [12, 13]. An alternative analytic continuation has been recently proposed by Meggiolaro [57]. In our resent work [17] we have generalized Meggiolaro's analytic continuation from parton-parton to gauge-invariant dipole-dipole scattering. In this approach one considers the correlation of two Wegner-Wilson loops tilted by an angle  $\Theta$  with respect to each other in Euclidean space-time and obtaines – after Maggiolaro's prescription for the analytic continuation of the angle  $\Theta$  – the  $S$ -matrix element for dipole-dipole scattering in Minkowski space-time [17]. Both analytic continuations give, of course, the same results and allow us to study the effect of confinement examined in Euclidean space-time on high-energy reactions computed in Minkowski space-time [8, 17, 58]. In chapter 3 we show the important features of the confining QCD string and its manifestation in high-energy scattering.

### The Static Color-Dipole Potential

To illustrate the meaning of the different contributions  $F_{\mu\nu\rho\sigma}^{NP(nc)}(z)$  and  $F_{\mu\nu\rho\sigma}^{NP(c)}(z)$  in the non-perturbative correlator (2.4.6), let us consider the potential of a static color-dipole which is obtained from the expectation value of one Wegner-Wilson loop<sup>5</sup> computed in Euclidean space-time (E) [1, 59]

$$V_r(R) = -\lim_{T \rightarrow \infty} \frac{1}{T} \ln \langle W_r^E[C] \rangle. \quad (2.4.11)$$

The computation of  $\langle W_r^E[C] \rangle$  follows the same line as the one for the Minkowskian case shown in Sec. 2.2: The only difference is the non-vanishing Euclidean  $\chi_{SS}^E$  in the final step of the computation which has to be computed now with the Euclidean correlator  $F_{\mu\nu\rho\sigma}^E$ . For a loop in the fundamental representation,  $V_r = V_{N_c}$  describes the static quark-antiquark potential and for a loop in the adjoint representation,  $V_r = V_{N_c^2-1}$  gives the static potential of a gluino pair (adjoint dipole).

Considered in Euclidean space-time, the perturbative correlator (2.4.3) leads to the non-confining *color-Yukawa potential* of a static color-dipole [17],

$$V_r^P(R) = -\frac{C_2(r)g^2(R)}{4\pi R} \exp[-m_g R], \quad (2.4.12)$$

where  $C_2(r)$  is the quadratic Casimir operator defined in (2.2.12) and  $r$  denotes the representation of  $SU(N_c)$ . The perturbative contribution dominates the static potential at small dipole sizes  $R$ . In the limit  $m_g \rightarrow 0$ , Eq. (2.4.12) reduces to the well-known *color-Coulomb potential* [60].

---

<sup>5</sup>Here the subtraction of the self-energy of the color-sources is understood.

The tensor structure of  $F_{\mu\nu\rho\sigma}^{NP(nc)}(z)$  given in (2.4.7) is characteristic for Abelian gauge theories, coincides with the tensor structure of the perturbative correlator (2.4.3), and does not lead to confinement when considered in Euclidean space-time since it gives the static color-dipole potential [17],

$$V_r^{NP\ nc}(R) = -C_2(r) \frac{\pi^2 G_2 (1 - \kappa) a}{3(N_c^2 - 1)} R^2 K_2[R/a], \quad (2.4.13)$$

which vanishes exponentially for large dipole sizes  $R$ .

In contrast, the tensor structure of  $F_{\mu\nu\rho\sigma}^{NP(c)}(z)$  given in (2.4.8) can only occur in non-Abelian gauge theories and Abelian gauge-theories with monopoles. Its Euclidean version leads to the following static color-dipole potential [17]

$$V_r^{NP\ c}(R) = C_2(r) \frac{2\pi^2 G_2 \kappa}{3(N_c^2 - 1)} R^2 \int_0^R d\rho (R - \rho) \rho K_1[\rho/a] \quad (2.4.14)$$

when computed with the *minimal surface*, i.e., the planar surface bounded by the loop as indicated by the shaded area in Fig. 2.1. For large dipole sizes,  $R \gtrsim 0.5$  fm, Eq. (2.4.14) reduces to a linearly increasing static potential

$$V_r^{NP\ c}(R) \Big|_{R \gtrsim 0.5 \text{ fm}} = \sigma_r R + \text{const.}, \quad (2.4.15)$$

which leads to *confinement* [16, 17]. Therefore, we call the tensor structure in (2.4.7) containing  $(1 - \kappa)$  non-confining (*nc*) and the tensor structure in (2.4.8) containing  $\kappa$  confining (*c*).

Color-confinement [16] is realized in our model by the formation of a flux-tube of color-electric fields between the color-sources in the dipole [17, 30, 31]. We study the intrinsic structure of this flux-tube or confining QCD string and the interaction between QCD strings in chapter 3.

The QCD *string tension*  $\sigma_r$  is given by the non-perturbative confining component (2.4.8) and reads for a color-dipole in the representation  $r$  of  $SU(N_c)$  [16, 17]

$$\sigma_r = C_2(r) \frac{\pi^3 G_2 \kappa}{48} \int_0^\infty dZ^2 D(Z^2, a^2) = C_2(r) \frac{\pi^3 \kappa G_2 a^2}{24}, \quad (2.4.16)$$

with the exponential correlation function (2.4.10) used in the final step. Since the string tension can be computed from first principles within lattice QCD [26], relation (2.4.16) puts an important constraint on the three fundamental parameters of the non-perturbative QCD vacuum  $a$ ,  $G_2$ , and  $\kappa$ . With the values for  $a$ ,  $G_2$ , and  $\kappa$  given in Sec. 2.7, that are used throughout this work, one obtains

for the string tension of the  $SU(3)$  quark-antiquark potential ( $r = 3$ ) a value of  $\sigma_3 = 0.22 \text{ GeV}^2 \equiv 1.12 \text{ GeV/fm}$  which coincides with those obtained from hadron spectroscopy [61], Regge theory [62], and lattice QCD investigations [26].

The *Casimir scaling* of the static potential can be directly seen from (2.4.12)-(2.4.14). It emerges trivially in our approach as a consequence of the Gaussian approximation explained in Sec. 2.2. Since the Casimir scaling hypothesis of the static potential has been verified to high accuracy for  $SU(N_c)$  on the lattice [33], this result has been interpreted as a strong hint towards Gaussian dominance in the QCD vacuum and, thus, as evidence for a strong suppression of higher cumulant contributions [63, 64]. In comparison to our model, the instanton model can neither describe Casimir scaling [64] nor the linear rise of the confining potential [65].

The static potential of an adjoint dipole differs from that of a fundamental dipole only in the eigenvalue of the corresponding quadratic Casimir operator:  $C_2(r) = C_2(N_c^2 - 1) = N_c$  for adjoint and  $C_2(r) = C_2(N_c) = (N_c^2 - 1)/(2N_c)$  for fundamental dipoles. Our model working in the quenched approximation has a shortcoming at large dipole sizes: *string breaking* cannot occur in fundamental dipoles as dynamical quark-antiquark production is excluded but should be present for adjoint dipoles because of dynamical gluon production. From Eqs. (2.4.15) and (2.4.16) it is clear that string breaking is neither described for fundamental nor for adjoint dipoles in our model. Interestingly, even on the lattice there has been no striking evidence for adjoint quark screening in quenched QCD [46]. It is even conjectured that the Wegner-Wilson loop operator is not suited to studies of string breaking [66].

## 2.5 Evaluation of the $\chi$ -Function with Minimal Surfaces

For the computation of the  $\chi$ -function (2.2.14)

$$\begin{aligned} \chi &:= \chi^P + \chi_{nc}^{NP} + \chi_c^{NP} \\ &= -i \frac{\pi^2}{4} \int_{S_1} d\sigma^{\mu\nu}(x_1) \int_{S_2} d\sigma^{\rho\sigma}(x_2) \left( F_{\mu\nu\rho\sigma}^P + F_{\mu\nu\rho\sigma}^{NP(nc)} + F_{\mu\nu\rho\sigma}^{NP(c)} \right), \end{aligned} \quad (2.5.1)$$

one has to specify surfaces  $S_{1,2}$  with the restriction  $\partial S_{1,2} = C_{1,2}$  according to the non-Abelian Stokes' theorem. As illustrated in Fig. 2.1, we put the reference point  $o$  at the origin of the coordinate system and choose for  $S_{1,2}$  the *minimal surfaces* that are built from the areas spanned by the corresponding loops  $C_{1,2}$  and the infinitesimally thin tube which connects the two surfaces  $S_1$  and  $S_2$ . The thin tube allows us to compare the field strengths in surface  $S_1$  with the field strengths in surface  $S_2$ .

Due to the truncation of the cumulant expansion or, equivalently, the Gaussian approximation, the non-perturbative confining component  $\chi_c^{NP}$  depends on the specific surface choice. This is not the case for the perturbative and the non-perturbative non-confining component. A different and more complicated result for  $\chi_c^{NP}$  was obtained with the pyramid mantle choice for the surfaces  $S_{1,2}$  in earlier applications of the SVM to high-energy scattering [13, 14, 18, 20–23]. In this work we use the minimal surfaces because of the following reasons. Minimal surface are usually used to obtain Wilson’s area law [16, 17]. The minimal surfaces are also favored by other complementary approaches such as the strong coupling expansion in lattice QCD, where plaquettes cover the minimal surface, or large- $N_c$  investigations, where the planar gluon diagrams dominate in the large- $N_c$  limit. Within bosonic string theory, our minimal surfaces represent the worldsheets of the *rigid* strings: Our model does not describe fluctuations or excitations of the string and thus cannot reproduce the Lüscher term which has recently been confirmed with unprecedented precision by Lüscher and Weisz [68].

Internal consistencies of our model favorize also the minimal surface: Since our results for the vacuum expectation value (VEV) of a rectangular Wegner-Wilson loop lead to a static quark-antiquark potential that is in good agreement with lattice data [17], we are led to conclude that the choice of the minimal surface is required by the Gaussian approximation in the gluon field strengths. Furthermore, we have shown in our recent work [17] that the minimal surfaces are actually needed to ensure the consistency of our results for the VEV of one loop  $\langle W_r[C] \rangle$  and the loop-loop correlation function  $\langle W_{r_1}[C_1]W_{r_2}[C_2] \rangle$ . Phenomenologically, in comparison with pyramid mantles, the description of the slope parameter  $B(s)$ , the differential elastic cross section  $d\sigma^{el}/dt(s, t)$ , and the elastic cross section  $\sigma^{el}(s)$  can be improved with minimal surfaces as shown in chapter 5.

The simplicity of the minimal surfaces is appealing: It allows us to show for the first time the structure of non-perturbative dipole-dipole interactions in momentum space, to represent the QCD string as a collection of stringless dipoles and to compute unintegrated gluon distributions of hadrons and photons. This is shown in chapter 3 and [58].

In applications of the model to high-energy scattering [8, 58, 67] the minimal surfaces are the most natural choice to examine the scattering of two rigid strings without any fluctuations or excitations. Our model does unfortunately not choose the surface dynamically and, thus, cannot describe string flips between two non-perturbative color-dipoles. This could generate also the energy dependence in non-perturbative interactions. Recently, new developments towards a dynamical surface choice and a theory for the dynamics of the confining strings have been reported [54].

## Parametrization of the Minimal Surfaces

The minimal surfaces  $S_1$  and  $S_2$  shown as shaded areas in Fig. 2.1 can be parametrized with the upper (lower) subscripts and signs referring to  $S_1$  ( $S_2$ ) as follows

$$S_{\substack{1 \\ (2)}} = \left\{ \left( \begin{array}{c} x_1^\mu(u, v) \\ x_2^\mu(u, v) \end{array} \right) = \left( \begin{array}{c} r_{1q}^\mu + u n_{\oplus}^\mu + v r_1^\mu \\ r_{2q}^\mu + u n_{\ominus}^\mu + v r_2^\mu \end{array} \right), \quad u \in [-T, T], \quad v \in [0, 1] \right\}, \quad (2.5.2)$$

where

$$\left( \begin{array}{c} n_{\oplus}^\mu \\ n_{\ominus}^\mu \end{array} \right) := \left( \begin{array}{c} 1 \\ \vec{0} \\ \begin{smallmatrix} + \\ - \end{smallmatrix} 1 \end{array} \right), \quad \left( \begin{array}{c} r_{1q}^\mu \\ r_{2q}^\mu \end{array} \right) := \left( \begin{array}{c} 0 \\ \vec{r}_{1q} \\ 0 \end{array} \right), \quad \text{and} \quad \left( \begin{array}{c} r_1^\mu \\ r_2^\mu \end{array} \right) := \left( \begin{array}{c} 0 \\ \vec{r}_1 \\ 0 \end{array} \right). \quad (2.5.3)$$

The infinitesimally thin tube is neglected since it does not contribute to the  $\chi$ -function. The computation of the  $\chi$ -function requires only the parametrized parts of the minimal surfaces (2.5.2), the corresponding infinitesimal surface elements

$$d\sigma^{\mu\nu} = \left( \frac{\partial x^\mu}{\partial u} \frac{\partial x^\nu}{\partial v} - \frac{\partial x^\mu}{\partial v} \frac{\partial x^\nu}{\partial u} \right) du dv = \left( n_{\oplus}^\mu r_1^\nu - r_1^\mu n_{\oplus}^\nu \right) du dv, \quad (2.5.4)$$

and the limit  $T \rightarrow \infty$  which is appropriate since the correlation length  $a$  is much smaller (see Sec. 2.7) than the longitudinal extension of the loops.

## $\chi_c^{NP}$ -Computation

Starting with the confining component

$$\begin{aligned} \chi_c^{NP} &:= -i \frac{\pi^2}{4} \int_{S_1} d\sigma^{\mu\nu}(x_1) \int_{S_2} d\sigma^{\rho\sigma}(x_2) F_{\mu\nu\rho\sigma}^{NP(c)}(z = x_1 - x_2) \\ &= -\frac{\pi^2 G_2 \kappa}{12(N_c^2 - 1)} \int_{S_1} d\sigma^{\mu\nu}(x_1) \int_{S_2} d\sigma^{\rho\sigma}(x_2) (g_{\mu\rho} g_{\nu\sigma} - g_{\mu\sigma} g_{\nu\rho}) iD(z^2/a^2), \end{aligned} \quad (2.5.5)$$

one exploits the anti-symmetry of the surface elements,  $d\sigma^{\mu\nu} = -d\sigma^{\nu\mu}$ , and applies the surface parametrization (2.5.2) with the corresponding surface elements (2.5.4) to obtain

$$\chi_c^{NP} = \frac{\pi^2 G_2 \kappa}{3(N_c^2 - 1)} 2 (\vec{r}_1 \cdot \vec{r}_2) \int_0^1 dv_1 \int_0^1 dv_2 \lim_{T \rightarrow \infty} \int_{-T}^T du_1 \int_{-T}^T du_2 iD(z^2/a^2), \quad (2.5.6)$$

where

$$z^\mu = x_1^\mu - x_2^\mu = u_1 n_{\oplus}^\mu - u_2 n_{\ominus}^\mu + r_{1q}^\mu - r_{2q}^\mu + v_1 r_1^\mu - v_2 r_2^\mu, \quad (2.5.7)$$

and the identities  $n_{\oplus} \cdot r_2 = r_1 \cdot n_{\ominus} = 0$  and  $n_{\oplus} \cdot n_{\ominus} = 2$ , evident from (2.5.3), have been used. Next, one Fourier transforms the correlation function and performs the  $u_1$  and  $u_2$  integrations in the limit  $T \rightarrow \infty$

$$\begin{aligned}
& \lim_{T \rightarrow \infty} \int_{-T}^T du_1 \int_{-T}^T du_2 iD(z^2/a^2) \\
&= \int \frac{d^4 k}{(2\pi)^4} i\tilde{D}(k^2) \lim_{T \rightarrow \infty} \int_{-T}^T du_1 \int_{-T}^T du_2 e^{-ikz} \\
&= \int \frac{d^4 k}{(2\pi)^2} i\tilde{D}(k^2) \exp[-ik_{\mu}(r_{1q}^{\mu} - r_{2q}^{\mu} + v_1 r_1^{\mu} - v_2 r_2^{\mu})] \delta(k^0 - k^3) \delta(k^0 + k^3) \\
&= \frac{1}{2} iD^{(2)}(\vec{r}_{1q} + v_1 \vec{r}_1 - \vec{r}_{2q} - v_2 \vec{r}_2) , \tag{2.5.8}
\end{aligned}$$

where  $iD^{(2)}$  is the confining correlation function in the two-dimensional transverse space (cf. Appendix C)

$$D^{(2)}(\vec{z}_{\perp}) = \int \frac{d^2 k_{\perp}}{(2\pi)^2} e^{i\vec{k}_{\perp} \cdot \vec{z}_{\perp}} \tilde{D}^{(2)}(\vec{k}_{\perp}) . \tag{2.5.9}$$

The contributions along the light-cone coordinates have been integrated out so that  $\chi_c^{NP}$  is completely determined by the transverse projection of the minimal surfaces. Inserting (2.5.8) into (2.5.6), one finally obtains

$$\chi_c^{NP} = \frac{\pi^2 G_2}{3(N_c^2 - 1)} \kappa(\vec{r}_1 \cdot \vec{r}_2) \int_0^1 dv_1 \int_0^1 dv_2 iD^{(2)}(\vec{r}_{1q} + v_1 \vec{r}_1 - \vec{r}_{2q} - v_2 \vec{r}_2) . \tag{2.5.10}$$

With  $\tilde{D}^{(2)}(\vec{k}_{\perp})$  obtained from the exponential correlation function (2.4.10), cf. Appendix C, we find

$$iD^{(2)}(\vec{z}_{\perp}) = 2\pi a^2 [1 + (|\vec{z}_{\perp}|/a)] \exp(-|\vec{z}_{\perp}|/a) \tag{2.5.11}$$

which is positive for all transverse distances.

## $\chi_{nc}^{NP}$ -Computation

Continuing with the computation of the non-confining component

$$\begin{aligned}
\chi_{nc}^{NP} &:= -i \frac{\pi^2}{4} \int_{S_1} d\sigma^{\mu\nu}(x_1) \int_{S_2} d\sigma^{\rho\sigma}(x_2) F_{\mu\nu\rho\sigma}^{NP(nc)}(z = x_1 - x_2) \\
&= \frac{\pi^2 G_2 (1 - \kappa)}{12(N_c^2 - 1)} \int_{S_1} d\sigma^{\mu\nu}(x_1) \int_{S_2} d\sigma^{\rho\sigma}(x_2) \\
&\quad \times \int \frac{d^4 k}{(2\pi)^4} e^{-ikz} \left[ k_{\nu} k_{\sigma} g_{\mu\rho} - k_{\nu} k_{\rho} g_{\mu\sigma} + k_{\mu} k_{\rho} g_{\nu\sigma} - k_{\mu} k_{\sigma} g_{\nu\rho} \right] i\tilde{D}'_1(k^2) , \tag{2.5.12}
\end{aligned}$$

we exploit again the anti-symmetry of both surface elements to obtain

$$\begin{aligned}\chi_{nc}^{NP} &= \frac{\pi^2 G_2 (1 - \kappa)}{3(N_c^2 - 1)} \int_0^1 dv_1 \int_0^1 dv_2 \int \frac{d^4 k}{(2\pi)^4} \lim_{T \rightarrow \infty} \int_{-T}^T du_1 \int_{-T}^T du_2 e^{-ikz} \\ &\quad \times \left[ 2(r_1 \cdot k)(r_2 \cdot k) - (\vec{r}_1 \cdot \vec{r}_2)(k^0 - k^3)(k^0 + k^3) \right] i\tilde{D}'_1(k^2) \quad (2.5.13)\end{aligned}$$

with  $z$  as given in (2.5.7). Again the identities  $n_{\oplus} \cdot r_2 = r_1 \cdot n_{\ominus} = 0$  and  $n_{\oplus} \cdot n_{\ominus} = 2$  have been used. Performing the  $u_1$  and  $u_2$  integrations in the limit  $T \rightarrow \infty$ , one obtains — as in (2.5.8) — two  $\delta$ -functions which allow us to carry out the integrations over  $k^0$  and  $k^3$  immediately. This leads to

$$\begin{aligned}\chi_{nc}^{NP} &= \frac{\pi^2 G_2 (1 - \kappa)}{3(N_c^2 - 1)} \int_0^1 dv_1 \int_0^1 dv_2 \int \frac{d^2 k_{\perp}}{(2\pi)^2} i\tilde{D}'_1^{(2)}(\vec{k}_{\perp}^2) (\vec{r}_1 \cdot \vec{k}_{\perp})(\vec{r}_2 \cdot \vec{k}_{\perp}) e^{i\vec{k}_{\perp}(\vec{r}_{1q} + v_1 \vec{r}_1 - \vec{r}_{2q} - v_2 \vec{r}_2)} \\ &= \frac{\pi^2 G_2 (1 - \kappa)}{3(N_c^2 - 1)} \int_0^1 dv_1 \frac{\partial}{\partial v_1} \int_0^1 dv_2 \frac{\partial}{\partial v_2} iD'_1^{(2)}(\vec{r}_{1q} + v_1 \vec{r}_1 - \vec{r}_{2q} - v_2 \vec{r}_2), \quad (2.5.14)\end{aligned}$$

where  $iD'_1^{(2)}$  is the non-confining correlation function in transverse space defined analogously to (2.5.9). The  $v_1$  and  $v_2$  integrations are trivial and lead (cf. Fig. 2.1b) to

$$\begin{aligned}\chi_{nc}^{NP} &= \frac{\pi^2 G_2}{3(N_c^2 - 1)} (1 - \kappa) \left[ iD'_1^{(2)}(\vec{r}_{1q} - \vec{r}_{2q}) + iD'_1^{(2)}(\vec{r}_{1\bar{q}} - \vec{r}_{2\bar{q}}) \right. \\ &\quad \left. - iD'_1^{(2)}(\vec{r}_{1q} - \vec{r}_{2\bar{q}}) - iD'_1^{(2)}(\vec{r}_{1\bar{q}} - \vec{r}_{2q}) \right]. \quad (2.5.15)\end{aligned}$$

Using  $\tilde{D}'_1^{(2)}(\vec{k}_{\perp}^2)$ , derived from the exponential correlation function (2.4.10) in Appendix C, we obtain

$$iD'_1^{(2)}(\vec{z}_{\perp}) = \pi a^4 [3 + 3(|\vec{z}_{\perp}|/a) + (|\vec{z}_{\perp}|/a)^2] \exp(-|\vec{z}_{\perp}|/a). \quad (2.5.16)$$

The non-perturbative components,  $\chi_c^{NP}$  and  $\chi_{nc}^{NP}$ , lead to *color transparency* for small dipoles, i.e. a dipole-dipole cross section with  $\sigma_{DD}(\vec{r}_1, \vec{r}_2) \propto |\vec{r}_1|^2 |\vec{r}_2|^2$  for  $|\vec{r}_{1,2}| \rightarrow 0$ , as known for the perturbative case [69]. This will be shown in Sec. 3.2.

## $\chi^P$ -Computation

The perturbative component  $\chi^P$  is defined as

$$\chi^P := -i \frac{\pi^2}{4} \int_{S_1} d\sigma^{\mu\nu}(x_1) \int_{S_2} d\sigma^{\rho\sigma}(x_2) F_{\mu\nu\rho\sigma}^P(z = x_1 - x_2)$$

$$\begin{aligned}
&= \frac{g^2}{4} \int_{S_1} d\sigma^{\mu\nu}(x_1) \int_{S_2} d\sigma^{\rho\sigma}(x_2) \\
&\quad \times \int \frac{d^4 k}{(2\pi)^4} e^{-ikz} \left[ k_\nu k_\sigma g_{\mu\rho} - k_\nu k_\rho g_{\mu\sigma} + k_\mu k_\rho g_{\nu\sigma} - k_\mu k_\sigma g_{\nu\rho} \right] i\tilde{D}'_P(k^2) ,
\end{aligned} \tag{2.5.17}$$

and shows a structure identical to the one of  $\chi_{nc}^{NP}$  given in (2.5.13). Accounting for the different prefactors and the different correlation function, the result for  $\chi_{nc}^{NP}$  (2.5.15) can be used to obtain

$$\begin{aligned}
\chi^P = & \left[ g^2(\vec{r}_{1q} - \vec{r}_{2q}) iD'_P^{(2)}(\vec{r}_{1q} - \vec{r}_{2q}) + g^2(\vec{r}_{1\bar{q}} - \vec{r}_{2\bar{q}}) iD'_P^{(2)}(\vec{r}_{1\bar{q}} - \vec{r}_{2\bar{q}}) \right. \\
& \left. - g^2(\vec{r}_{1q} - \vec{r}_{2\bar{q}}) iD'_P^{(2)}(\vec{r}_{1q} - \vec{r}_{2\bar{q}}) - g^2(\vec{r}_{1\bar{q}} - \vec{r}_{2q}) iD'_P^{(2)}(\vec{r}_{1\bar{q}} - \vec{r}_{2q}) \right] ,
\end{aligned} \tag{2.5.18}$$

where the running coupling  $g^2(\vec{z}_\perp)$  is understood as given in (2.4.5). With (2.4.4) one obtains the perturbative correlation function in transverse space

$$iD'_P^{(2)}(\vec{z}_\perp) = \frac{1}{2\pi} K_0(m_G|\vec{z}_\perp|) , \tag{2.5.19}$$

where  $K_0$  denotes the 0<sup>th</sup> modified Bessel function (McDonald function).

In contrast to the confining component  $\chi_c^{NP}$ , the non-confining components,  $\chi_{nc}^{NP}$  and  $\chi^P$ , depend only on the transverse position between the quark and antiquark of the two dipoles and are therefore independent of the surface choice.

Finally, we explain that the vanishing of  $\chi_{S_1 S_1}$  and  $\chi_{S_2 S_2}$  anticipated in Sec. 2.3 results from the light-like loops and the tensor structures in  $F_{\mu\nu\rho\sigma}$ . Concentrating — without loss of generality — on  $\chi_{S_1 S_1}$ , the appropriate infinitesimal surface elements (2.5.4) and the  $F_{\mu\nu\rho\sigma}$ -ansatz given in (2.4.1), (2.4.6), and (2.4.3) are inserted into (2.2.14). Having simplified the resulting expression by exploiting the anti-symmetry of the surface elements, one finds only terms proportional to  $n_\oplus^2$ ,  $n_\oplus \cdot r_1$ , and  $n_\oplus \cdot z$  with  $z^\mu = x_1^\mu - x_2^\mu = (u_1 - u_2)n_\oplus^\mu + (v_1 - v_2)r_1^\mu$ . Since  $n_\oplus^2 = 0$  and  $n_\oplus \cdot r_1 = 0$ , which is evident from (2.5.3), all terms vanish and  $\chi_{S_1 S_1} = 0$  is derived.

Note that  $\chi = \chi^P + \chi_{nc}^{NP} + \chi_c^{NP}$  is a real-valued function. Since, in addition, the wave functions  $|\psi_i(z_i, \vec{r}_i)|^2$  used in this work (cf. Appendix B) are invariant under the replacement  $(\vec{r}_i \rightarrow -\vec{r}_i, z_i \rightarrow 1 - z_i)$ , the  $T$ -matrix element (2.1.2) upon inserting the results (2.2.15) and (2.3.20) becomes purely imaginary and reads for  $N_c = 3$

$$\begin{aligned}
T(s, t) = & 2is \int d^2 b_\perp e^{i\vec{q}_\perp \cdot \vec{b}_\perp} \int dz_1 d^2 r_1 \int dz_2 d^2 r_2 |\psi_1(z_1, \vec{r}_1)|^2 |\psi_2(z_2, \vec{r}_2)|^2 \\
& \times \left[ 1 - \frac{2}{3} \cos\left(\frac{1}{3}\chi(\vec{b}_\perp, z_1, \vec{r}_1, z_2, \vec{r}_2)\right) - \frac{1}{3} \cos\left(\frac{2}{3}\chi(\vec{b}_\perp, z_1, \vec{r}_1, z_2, \vec{r}_2)\right) \right] .
\end{aligned} \tag{2.5.20}$$

The real part averages out in the integration over  $\vec{r}_i$  and  $z_i$  since the  $\chi$ -function changes sign

$$\chi(\vec{b}_\perp, 1 - z_1, -\vec{r}_1, z_2, \vec{r}_2) = -\chi(\vec{b}_\perp, z_1, \vec{r}_1, z_2, \vec{r}_2), \quad (2.5.21)$$

which can be seen directly from (2.5.10),(2.5.15) and (2.5.18) as  $(\vec{r}_1 \rightarrow -\vec{r}_1, z_1 \rightarrow 1 - z_1)$  implies  $\vec{r}_{1q} \rightarrow \vec{r}_{1\bar{q}}$ . In physical terms,  $(\vec{r}_i \rightarrow -\vec{r}_i, z_i \rightarrow 1 - z_i)$  corresponds to *charge conjugation* i.e. the replacement of each parton with its antiparton and the associated reversal of the loop direction.

Consequently, the  $T$ -matrix (2.5.20) describes only charge conjugation  $C = +1$  exchange. Since in our quenched approximation purely gluonic interactions are modelled, (2.5.20) describes only pomeron<sup>6</sup> but not reggeon exchange.

## 2.6 Energy Dependence

Up to now the  $T$ -matrix element (2.5.20) leads to energy-independent total cross sections in contradiction to the experimental observation. This is disappointing from the phenomenological point of view but not surprising since our formalism does not describe gluon radiation which would generate the energy dependence. Nevertheless, we introduce the energy dependence in a phenomenological way inspired by other successful models so that a unified description of hadron-hadron, photon-proton, and photon-photon reactions is achieved. The powerlike ansatz used for the energy dependence is crucial to guarantee the Froissart bound [7] as shown in chapter 4.

Most models for high-energy scattering are constructed to describe either hadron-hadron or photon-hadron reactions. For example, Kopeliovich et al. [70] as well as Berger and Nachtmann [14] focus on hadron-hadron scattering. In contrast, Golec-Biernat and Wüsthoff [71, 72] and Forshaw, Kerley, and Shaw [73] concentrate on photon-proton reactions. A model that describes the energy dependence in both hadron-hadron and photon-hadron reactions up to large photon virtualities is the two-pomeron model of Donnachie and Landshoff [28]. Based on Regge theory, they find hard pomeron trajectory with intercept  $1 + \epsilon_{hard} \approx 1.4$  that governs the strong energy dependence of  $\gamma^* p$  reactions with high  $Q^2$  and a soft pomeron trajectory with intercept  $1 + \epsilon_{soft} \approx 1.08$  that governs the weak energy dependence of hadron-hadron or  $\gamma^* p$  reactions with low  $Q^2$ . Similarly, we aim at a simultaneous description

---

<sup>6</sup>Odderon  $C = -1$  exchange is excluded in our model. It would survive in the following cases:  
 (a) Wave functions are used that are not invariant under the transformation  $(\vec{r}_i \rightarrow -\vec{r}_i, z_i \rightarrow 1 - z_i)$ .  
 (b) The proton is described as a system of three quarks with finite separations modelled by three loops with one common light-like line. (c) The Gaussian approximation that enforces the truncation of the cumulant expansion is relaxed and additional higher cumulants are taken into account.

of hadron-hadron, photon-proton, and photon-photon reactions involving real and virtual photons as well.

In line with other two-component (hard + soft) models [21, 22, 28, 73, 74] and the different hadronization mechanisms in hard and soft collisions, our physical ansatz demands that the perturbative and non-perturbative contributions do not interfere. Therefore, we modify the cosine-summation in (2.5.20) allowing only even numbers of soft and hard correlations,  $(\chi^P)^{2n} (\chi^{NP})^{2m}$  with  $n, m \in \mathbb{N}$ . Interference terms with odd numbers of hard and soft correlations are subtracted by the replacement

$$\cos [c\chi] = \cos [c(\chi^P + \chi^{NP})] \rightarrow \cos [c\chi^P] \cos [c\chi^{NP}] , \quad (2.6.1)$$

where  $c = 1/3$  or  $2/3$ . This prescription leads to the following factorization of soft and hard physics in the  $T$ -matrix element (2.5.20),

$$\begin{aligned} T(s, t) &= 2is \int d^2 b_\perp e^{i\vec{q}_\perp \vec{b}_\perp} \int dz_1 d^2 r_1 \int dz_2 d^2 r_2 |\psi_1(z_1, \vec{r}_1)|^2 |\psi_2(z_2, \vec{r}_2)|^2 \\ &\times \left[ 1 - \frac{2}{3} \cos\left(\frac{1}{3}\chi^P\right) \cos\left(\frac{1}{3}\chi^{NP}\right) - \frac{1}{3} \cos\left(\frac{2}{3}\chi^P\right) \cos\left(\frac{2}{3}\chi^{NP}\right) \right] . \end{aligned} \quad (2.6.2)$$

In the limit of small  $\chi$ -functions,  $|\chi^P| \ll 1$  and  $|\chi^{NP}| \ll 1$ , one gets

$$\begin{aligned} T(s, t) &= 2is \int d^2 b_\perp e^{i\vec{q}_\perp \vec{b}_\perp} \int dz_1 d^2 r_1 \int dz_2 d^2 r_2 |\psi_1(z_1, \vec{r}_1)|^2 |\psi_2(z_2, \vec{r}_2)|^2 \\ &\times \frac{1}{9} \left[ (\chi^P)^2 + (\chi^{NP})^2 \right] . \end{aligned} \quad (2.6.3)$$

In this limit, the  $T$ -matrix element evidently becomes a sum of a perturbative and a non-perturbative component. We show in the following chapter that the perturbative correlations,  $(\chi^P)^2$ , describe the well-known *two-gluon exchange* [34, 35] to dipole-dipole scattering and the non-perturbative correlations,  $(\chi^{NP})^2$ , the corresponding non-perturbative two-point interactions.

As the two-component structure of (2.6.3) reminds of the two-pomeron model of Donnachie and Landshoff [28], we adopt the powerlike energy increase and ascribe a strong energy dependence to the perturbative component  $\chi^P$  and a weak one to the non-perturbative component  $\chi^{NP}$

$$\begin{aligned} (\chi^P)^2 &\rightarrow (\chi^P(s))^2 := (\chi^P)^2 \left( \frac{s}{s_0} \frac{\vec{r}_1^2 \vec{r}_2^2}{R_0^4} \right)^{\epsilon^P} \\ (\chi^{NP})^2 &\rightarrow (\chi^{NP}(s))^2 := (\chi^{NP})^2 \left( \frac{s}{s_0} \frac{\vec{r}_1^2 \vec{r}_2^2}{R_0^4} \right)^{\epsilon^{NP}} \end{aligned} \quad (2.6.4)$$

with the scaling factor  $s_0 R_0^4$ . The powerlike energy dependence with the exponents  $0 \approx \epsilon^{NP} < \epsilon^P < 1$  guarantees Regge type behavior at moderately high energies, where the small- $\chi$  limit (2.6.3) is appropriate. In (2.6.4), the energy variable  $s$  is scaled by the factor  $\vec{r}_1^2 \vec{r}_2^2$  that allows to rewrite the energy dependence in photon-hadron scattering in terms of the appropriate Bjorken scaling variable  $x$

$$s \vec{r}_1^2 \propto \frac{s}{Q^2} = \frac{1}{x}, \quad (2.6.5)$$

where  $|\vec{r}_1|$  is the transverse extension of the  $q\bar{q}$  dipole in the photon. A similar factor has been used before in the dipole model of Forshaw, Kerley, and Shaw [73] and also in the model of Donnachie and Dosch [74] in order to respect the scaling properties observed in the structure function of the proton.<sup>7</sup> In the dipole-proton cross section of Golec-Biernat and Wüsthoff [71, 72], Bjorken  $x$  is used directly as energy variable which is important for the success of the model. In fact, also in our model, the  $\vec{r}_1^2 \vec{r}_2^2$  factor improves the description of  $\gamma^* p$  reactions at large  $Q^2$ .

The powerlike Regge type energy dependence (2.6.4) can be derived in more theoretical frameworks: A powerlike energy dependence is found for hadronic reactions by Kopeliovich et al. [70] and for hard photon-proton reactions from the BFKL equation [75]. However, these approaches need unitarization since their powerlike energy dependence will ultimately violate  $S$ -matrix unitarity at asymptotic energies. In our model, we use the following  $T$ -matrix element as the basis for chapter 4 and 5

$$\begin{aligned} T(s, t) = & 2is \int d^2 b_\perp e^{i\vec{q}_\perp \vec{b}_\perp} \int dz_1 d^2 r_1 \int dz_2 d^2 r_2 |\psi_1(z_1, \vec{r}_1)|^2 |\psi_2(z_2, \vec{r}_2)|^2 \\ & \times \left[ 1 - \frac{2}{3} \cos\left(\frac{1}{3}\chi^P(s)\right) \cos\left(\frac{1}{3}\chi^{NP}(s)\right) - \frac{1}{3} \cos\left(\frac{2}{3}\chi^P(s)\right) \cos\left(\frac{2}{3}\chi^{NP}(s)\right) \right]. \end{aligned} \quad (2.6.6)$$

Here the cosine functions in combination with the powerlike energy ansatz ensure the  $S$ -matrix unitarity in impact parameter space and the Froissart bound [7] as shown in chapter 4. Furthermore, the multiple gluonic interactions associated with the higher order terms in the expansion of the cosine functions provide the mechanism which leads to saturation effects in cross sections at ultra-high energies.

Having ascribed the energy dependence to the  $\chi$ -function, the energy behavior of hadron-hadron, photon-hadron, and photon-photon scattering results exclusively from the *universal* loop-loop correlation function  $S_{DD}$ . In this way a unified description of hadronic and photonic interactions is achieved.

---

<sup>7</sup>In the model of Donnachie and Dosch [74],  $s |\vec{r}_1| |\vec{r}_2|$  is used as the energy variable if both dipoles are small, which is in accordance with the choice of the typical BFKL energy scale but leads to discontinuities in the dipole-dipole cross section. In order to avoid such discontinuities, we use the energy variable (2.6.4) also for the scattering of two small dipoles.

## 2.7 Model Parameters

Lattice QCD simulations provide important information and constraints on the model parameters. The fine tuning of the parameters was, however, directly performed on the high-energy scattering data for hadron-hadron, photon-hadron, and photon-photon reactions where an error ( $\chi^2$ ) minimization was not feasible because of the non-trivial multi-dimensional integrals in the  $T$ -matrix element (2.6.6).

The parameters  $a$ ,  $\kappa$ ,  $G_2$ ,  $m_G$ ,  $M^2$ ,  $s_0 R_0^4$ ,  $\epsilon^{NP}$  and  $\epsilon^P$  determine the dipole-dipole scattering and are universal for all reactions described. In addition, there are reaction-dependent parameters associated with the wave functions which are provided in Appendix B.

The perturbative component involves the gluon mass  $m_G$  as IR regulator (or inverse “perturbative correlation length”) and the parameter  $M^2$  that freezes the running coupling (2.4.5) for large distance scales. We adopt the parameters

$$m_G = m_\rho = 0.77 \text{ GeV} \quad \text{and} \quad M^2 = 1.04 \text{ GeV}^2. \quad (2.7.1)$$

The value of the gluon mass is important for the interplay between the perturbative and non-perturbative contribution. Using our perturbative component, it gives a reasonable “perturbative glueball mass” (GB) of  $M_{GB}^P = 2m_G = 1.54 \text{ GeV}$ . The value of the parameter  $M^2$  in (2.7.1) that fixes the running coupling at large distances at  $\alpha_s = 0.4$  is taken from [76].

The non-perturbative component involves the correlation length  $a$ , the gluon condensate  $G_2$ , and the parameter  $\kappa$  indicating the non-Abelian character of the correlator. With the simple exponential correlation functions specified in Euclidean space-time (2.4.10), we obtain the following values for the parameters of the non-perturbative correlator (2.4.6)

$$a = 0.302 \text{ fm}, \quad \kappa = 0.74, \quad G_2 = 0.074 \text{ GeV}^4, \quad (2.7.2)$$

and, correspondingly, the string tension for the fundamental representation of  $SU(3)$  becomes

$$\sigma_3 = \frac{\pi^3 \kappa G_2 a^2}{18} = 0.22 \text{ GeV}^2 \equiv 1.12 \text{ GeV/fm}, \quad (2.7.3)$$

which is consistent with hadron spectroscopy [61], Regge theory [62], and lattice QCD investigations [26]. Using the above value for the correlation length, the non-perturbative component generates a “non-perturbative glueball mass” of  $M_{GB}^{NP} = 2/a = 1.31 \text{ GeV}$  that is smaller than the “perturbative glueball mass”  $M_{GB}^P$  and thus governs the long-range interactions as expected.

Lattice QCD computations of the gluon field strength correlator down to distances of 0.4 fm have obtained the following values with the exponential correlation function (2.4.10) [25]:  $a = 0.219$  fm,  $\kappa = 0.746$ ,  $G_2 = 0.173$  GeV $^4$ . This value for  $\kappa$  is in agreement with the one in (2.7.2), while the fit to high-energy scattering data clearly requires a larger value for  $a$  and a smaller value for  $G_2$ .

The energy dependence of the model is associated with the energy exponents  $\epsilon^{NP}$  and  $\epsilon^P$ , and the scaling parameter  $s_0 R_0^4$

$$\epsilon^{NP} = 0.125, \quad \epsilon^P = 0.73, \quad \text{and} \quad s_0 R_0^4 = (47 \text{ GeV fm}^2)^2. \quad (2.7.4)$$

In comparison with the energy exponents of Donnachie and Landshoff [28, 29],  $\epsilon_{soft} \approx 0.08$  and  $\epsilon_{hard} \approx 0.4$ , our exponents are larger. However, the cosine functions in our  $T$ -matrix element (2.6.6) reduce the large exponents so that the energy dependence of the cross sections agrees with the experimental data as illustrated in chapter 5.

We have fixed the above parameters by trying to reproduce as many experimental observables as possible. The numerous observables can, of course, only narrow the range of the parameters. Additional constraints have been lattice QCD simulations and other models. Nonetheless, since an error ( $\chi^2$ ) minimization has not been possible, the given parameter values cannot be mandatory.

# Chapter 3

## Anatomy of QCD Strings and Unintegrated Gluon Distributions

In this chapter we investigate the QCD structure of the perturbative and non-perturbative dipole-dipole interaction in momentum space within our loop-loop correlation model. We reproduce the known results for perturbative interactions between the dipoles and give new insights into non-perturbative interactions between QCD strings which lead to quark-confinement in dipoles. Non-perturbative string-string interactions show a new structure different from perturbative dipole-dipole interactions. The confining QCD string exhibits a very nice feature: It can be exactly represented as a collection of stringless quark-antiquark dipoles. This outstanding result allows us to extract the microscopic structure of unintegrated gluon distributions of hadrons and photons. Our unintegrated gluon distribution of the proton is compared with those obtained in other approaches. Confining QCD string manifestations are shown explicitly in dipole-hadron cross sections and unintegrated gluon distributions. The  $|\vec{k}_\perp|$ -factorization, known in perturbative physics, is found to be valid also in non-perturbative interactions within our model.

The structural aspects exposed in this chapter have been possible because of the simple minimal surfaces (see Fig. 2.1) used in our model. The previous complicated pyramid mantle choice of the surfaces [13, 14, 18–23] did not allow such studies.

We consider throughout this chapter only the lowest order contribution to dipole-dipole interactions, i.e., the small- $\chi$  limit of the  $T$ -matrix element (2.6.3). With a phenomenological energy dependence assigned to the  $\chi$ -functions as discussed in Sec. 2.6, this limit can be used to describe experimental observables for  $x =$

$Q^2/s \geq 10^{-4}$ . For lower Bjorken- $x$  (higher c.m. energy) values, the exact  $T$ -matrix element (2.6.6) is needed to ensure  $S$ -matrix unitarity conditions and to observe saturation effects in high-energy reactions as discussed in chapter 4 and 5.

### 3.1 QCD Structure of Dipole-Dipole Scattering in Momentum Space

The total dipole-dipole cross section in the small- $\chi$  limit is obtained from Eq. (2.6.3) via the optical theorem

$$\begin{aligned}\sigma_{DD}^{tot}(s_0) &= \frac{1}{s_0} \text{Im } T(s_0, t=0) \\ &= 2 \int d^2 b_\perp \int dz_1 d^2 r_1 \int dz_2 d^2 r_2 |\psi_{D_1}(z_1, \vec{r}_1)|^2 |\psi_{D_2}(z_2, \vec{r}_2)|^2 \\ &\quad \times \frac{1}{9} \left[ (\chi^P)^2 + (\chi_{nc}^{NP} + \chi_c^{NP})^2 \right],\end{aligned}\quad (3.1.1)$$

where  $\sqrt{s_0} \approx 20$  GeV denotes the c.m. energy at which our model (2.6.2) reproduces the experimental observables. The dipoles in Eq. (3.1.1) have fixed  $z_i$  and  $|\vec{r}_i|$  values

$$|\psi_{D_i}(z_i, \vec{r}_i)|^2 = \frac{1}{2\pi|\vec{r}_{D_i}|} \delta(|\vec{r}_i| - |\vec{r}_{D_i}|) \delta(z_i - z_{D_i}) \quad (3.1.2)$$

but are averaged over all orientations. Being interested in the momentum-space structure of the scattering, we use (2.5.9) to write the  $\chi$ -functions computed with minimal surfaces in the previous chapter, see (2.5.10), (2.5.15), (2.5.18), in the form

$$\begin{aligned}\chi^P &= 4\pi \int \frac{d^2 k_\perp}{(2\pi)^2} \alpha_s(k_\perp^2) i\tilde{D}_P^{(2)}(k_\perp^2) \left[ e^{i\vec{k}_\perp(\vec{r}_{1q}-\vec{r}_{2q})} + e^{i\vec{k}_\perp(\vec{r}_{1\bar{q}}-\vec{r}_{2\bar{q}})} \right. \\ &\quad \left. - e^{i\vec{k}_\perp(\vec{r}_{1q}-\vec{r}_{2\bar{q}})} - e^{i\vec{k}_\perp(\vec{r}_{1\bar{q}}-\vec{r}_{2q})} \right]\end{aligned}\quad (3.1.3)$$

$$\begin{aligned}\chi_{nc}^{NP} &= \frac{\pi^2 G_2 (1-\kappa)}{24} \int \frac{d^2 k_\perp}{(2\pi)^2} i\tilde{D}_1^{(2)}(k_\perp^2) \left[ e^{i\vec{k}_\perp(\vec{r}_{1q}-\vec{r}_{2q})} + e^{i\vec{k}_\perp(\vec{r}_{1\bar{q}}-\vec{r}_{2\bar{q}})} \right. \\ &\quad \left. - e^{i\vec{k}_\perp(\vec{r}_{1q}-\vec{r}_{2\bar{q}})} - e^{i\vec{k}_\perp(\vec{r}_{1\bar{q}}-\vec{r}_{2q})} \right]\end{aligned}\quad (3.1.4)$$

$$\begin{aligned}\chi_c^{NP} &= \frac{\pi^2 G_2 \kappa}{24} (\vec{r}_1 \cdot \vec{r}_2) \int_0^1 dv_1 \int_0^1 dv_2 \int \frac{d^2 k_\perp}{(2\pi)^2} i\tilde{D}^{(2)}(k_\perp^2) e^{i\vec{k}_\perp(\vec{r}_{1q}+v_1\vec{r}_1-\vec{r}_{2q}-v_2\vec{r}_2)}\end{aligned}\quad (3.1.5)$$

with the Minkowskian correlation functions in transverse space

$$i\tilde{D}'^{(2)}_P(k_\perp^2) = \frac{1}{k_\perp^2 + m_G^2}, \quad (3.1.6)$$

$$i\tilde{D}'^{(2)}_1(k_\perp^2) = \frac{30\pi^2}{a(k_\perp^2 + a^{-2})^{\frac{7}{2}}}, \quad (3.1.7)$$

$$i\tilde{D}^{(2)}(k_\perp^2) = \frac{12\pi^2}{a(k_\perp^2 + a^{-2})^{\frac{5}{2}}}. \quad (3.1.8)$$

The perturbative correlation function,  $\tilde{D}'^{(2)}_P(k_\perp^2)$ , results from Eq. (2.4.4) for  $k^0 = k^3 = 0$ , i.e.,  $k^2 = -\vec{k}_\perp^2$ , which is enforced in the computation of  $\chi$  - functions. The derivation of the non-perturbative correlation functions,  $\tilde{D}'^{(2)}_1(k_\perp^2)$  and  $\tilde{D}^{(2)}(k_\perp^2)$ , from Eq. (2.4.10) is shown in Appendix C.

The component  $\chi^P$  describes the perturbative interaction of the quark and anti-quark of one dipole with the quark and antiquark of the other dipole as evident from the  $\vec{r}_{iq}$  and  $\vec{r}_{i\bar{q}}$  dependence of (3.1.3) and Fig. 2.1b. The component  $\chi_{nc}^{NP}$  has the same structure as  $\chi^P$  and gives the non-perturbative interaction between the quarks and antiquarks of the dipoles. With the term quark used generically for quarks and antiquarks in the following, we refer to  $\chi^P$  and  $\chi_{nc}^{NP}$  as *quark-quark interactions*.

The component  $\chi_c^{NP}$  given in Eq. (3.1.5) shows a different structure. Here the integrations over  $v_1$  and  $v_2$  sum non-perturbative interactions between the gluon field strengths connecting the quark and antiquark in each of the two dipoles. These connections are manifestations of the strings that confine the corresponding quark and antiquark in the dipole and are visualized in Fig. 2.1b. Indeed, the non-perturbative component  $\chi_c^{NP}$  shows a flux tube (string) between a static quark-antiquark pair in Euclidean space-time [17, 30, 31] which confines the quark and antiquark in the dipole as explained in chapter 2. Therefore, we understand the confining component  $\chi_c^{NP}$  as a *string-string interaction*.

The mixed contribution  $\chi_{nc}^{NP} \chi_c^{NP}$  that occurs in the dipole-dipole cross section (3.1.1) gives the non-perturbative interaction of the quark and antiquark of one dipole with the string of the other dipole, i.e., it represents the *quark-string interaction*.

To be able to examine the  $|\vec{k}_\perp|$  - structure of dipole-dipole interactions, we carry out all integrations in Eq. (3.1.1) except, of course, the one over transverse momentum  $|\vec{k}_\perp|$  that enters through the  $\chi$ -functions (3.1.3)–(3.1.5). The resulting perturbative ( $P$ ) and non-perturbative ( $NP$ ) integrand of the total dipole-dipole cross

section

$$\sigma_{DD}^{tot}(s_0) = \int d|\vec{k}_\perp| \left[ I^P(s_0, |\vec{k}_\perp|) + I^{NP}(s_0, |\vec{k}_\perp|) \right] \quad (3.1.9)$$

$$= \int d|\vec{k}_\perp| \left[ I^P(s_0, |\vec{k}_\perp|) + I_{qq}^{NP}(s_0, |\vec{k}_\perp|) + I_{ss}^{NP}(s_0, |\vec{k}_\perp|) \right], \quad (3.1.10)$$

show the following momentum-space structure:

$$I^P(s_0, |\vec{k}_\perp|) = \frac{2}{9} \frac{1}{2\pi} |\vec{k}_\perp| (4\pi\alpha_s(k_\perp^2))^2 \left[ i\tilde{D}'^{(2)}(k_\perp^2) \right]^2 \times \left[ 2 \langle \psi_{D_1} | 1 - e^{i\vec{k}_\perp \cdot \vec{r}_1} | \psi_{D_1} \rangle 2 \langle \psi_{D_2} | 1 - e^{i\vec{k}_\perp \cdot \vec{r}_2} | \psi_{D_2} \rangle \right] \quad (3.1.11)$$

$$I_{qq}^{NP}(s_0, |\vec{k}_\perp|) = \frac{2}{9} \frac{1}{2\pi} |\vec{k}_\perp| \left( \frac{\pi^2 G_2}{24} \right)^2 \left[ (1 - \kappa) i\tilde{D}'^{(2)}(k_\perp^2) + \frac{\kappa}{k_\perp^2} i\tilde{D}^{(2)}(k_\perp^2) \right]^2 \times \left[ 2 \langle \psi_{D_1} | 1 - e^{i\vec{k}_\perp \cdot \vec{r}_1} | \psi_{D_1} \rangle 2 \langle \psi_{D_2} | 1 - e^{i\vec{k}_\perp \cdot \vec{r}_2} | \psi_{D_2} \rangle \right] \quad (3.1.12)$$

$$I_{ss}^{NP}(s_0, |\vec{k}_\perp|) = \frac{2}{9} \frac{1}{2\pi} |\vec{k}_\perp| \left( \frac{\pi^2 G_2}{24} \right)^2 \left[ \frac{\kappa}{k_\perp^2} i\tilde{D}^{(2)}(k_\perp^2) \right]^2 \times \left[ 2 \langle \psi_{D_1} | \tan^2 \phi_1 (1 - e^{i\vec{k}_\perp \cdot \vec{r}_1}) | \psi_{D_1} \rangle 2 \langle \psi_{D_2} | \tan^2 \phi_2 (1 - e^{i\vec{k}_\perp \cdot \vec{r}_2}) | \psi_{D_2} \rangle \right] \quad (3.1.13)$$

where the brackets  $\langle \psi_{D_i} | \dots | \psi_{D_i} \rangle$  denote the averages

$$\langle \psi_{D_i} | A_i | \psi_{D_i} \rangle = \int dz_i d^2 r_i |\psi_{D_i}(z_i, \vec{r}_i)|^2 A_i \quad (3.1.14)$$

and the dipole orientation  $\phi_i$  is defined as the angle between transverse momentum  $\vec{k}_\perp$  and dipole vector  $\vec{r}_i$ . With Eq. (3.1.2) the integration over the dipole orientations  $\phi_i$  leads, respectively, to the Bessel function  $J_0(|\vec{k}_\perp| |\vec{r}_{D_i}|)$  and the generalized hypergeometric function<sup>1</sup>  ${}_1F_2(-1/2; 1/2, 1; -k_\perp^2 r_{D_i}^2/4)$

$$\begin{aligned} \langle \psi_{D_i} | 1 - e^{i\vec{k}_\perp \cdot \vec{r}_i} | \psi_{D_i} \rangle &= \frac{1}{2\pi} \int_0^{2\pi} d\phi_i (1 - e^{i\vec{k}_\perp \cdot \vec{r}_{D_i}}) \\ &= 1 - J_0(|\vec{k}_\perp| |\vec{r}_{D_i}|), \end{aligned} \quad (3.1.15)$$

$$\begin{aligned} \langle \psi_{D_i} | \tan^2 \phi_i (1 - e^{i\vec{k}_\perp \cdot \vec{r}_i}) | \psi_{D_i} \rangle &= \frac{1}{2\pi} \int_0^{2\pi} d\phi_i \tan^2 \phi_i (1 - e^{i\vec{k}_\perp \cdot \vec{r}_{D_i}}) \\ &= -1 + {}_1F_2\left(-\frac{1}{2}; \frac{1}{2}, 1; \frac{-k_\perp^2 r_{D_i}^2}{4}\right). \end{aligned} \quad (3.1.16)$$

---

<sup>1</sup>A review of generalized hypergeometric functions can be found in [77]. In the computer program Mathematica [78] “HypergeometricPFQ[{-1/2}, {1/2, 1}, -k\_\perp^2 r\_D^2/4]” denotes this function.

The important implications will be discussed in the following section.

The integrand  $I^P$  given in Eq. (3.1.11) describes the known perturbative two-gluon<sup>2</sup> exchange [34, 35] between the quarks and antiquarks of the two dipoles. The ingredients of  $I^P$  are visualized for one combination of gluon exchanges in Fig. 3.1a: the paired horizontal lines represent the *dipole factors*  $(1 - e^{i\vec{k}_\perp \cdot \vec{r}_i})$  that describe the phase difference between the quark and antiquark at separate transverse positions, the surrounding brackets indicate the average over the dipole orientations (3.1.14), the two curly lines illustrate the gluon propagator squared  $[i\tilde{D}'_P]_i^2$ , and the four vertices (dots) correspond to the strong coupling to the fourth power  $g^4 = (4\pi\alpha_s)^2$ .

The integrand  $I^{NP} = I_{qq}^{NP} + I_{ss}^{NP}$  given in Eqs. (3.1.12) and (3.1.13) describes the non-perturbative interactions: the quark-quark, string-string, and quark-string interactions identified by the appropriate correlation functions  $[i\tilde{D}'_1]_i^2$ ,  $[i\tilde{D}_1]_i^2$ , and  $[i\tilde{D}'_1 i\tilde{D}_1]$ . These interactions are illustrated in Figs. 3.1b, 3.1c and 3.1d, respectively. Analogous to the perturbative interaction in Fig. 3.1a, the dashed and solid zig-zag lines represent, respectively, the non-confining  $(1 - \kappa) i\tilde{D}'_1$  and the confining  $(\kappa/k_\perp^2) i\tilde{D}_1$  non-perturbative correlations, the shaded areas symbolize the strings, and the four vertices (squares) in each figure indicate the "non-perturbative coupling" to the fourth power  $g_{NP}^4 := (\pi^2 G_2/24)^2$ .

The integrand  $I_{qq}^{NP}$  describes the non-perturbative *interactions between the quarks and antiquarks* of the two dipoles and exhibits the same dipole factors  $(1 - e^{i\vec{k}_\perp \cdot \vec{r}_i})$  that appear in the perturbative integrand (3.1.11).  $I_{qq}^{NP}$  contains three components: the non-confining component, the confining component, and their interference term. While the non-confining component visualized in Fig. 3.1b has the same structure as the perturbative contribution, see also Eqs. (3.1.3) and (3.1.4), the confining component shown in its more general form in Fig. 3.1c comes from the interaction between the quarks and antiquarks at the endpoints of the strings, which will be further discussed below Eq. (3.1.17). The interference term describes the quark-string interaction as illustrated in Fig. 3.1d. Note that it reduces entirely to an interaction between the quarks and antiquarks of the dipoles with the additional denominator  $1/k_\perp^2$  generated by the integrations over the variables  $v_1$  and  $v_2$  in the confining component  $\chi_c^{NP}$  given in Eq. (3.1.5).

The integrand  $I_{ss}^{NP}$  describes the non-perturbative *string-string interaction* shown in Fig. 3.1c. The new angular dependencies in the string-string interaction, the modified dipole factors  $\tan^2\phi_i(1 - e^{i\vec{k}_\perp \cdot \vec{r}_{D_i}})$  in Eq. (3.1.13), are obtained as follows. The integrations over  $v_1$ ,  $v_2$ ,  $v'_1$ , and  $v'_2$  in  $(\chi_c^{NP})^2$  produce the dipole factors  $(1 - e^{i\vec{k}_\perp \cdot \vec{r}_i})$

---

<sup>2</sup>The exact  $T$ -matrix element (2.6.6), used to describe scattering processes at ultra-high energies in chapter 5, goes beyond two-gluon exchange due to the higher orders in the cosine expansion.

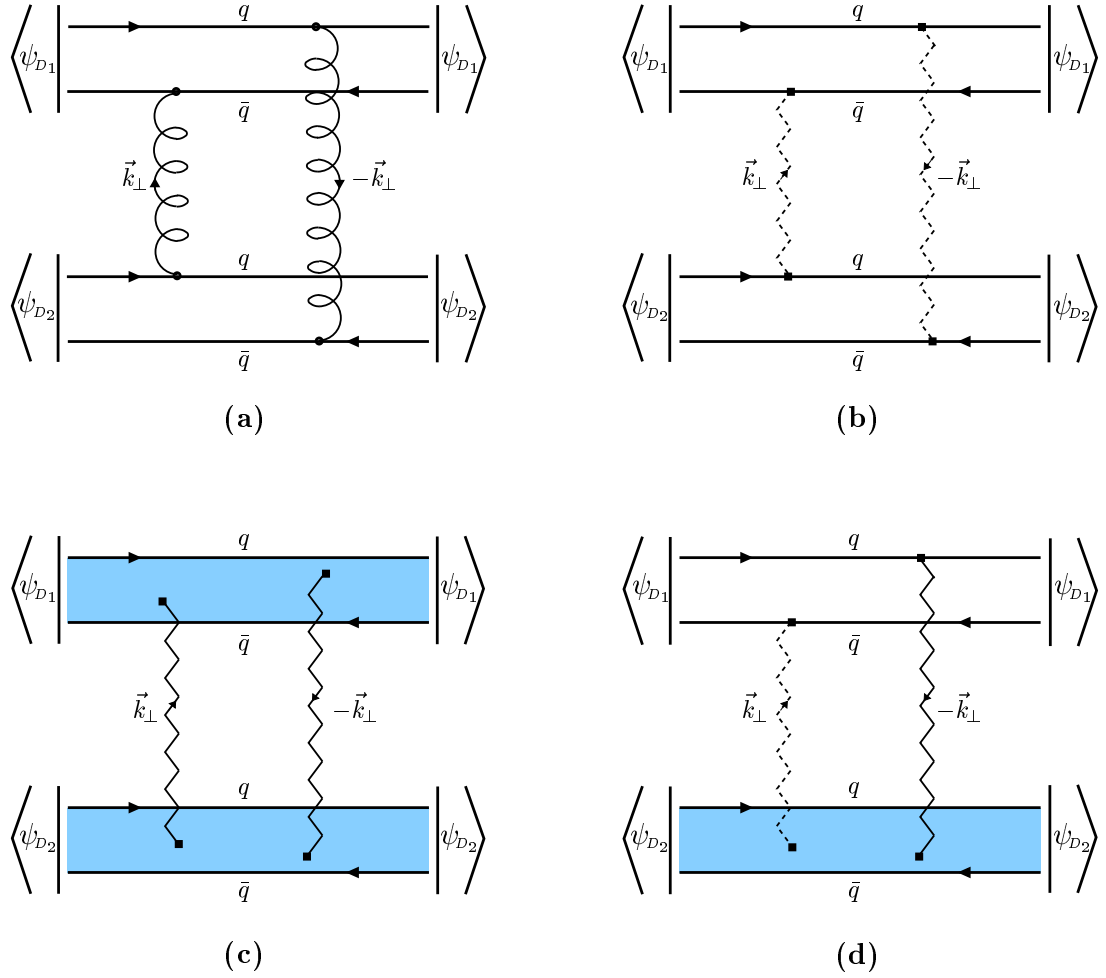


Figure 3.1: Perturbative and non-perturbative contributions to dipole-dipole scattering: **(a)** perturbative quark-quark interaction and non-perturbative **(b)** quark-quark, **(c)** string-string, and **(d)** quark-string interactions. The term quark is used genuinely for quarks and antiquarks. Only one diagram is shown for each type of interaction. Paired horizontal lines represent quark-antiquark dipoles, surrounding brackets indicate the averages over the dipole orientations (3.1.14), shaded areas visualize strings, curly lines denote exchanged perturbative gluons, and dashed and solid zig-zag lines symbolize, respectively, the non-perturbative non-confining and confining correlation functions.

and the denominator  $1/[(\vec{k}_\perp \vec{r}_1)^2 (\vec{k}_\perp \vec{r}_2)^2]$ . This denominator multiplied with the additional factor  $(\vec{r}_1 \vec{r}_2)^2$  from  $(\chi_c^{NP})^2$ , see Eq. (3.1.5), gives the total angular dependence

$$\begin{aligned} \frac{(\vec{r}_1 \vec{r}_2)^2}{(\vec{k}_\perp \vec{r}_1)^2 (\vec{k}_\perp \vec{r}_2)^2} &= \frac{r_1^2 r_2^2 \cos^2(\phi_1 - \phi_2)}{(k_\perp^2 r_1^2 \cos^2 \phi_1) (k_\perp^2 r_2^2 \cos^2 \phi_2)} \\ &= \frac{(\cos \phi_1 \cos \phi_2 + \sin \phi_1 \sin \phi_2)^2}{k_\perp^4 \cos^2 \phi_1 \cos^2 \phi_2} \\ &= \frac{1}{k_\perp^4} (1 + 2 \tan \phi_1 \tan \phi_2 + \tan^2 \phi_1 \tan^2 \phi_2) . \quad (3.1.17) \end{aligned}$$

The first term in Eq. (3.1.17) explains the interaction between the endpoints of the strings with the additional factor  $1/k_\perp^4$  in the first contribution  $I_{qq}^{NP}$  already mentioned above. The product of the second term in Eq. (3.1.17),  $2 \tan \phi_1 \tan \phi_2$ , with the dipole factors vanishes after the integration over the dipole orientations  $\phi_1$  and  $\phi_2$ . The third term in Eq. (3.1.17),  $\tan^2 \phi_1 \tan^2 \phi_2$ , weights the different orientations of the strings and is characteristic for the string-string interaction (3.1.13) in our model. Due to this factor, the string-string interaction differs significantly from the interaction between the quarks and antiquarks of the dipoles known from perturbative two-gluon exchange (3.1.11).

In Fig. 3.2 we show the perturbative integrand  $I^P$  (solid line) and the non-perturbative integrand  $I^{NP}$  (dashed line) of the total dipole-dipole cross section (3.1.10) as a function of transverse momentum  $|\vec{k}_\perp|$  for various dipole sizes. The integrands have been calculated with the model parameters given in Sec. 2.7 that allow a good description of the experimental data of hadron and photon reactions at the c.m. energy of  $\sqrt{s_0} \approx 20$  GeV with the wave functions given in Appendix B and the exact  $T$ -matrix element (2.6.2). Evidently, the non-perturbative integrand  $I^{NP}$  governs the low momenta and the perturbative integrand  $I^P$  the high momenta exchanged in the dipole-dipole scattering. This behavior is a direct consequence of the correlation functions: The non-perturbative correlation functions (3.1.7) and (3.1.8) favor low momenta and suppress high momenta in comparison to the perturbative correlation function (2.4.4). For fixed dipole sizes  $|\vec{r}_{D_1}|$  and  $|\vec{r}_{D_2}|$  the absolute values of the perturbative and non-perturbative integrand are controlled, respectively, by the parameters  $(m_g, M)$  and  $(G_2, a, \kappa)$  given in Sec. 2.7. With decreasing dipole sizes the ratio  $I^P/I^{NP}$  increases: for large dipole sizes  $|\vec{r}_{D_1}| = |\vec{r}_{D_2}| = 1$  fm, the non-perturbative contribution gives the main contribution to the total dipole-dipole cross section; for small dipole sizes  $|\vec{r}_{D_1}| = |\vec{r}_{D_2}| = 0.1$  fm, the perturbative contribution dominates.

As can be seen from the analytic results in Eqs. (3.1.11)–(3.1.16), the total dipole-dipole cross section (3.1.10) or the forward scattering amplitude  $T(s_0, t = 0)$  does not depend on the longitudinal quark momentum fractions  $z_{D_i}$  of the dipoles.

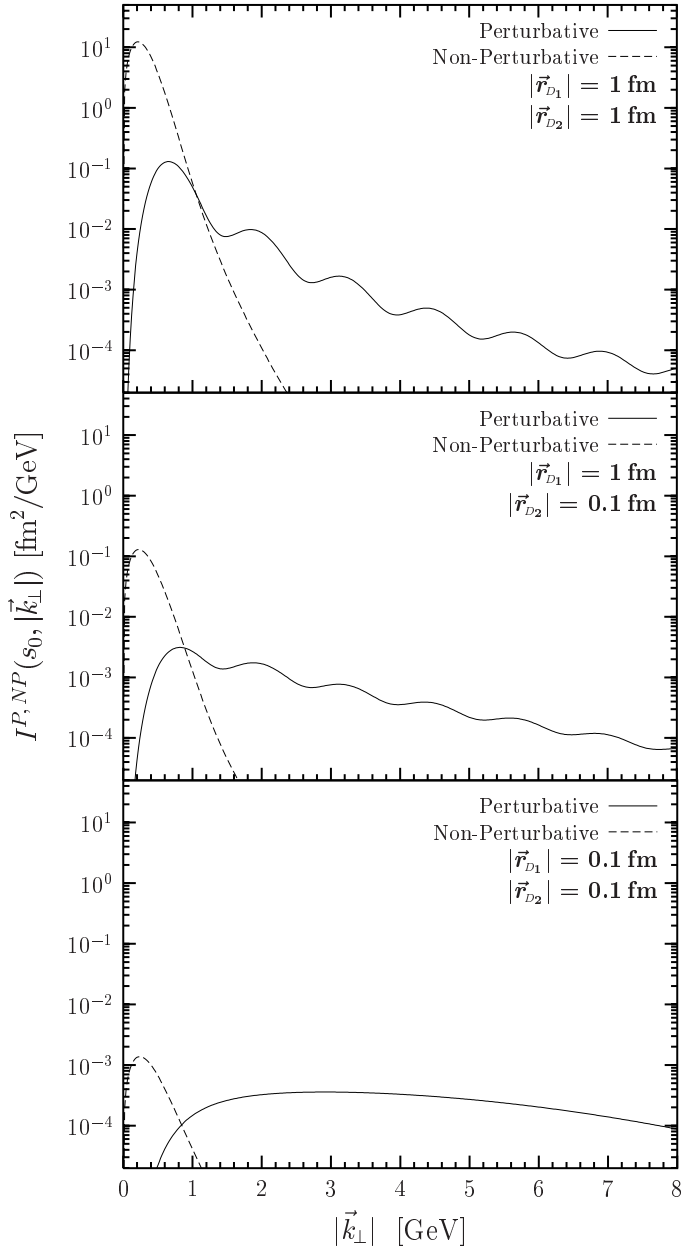


Figure 3.2: The perturbative integrand  $I^P$  (solid line) and the non-perturbative integrand  $I^{NP}$  (dashed line) of the total dipole-dipole cross section (3.1.10) as a function of transverse momentum  $|\vec{k}_\perp|$  for various dipole sizes  $|\vec{r}_{D_1}|$  and  $|\vec{r}_{D_2}|$ . The integrands are shown for the parameters given in Sec. 2.7 that allow a good description of the experimental data of hadron and photon reactions at  $\sqrt{s_0} \approx 20$  GeV with the wave functions given in Appendix B and the exact  $T$ -matrix element (2.6.2). The oscillations of the perturbative integrand  $I^P$  originate from the Bessel function  $J_0(|\vec{k}_\perp| |\vec{r}_{D_i}|)$ .

For  $t = 0$  the parameter  $z_{D_i}$  disappears upon the integration over  $z_i$  since only  $|\psi_{D_i}(z_i, \vec{r}_i)|^2$  given in Eq. (3.1.2) depends on  $z_i$ .

The structure presented for dipole-dipole scattering remains in reactions involving hadrons and photons: the hadronic and photonic total cross sections are obtained from the total dipole-dipole cross section (3.1.1) by replacing  $|\psi_{D_i}(z_i, \vec{r}_i)|^2$  given in Eq. (3.1.2) with the hadron and photon wave functions given in Appendix B. As the total dipole-dipole cross section, the total hadronic and photonic cross sections are independent of the parameters which control the  $z_i$ -distribution in the wave functions due to the normalization of the  $z_i$ -distributions. The independence of the total hadronic cross section on the widths  $\Delta z_h$  can be seen immediately with the Gaussian hadron wave functions (B.1.1)

$$\langle \psi_h | 1 - e^{i\vec{k}_\perp \cdot \vec{r}_i} | \psi_h \rangle = 1 - e^{-\frac{1}{2} k_\perp^2 S_h^2}, \quad (3.1.18)$$

$$\langle \psi_h | \tan^2 \phi_i (1 - e^{i\vec{k}_\perp \cdot \vec{r}_i}) | \psi_h \rangle = -1 + e^{-\frac{1}{2} k_\perp^2 S_h^2} + \sqrt{\frac{\pi}{2}} |\vec{k}_\perp| S_h \operatorname{Erf} \left( \frac{|\vec{k}_\perp| S_h}{\sqrt{2}} \right) \quad (3.1.19)$$

with the error function  $\operatorname{Erf}(z) = \sqrt{2/\pi} \int_0^z dt \exp(-t^2)$ . These analytical results confirm the  $\Delta z_h$  and  $z_D$ -independence of the total dipole-proton cross section assumed in phenomenological models [71–73]. However, the non-forward hadronic scattering amplitude  $T(s_0, t \neq 0)$  depends on the parameter  $\Delta z_h$  as shown explicitly in Appendix D. Thus, the differential elastic cross section  $d\sigma^{el}/dt(s, t)$  (5.4.1) and its logarithmic slope  $B(s, t)$  (5.3.1) are  $\Delta z_h$ -dependent. In fact, this  $\Delta z_h$ -dependence is essential for the agreement with experimental data [8] as discussed in chapter 5.

The  $|\vec{k}_\perp|$ -dependence of the perturbative and non-perturbative integrand for hadron-hadron, hadron-photon, and photon-photon cross sections at high photon virtualities is similar to the one of the perturbative and non-perturbative integrand of the dipole-dipole cross section shown in Fig. 3.2 for ( $|\vec{r}_{D_1}| = |\vec{r}_{D_2}| = 1$  fm), ( $|\vec{r}_{D_1}| = 1$  fm,  $|\vec{r}_{D_2}| = 0.1$  fm), and ( $|\vec{r}_{D_1}| = |\vec{r}_{D_2}| = 0.1$  fm), respectively. Of course, the absolute values differ and the oscillations of the perturbative integrand caused by the Bessel functions disappear.

## 3.2 Decomposition of the QCD String into Dipoles and Unintegrated Gluon Distributions

The *unintegrated gluon distribution* of hadrons<sup>3</sup>  $\mathcal{F}_h(x, k_\perp^2)$  is a basic, universal quantity convenient for the computation of many scattering observables at small  $x$ . It is the central object in the BFKL [40] and CCFM [41] evolution equations. Upon integration over the transverse gluon momentum  $|\vec{k}_\perp|$  it leads to the conventional gluon distribution  $xG_h(x, Q^2)$  used in the DGLAP evolution equation [42]. The unintegrated gluon distribution is crucial to describe processes in which transverse momenta are explicitly exposed such as dijet [38] or vector meson [39] production at HERA. Its explicit  $|\vec{k}_\perp|$  dependence is particularly suited to study the interplay between soft and hard physics. In this section an exact representation of the string as a collection of stringless quark-antiquark dipoles is presented that allows us to extract the perturbative and non-perturbative contributions to  $\mathcal{F}_h(x, k_\perp^2)$  from our total dipole-hadron cross section via  $|\vec{k}_\perp|$ -factorization.

We calculate the unintegrated gluon distribution  $\mathcal{F}_h(x, k_\perp^2)$  with the  $T$ -matrix element in the limit of small  $\chi$ -functions (2.6.3). Following Sec. 2.6, we give a strong energy dependence to the perturbative contribution  $\chi^P$  and a weak one to the non-perturbative contribution  $\chi^{NP}$ , see also Eqs. (2.6.4) and (2.6.5),

$$\begin{aligned} (\chi^P)^2 &\rightarrow (\chi^P)^2 \left(\frac{x_0}{x}\right)^{\epsilon^P} \\ (\chi^{NP})^2 &\rightarrow (\chi^{NP})^2 \left(\frac{x_0}{x}\right)^{\epsilon^{NP}} \end{aligned} \quad (3.2.1)$$

where the values of the exponents  $\epsilon^P$  and  $\epsilon^{NP}$  are given in Sec. 2.7 and  $x_0 = 2.4 \times 10^{-3}$  is adjusted to reproduce at  $Q^2 = 1 \text{ GeV}^2$  the integrated gluon distribution of the proton  $xG_p(x, Q^2)$  extracted from the HERA data [79]. The small- $\chi$  limit (2.6.3) considered here is applicable only for  $x = Q^2/s \geq 10^{-4}$ . For  $x \leq 10^{-4}$ , the full  $T$ -matrix element (2.6.2) has to be used which satisfies the  $S$ -matrix unitarity and leads to a successful description of many reactions as shown in chapter 4 and 5. The structure of the interactions worked out in this section, however, is independent of the phenomenological energy dependence considered.

The total dipole-hadron cross section  $\sigma_{Dh}(x, |\vec{r}_D|)$  is obtained from the total dipole-dipole cross section (3.1.1) by replacing  $|\psi_{D_2}(z_2, \vec{r}_2)|^2$  with a squared hadron wave function  $|\psi_h(z_2, \vec{r}_2)|^2$ . Accordingly, the  $x$ -dependent total dipole-hadron cross

---

<sup>3</sup>The word hadron and the subscript  $h$  is used genuinely for hadrons and photons in this section.

section reads

$$\begin{aligned} \sigma_{Dh}(x, |\vec{r}_D|) &= \frac{8}{9} \frac{1}{4\pi} \int dk_\perp^2 \quad (3.2.2) \\ &\times \left[ (4\pi\alpha_s(k_\perp^2))^2 \left\{ \left[ i\tilde{D}'^{(2)}(k_\perp^2) \right]^2 \left( 1 - J_0(|\vec{k}_\perp||\vec{r}_D|) \right) \langle \psi_h | 1 - e^{i\vec{k}_\perp \cdot \vec{r}_2} | \psi_h \rangle \right\} \left( \frac{x_0}{x} \right)^{\epsilon^P} \right. \\ &+ \left( \frac{\pi^2 G_2}{24} \right)^2 \left\{ \left[ \frac{\kappa}{k_\perp^2} i\tilde{D}^{(2)}(k_\perp^2) + (1 - \kappa) i\tilde{D}'^{(2)}(k_\perp^2) \right]^2 \left( 1 - J_0(|\vec{k}_\perp||\vec{r}_D|) \right) \langle \psi_h | 1 - e^{i\vec{k}_\perp \cdot \vec{r}_2} | \psi_h \rangle \right. \\ &\left. \left. + \left[ \frac{\kappa}{k_\perp^2} i\tilde{D}^{(2)}(k_\perp^2) \right]^2 \left( -1 + {}_1F_2\left(-\frac{1}{2}; \frac{1}{2}, 1; \frac{-k_\perp^2 r_D^2}{4}\right) \right) \langle \psi_h | \tan^2 \phi_2 (1 - e^{i\vec{k}_\perp \cdot \vec{r}_2}) | \psi_h \rangle \right\} \left( \frac{x_0}{x} \right)^{\epsilon^{NP}} \right] \end{aligned}$$

with the Bessel function  $J_0(|\vec{k}_\perp||\vec{r}_D|)$  and the generalized hypergeometric function  ${}_1F_2(-1/2; 1/2, 1; -k_\perp^2 r_D^2/4)$  derived in the previous section.

For dipole sizes  $|\vec{r}_D| \rightarrow 0$ , the perturbative contribution to  $\sigma_{Dh}(x, |\vec{r}_D|)$  is known to vanish quadratically with decreasing dipole size,  $\sigma_{Dh}(x, |\vec{r}_D|) \propto r_D^2$ . This behavior reflects the weak absorption of a small color-singlet dipole in the hadron and is known as *color transparency*. It can be seen immediately from Eq. (3.2.2) as

$$\left( 1 - J_0(|\vec{k}_\perp||\vec{r}_D|) \right) \approx \frac{k_\perp^2 r_D^2}{4} \quad \text{for } |\vec{r}_D| \rightarrow 0 \text{ and finite } |\vec{k}_\perp|. \quad (3.2.3)$$

The non-perturbative contribution to  $\sigma_{Dh}(x, |\vec{r}_D|)$  gives color transparency as well since the generalized hypergeometric function behaves as

$$\left( -1 + {}_1F_2\left(-\frac{1}{2}; \frac{1}{2}, 1; \frac{-k_\perp^2 r_D^2}{4}\right) \right) \approx \frac{k_\perp^2 r_D^2}{4} \quad \text{for } |\vec{r}_D| \rightarrow 0 \text{ and finite } |\vec{k}_\perp|. \quad (3.2.4)$$

For large dipole sizes,  $|\vec{r}_D| \gtrsim 1 \text{ fm}$ , the perturbative contribution to  $\sigma_{Dh}(x, |\vec{r}_D|)$  describing interactions of the quark and antiquark of the dipole with the hadron saturates since

$$\left( 1 - J_0(|\vec{k}_\perp||\vec{r}_D|) \right) \approx 1 \quad \text{for large } |\vec{k}_\perp||\vec{r}_D|. \quad (3.2.5)$$

In contrast, the non-perturbative contribution to  $\sigma_{Dh}(x, |\vec{r}_D|)$  increases linearly with increasing dipole size,  $\sigma_{Dh}(x, |\vec{r}_D|) \propto |\vec{r}_D|$ . This linear increase is generated by the interaction of the string of the dipole with the hadron: The string elongates linearly with the dipole size  $|\vec{r}_D|$  and, thus, has a linearly increasing geometric cross section with the hadron. Indeed, this feature of the string can be seen analytically since

$$\left( -1 + {}_1F_2\left(-\frac{1}{2}; \frac{1}{2}, 1; \frac{-k_\perp^2 r_D^2}{4}\right) \right) \propto |\vec{k}_\perp||\vec{r}_D| \quad \text{for large } |\vec{k}_\perp||\vec{r}_D|. \quad (3.2.6)$$

When considered in Euclidean space-time, the same string gives also the linear confining potential between a static quark and antiquark at large  $q\bar{q}$  separations [17, 31] as shown briefly at the end of Sec. 2.4. Thus, the behavior of the total dipole-hadron cross section is related to the confining potential. Furthermore, as we are working in the quenched approximation, there is no string breaking through dynamical quark-antiquark production at large dipole sizes. String breaking is expected to stop the linear increase of the total dipole-hadron cross section at dipole sizes of  $|\vec{r}_D| \gtrsim 1$  fm analogous to the saturation of the static  $q\bar{q}$  potential seen for large  $q\bar{q}$  separations on the lattice in full QCD [26, 80].

In Fig. 3.3 we show the perturbative (solid line) and non-perturbative (dashed line) contributions to the total dipole-proton cross section  $\sigma_{Dp}(x, |\vec{r}_D|)$  as a function of the dipole size  $|\vec{r}_D|$  at  $x = x_0 = 2.4 \cdot 10^{-3}$ , where the perturbative contribution is multiplied by a factor of 10. The dipole-proton cross section is computed with the

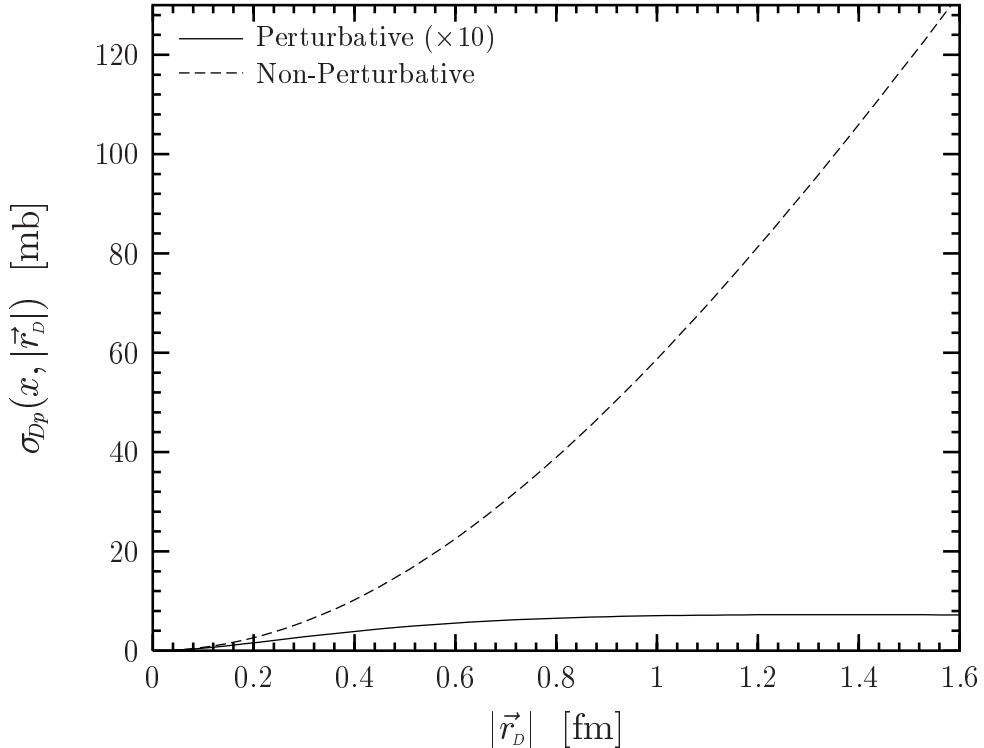


Figure 3.3: Perturbative (solid line) and non-perturbative (dashed line) contributions to the total dipole-proton cross section  $\sigma_{Dp}(x, |\vec{r}_D|)$  as a function of the dipole size  $|\vec{r}_D|$  at  $x = x_0 = 2.4 \cdot 10^{-3}$ , with the perturbative contribution multiplied by a factor of 10. The perturbative contribution shows color transparency at small  $|\vec{r}_D|$  and saturates at large  $|\vec{r}_D|$ . The non-perturbative contribution shows also color transparency at small  $|\vec{r}_D|$  but increases linearly with increasing  $|\vec{r}_D|$ .

simple Gaussian proton wave function (B.1.1) and illustrates the general features discussed above: The perturbative contribution shows color transparency at small  $|\vec{r}_D|$  and saturates at large  $|\vec{r}_D|$ . The non-perturbative contribution shows also color transparency at small  $|\vec{r}_D|$  but increases linearly with increasing  $|\vec{r}_D|$ .

Our result (3.2.2) shows that the  $|\vec{k}_\perp|$ -dependence of the hadron constituents factorizes from the rest of the process in both the perturbative and the non-perturbative contribution to the total dipole-hadron cross section. This factorization – known in perturbative QCD as  $|\vec{k}_\perp|$ -factorization [81] – allows to define the unintegrated gluon distribution  $\mathcal{F}_h(x, k_\perp^2)$  as follows [69, 72, 82]

$$\sigma_{Dh}(x, |\vec{r}_D|) = \frac{4\pi^2 r_D^2}{3} \int dk_\perp^2 \frac{\left(1 - J_0(|\vec{k}_\perp| |\vec{r}_D|)\right)}{(|\vec{k}_\perp| |\vec{r}_D|)^2} \alpha_s(k_\perp^2) \mathcal{F}_h(x, k_\perp^2) . \quad (3.2.7)$$

For small dipole sizes  $|\vec{r}_D|$ , this equation together with (3.2.3) and the integrated gluon distribution

$$xG_h(x, Q^2) = \int_0^{Q^2} dk_\perp^2 \mathcal{F}_h(x, k_\perp^2) \quad (3.2.8)$$

leads to the widely used perturbative QCD relation [83]

$$\sigma_{Dh}(x, |\vec{r}_D|) = \frac{\pi^2 r_D^2}{3} \left[ \alpha_s(Q^2) xG_h(x, Q^2) \right]_{Q^2=c/r_D^2} , \quad (3.2.9)$$

where  $c \approx 10$  is estimated from the properties of the Bessel function  $J_0(|\vec{k}_\perp| |\vec{r}_D|)$  [84].

To extract the unintegrated gluon distribution  $\mathcal{F}_h(x, k_\perp^2)$ , we compare (3.2.7) with (3.2.2) using the following mathematical identity

$$\left( -1 + {}_1F_2\left(-\frac{1}{2}; \frac{1}{2}, 1; \frac{-k_\perp^2 r_D^2}{4}\right) \right) = \int_0^1 d\xi \frac{1}{\xi^2} \left( 1 - J_0(|\vec{k}_\perp| |\vec{r}_D| \xi) \right) . \quad (3.2.10)$$

As discussed in the previous section, the lhs of (3.2.10) results from the string averaged over all orientations (3.1.16). Thus, the string confining the quark-antiquark dipole of length  $|\vec{r}_D|$  can be represented as an integral over stringless dipoles of sizes  $\xi |\vec{r}_D|$  with  $0 \leq \xi \leq 1$  and a dipole number density of  $n(\xi) = 1/\xi^2$ . As visualized in Fig. 3.4, the string-hadron scattering process reduces to an incoherent superposition of stringless dipole-hadron scattering processes with dipole sizes  $0 \leq \xi |\vec{r}_D| \leq |\vec{r}_D|$  and dipole number density  $n(\xi) = 1/\xi^2$ . The decomposition of the string into many smaller stringless dipoles via (3.2.10) behaves similar to the wave function of a  $q\bar{q}$  onium state in the large  $N_c$  limit [36, 37]: The numerous gluons emitted inside the onium state can be considered as many  $q\bar{q}$  dipoles in the large  $N_c$  limit.

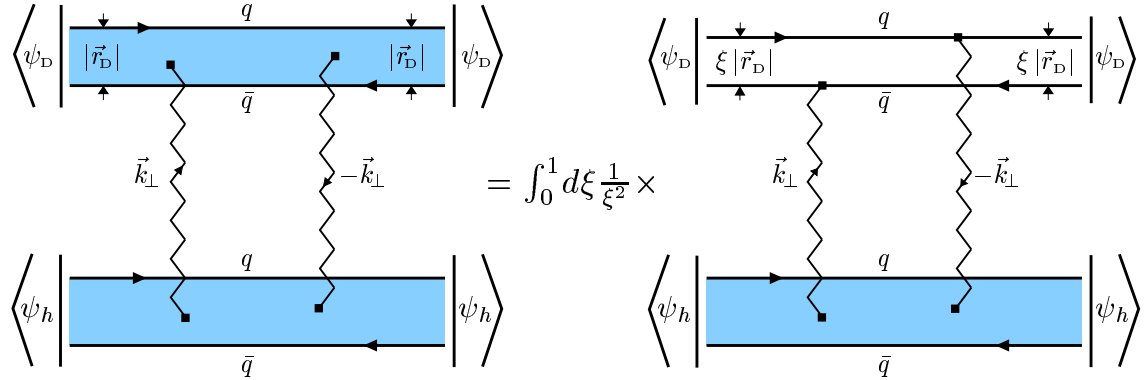


Figure 3.4: The string of length  $|\vec{r}_D|$  is made up of stringless dipoles of size  $\xi|\vec{r}_D|$  with  $0 \leq \xi \leq 1$  and dipole number density  $n(\xi) = 1/\xi^2$ . The string-hadron scattering process reduces to an incoherent superposition of stringless dipole-hadron scattering processes.

Inserting (3.2.10) into (3.2.2) and rescaling the momentum variable  $|\vec{k}'_\perp| = \xi|\vec{k}_\perp|$ , the string-hadron (*sh*) contribution to the total dipole-hadron cross section (3.2.2) becomes

$$\begin{aligned} \sigma_{Dh}^{sh}(x, |\vec{r}_D|) &= \frac{8}{9} \frac{1}{4\pi} \int dk'^2_\perp \left( 1 - J_0(|\vec{k}'_\perp| |\vec{r}_D|) \right) \quad (3.2.11) \\ &\times \left( \frac{\pi^2 G_2}{24} \right)^2 \left\{ \frac{\kappa^2}{k'^4_\perp} \int_0^1 d\xi \left[ i\tilde{D}^{(2)}\left(\frac{k'^2_\perp}{\xi^2}\right) \right]^2 \langle \psi_h | \tan^2 \phi_2 (1 - e^{i(\vec{k}'_\perp/\xi)\vec{r}_2}) | \psi_h \rangle \right\} \left( \frac{x_0}{x} \right)^{\epsilon^{NP}}. \end{aligned}$$

The dipole factor  $(1 - J_0(|\vec{k}'_\perp| |\vec{r}_D|))$  indicates that the string-hadron interaction has been rewritten into a stringless dipole-hadron interaction. The string confining the dipole has been shifted into the hadron. Comparing (3.2.7) with our new expression for the total dipole-hadron cross section,

$$\begin{aligned} \sigma_{Dh}(x, |\vec{r}_D|) &= \frac{8}{9} \frac{1}{4\pi} \int dk^2_\perp \left( 1 - J_0(|\vec{k}_\perp| |\vec{r}_D|) \right) \\ &\times \left[ (4\pi\alpha_s(k^2_\perp))^2 \left\{ \left[ i\tilde{D}'^{(2)}(k^2_\perp) \right]^2 \langle \psi_h | 1 - e^{i\vec{k}_\perp \vec{r}_2} | \psi_h \rangle \right\} \left( \frac{x_0}{x} \right)^{\epsilon^P} \right. \\ &+ \left( \frac{\pi^2 G_2}{24} \right)^2 \left\{ \left[ (1 - \kappa) \left[ i\tilde{D}'^{(2)}(k^2_\perp) \right] + \frac{\kappa}{k^2_\perp} \left[ i\tilde{D}^{(2)}(k^2_\perp) \right] \right]^2 \langle \psi_h | 1 - e^{i\vec{k}_\perp \vec{r}_2} | \psi_h \rangle \right. \\ &\left. \left. + \frac{\kappa^2}{k^4_\perp} \int_0^1 d\xi \left[ i\tilde{D}^{(2)}\left(\frac{k^2_\perp}{\xi^2}\right) \right]^2 \langle \psi_h | \tan^2 \phi_2 (1 - e^{i(\vec{k}_\perp/\xi)\vec{r}_2}) | \psi_h \rangle \right\} \left( \frac{x_0}{x} \right)^{\epsilon^{NP}} \right], \quad (3.2.12) \end{aligned}$$

one obtains the unintegrated gluon distribution

$$\begin{aligned}
\mathcal{F}_h(x, k_\perp^2) &= \frac{k_\perp^2}{6\pi^3 \alpha_s(k_\perp^2)} \\
&\times \left[ (4\pi\alpha_s(k_\perp^2))^2 \left\{ \left[ i\tilde{D}_P^{(2)}(k_\perp^2) \right]^2 \langle \psi_h | 1 - e^{i\vec{k}_\perp \vec{r}_2} | \psi_h \rangle \right\} \left( \frac{x_0}{x} \right)^{\epsilon^P} \right. \\
&+ \left( \frac{\pi^2 G_2}{24} \right)^2 \left\{ \left[ (1 - \kappa) \left[ i\tilde{D}_1^{(2)}(k_\perp^2) \right] + \frac{\kappa}{k_\perp^2} \left[ i\tilde{D}^{(2)}(k_\perp^2) \right] \right]^2 \langle \psi_h | 1 - e^{i\vec{k}_\perp \vec{r}_2} | \psi_h \rangle \right. \\
&\left. \left. + \frac{\kappa^2}{k_\perp^4} \int_0^1 d\xi \left[ i\tilde{D}^{(2)}\left(\frac{k_\perp^2}{\xi^2}\right) \right]^2 \langle \psi_h | \tan^2 \phi_2 (1 - e^{i(\vec{k}_\perp/\xi)\vec{r}_2}) | \psi_h \rangle \right\} \left( \frac{x_0}{x} \right)^{\epsilon^{NP}} \right]. \quad (3.2.13)
\end{aligned}$$

This result shows explicitly the microscopic structure of the perturbative and non-perturbative contribution to  $\mathcal{F}_h(x, k_\perp^2)$ . It is valid for any hadron wave function. To get numerical values for the unintegrated gluon distribution  $\mathcal{F}_h(x, k_\perp^2)$ , the hadron wave functions must be specified.

### 3.3 Numerical Results for Unintegrated Gluon Distributions in Hadrons and Photons

In this section we present the unintegrated gluon distribution (3.2.13) for protons, pions, kaons, and photons computed with the Gaussian hadron wave function (B.1.1) and the perturbatively derived photon wave functions (B.2.1) and (B.2.2). To account for non-perturbative effects at low photon virtuality  $Q^2$  in the photon wave functions, quark masses  $m_f(Q^2)$  are used that interpolate between the current quarks at large  $Q^2$  and the constituent quarks at small  $Q^2$  [20] as discussed in Appendix B.

The unintegrated gluon distribution of the proton  $\mathcal{F}_p(x, k_\perp^2)$  is shown as a function of transverse momentum  $|\vec{k}_\perp|$  at  $x = 10^{-1}, 10^{-2}, 10^{-3}$ , and  $10^{-4}$  in Fig. 3.5. Figure 3.6 illustrates the interplay of the perturbative (solid line) and non-perturbative (dashed line) contributions to  $|\vec{k}_\perp| \mathcal{F}_p(x, k_\perp^2)$  as a function of transverse momentum  $|\vec{k}_\perp|$  for the same values of  $x$ . At small momenta  $|\vec{k}_\perp|$ , the unintegrated gluon distribution is dominated by the non-perturbative contribution and behaves as  $1/|\vec{k}_\perp|$ . This behavior is a string manifestation as it reflects the linear increase of the total dipole-proton cross section at large dipole sizes. In contrast, the saturation model of Golec-Biernat and Wüsthoff [72] shows the behavior  $\mathcal{F}_p^{GBW}(x, k_\perp^2) \propto k_\perp^2$  for small momenta. With increasing  $|\vec{k}_\perp|$ , the non-perturbative contribution to  $\mathcal{F}_p(x, k_\perp^2)$  decreases rapidly which results from the strong suppression of large momenta by

the non-perturbative correlation functions  $i\tilde{D}'^{(2)}(k_\perp^2)$  and  $i\tilde{D}^{(2)}(k_\perp^2)$  given in (3.1.7) and (3.1.8). For  $|\vec{k}_\perp| \gtrsim 1 \text{ GeV}$ , the perturbative contribution dominates the unintegrated gluon distribution. It drops as  $1/k_\perp^2$  in accordance with the perturbative correlation function  $i\tilde{D}'^{(2)}(k_\perp^2)$  given in (3.1.6). This perturbative QCD result is not reproduced by the phenomenological model of Golec-Biernat and Wüsthoff [72] which predicts a Gaussian decrease of  $\mathcal{F}_p(x, k_\perp^2)$  with increasing  $|\vec{k}_\perp|$ .

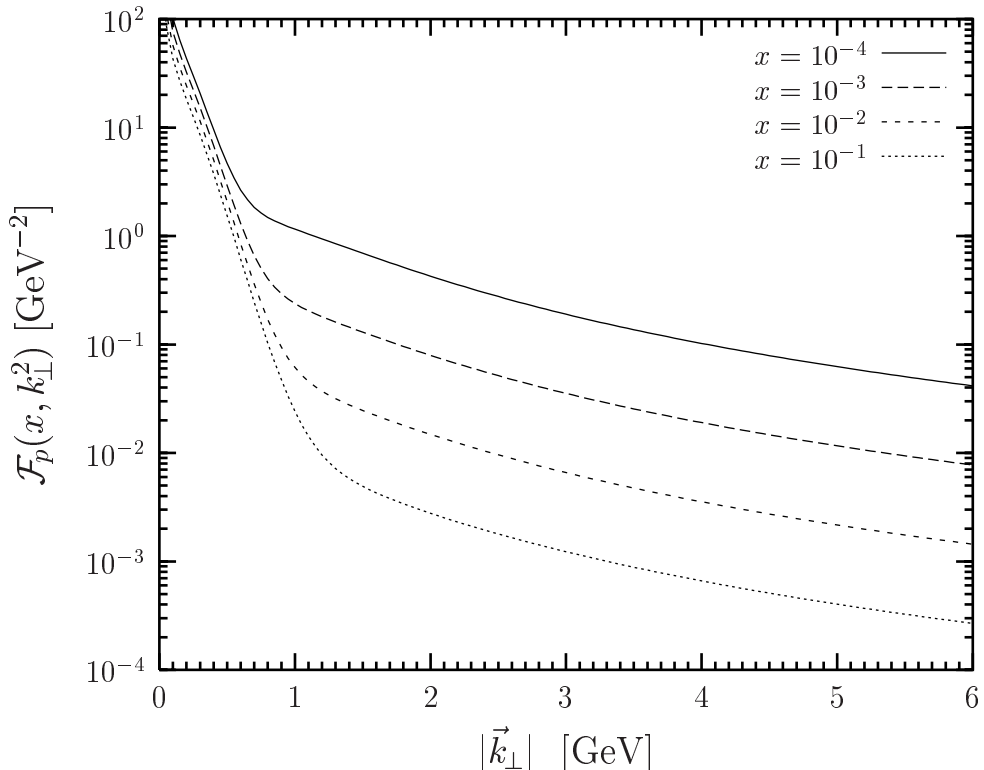


Figure 3.5: The unintegrated gluon distribution of the proton  $\mathcal{F}_p(x, k_\perp^2)$  as a function of transverse momentum  $|\vec{k}_\perp|$  at Bjorken- $x$  values of  $10^{-1}$ ,  $10^{-2}$ ,  $10^{-3}$  and  $10^{-4}$ .

The  $x$ -dependence of  $\mathcal{F}_p(x, k_\perp^2)$  can be seen in Figs. 3.5 and 3.6: With decreasing  $x$ , the perturbative contribution increases much stronger than the non-perturbative contribution which results from the energy exponents  $\epsilon^P \gg \epsilon^{NP}$  in (3.2.1) necessary to describe the experimental data within our model as discussed in Sec. 2.6. Moreover, the perturbative contribution extends into the small- $|\vec{k}_\perp|$  region as  $x$  decreases. Indeed, the soft-hard transition point moves towards smaller momenta with decreasing  $x$  as shown in Fig. 3.6. Such a hard-to-soft diffusion is observed also in [85] where the unintegrated gluon distribution has been parametrized to reproduce the experimental data for the proton structure function  $F_2(x, Q^2)$  at small  $x$ .

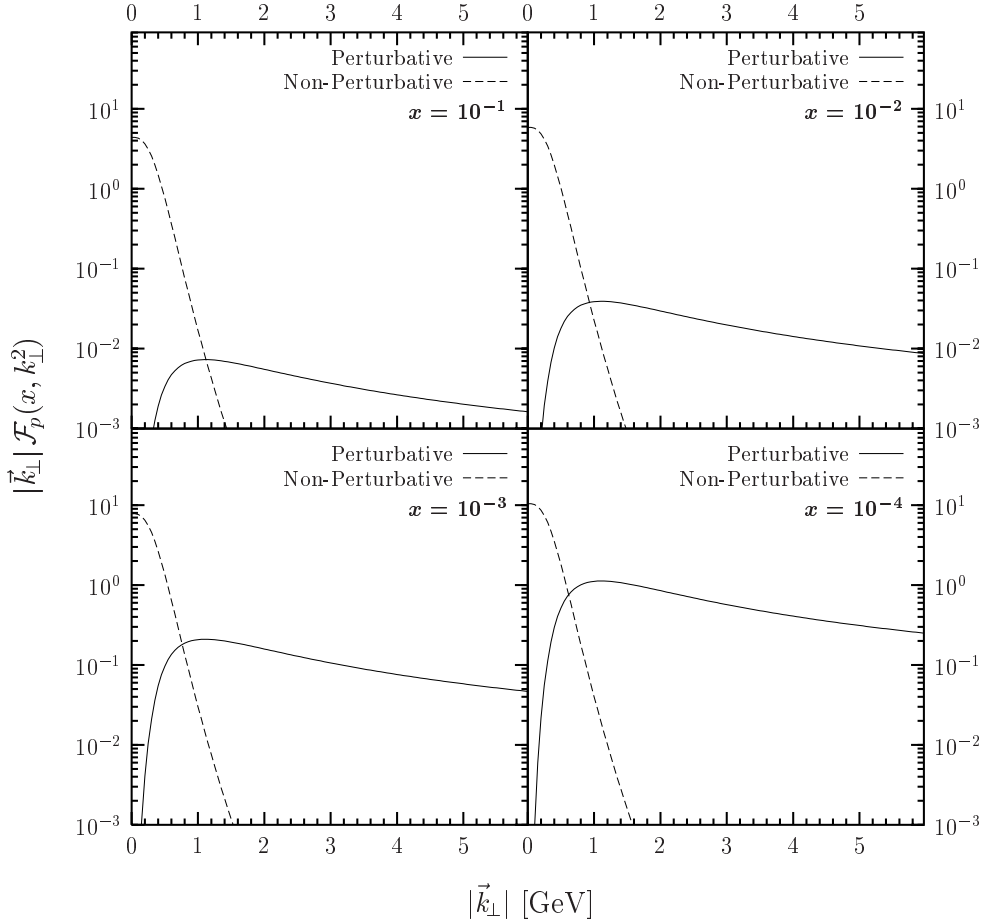


Figure 3.6: The unintegrated gluon distribution of the proton  $\mathcal{F}_p(x, k_\perp^2)$  times the transverse momentum  $|\vec{k}_\perp|$  as a function of  $|\vec{k}_\perp|$  at Bjorken- $x$  values of  $10^{-1}$ ,  $10^{-2}$ ,  $10^{-3}$  and  $10^{-4}$ .

The opposite behavior is obtained in the approach of the color glass condensate [86]: With decreasing  $x$ , gluons are produced predominantly in the high-  $|\vec{k}_\perp|$  region of lower density and weaker repulsive interactions.

In Fig. 3.7, the unintegrated gluon distribution of the proton, pion, and kaon  $\mathcal{F}_h(x, k_\perp^2)$  times the transverse momentum  $|\vec{k}_\perp|$  is shown as a function of  $|\vec{k}_\perp|$  at  $x = 10^{-3}$ . The hadrons are characterized by different values for  $\Delta z_h$  and  $S_h$  in the hadron wave function (B.1.1). However,  $\mathcal{F}_h(x, k_\perp^2)$  depends only on  $S_h$ . Due to the normalization of the hadron wave functions,  $\Delta z_h$  disappears upon the integration over  $z_i$  as can be seen directly from (3.1.18) and (3.1.19). At small momenta,  $\mathcal{F}_h(x, k_\perp^2) \propto S_h^2$  is found from (3.1.18), (3.1.19), and (3.2.13). It becomes visible

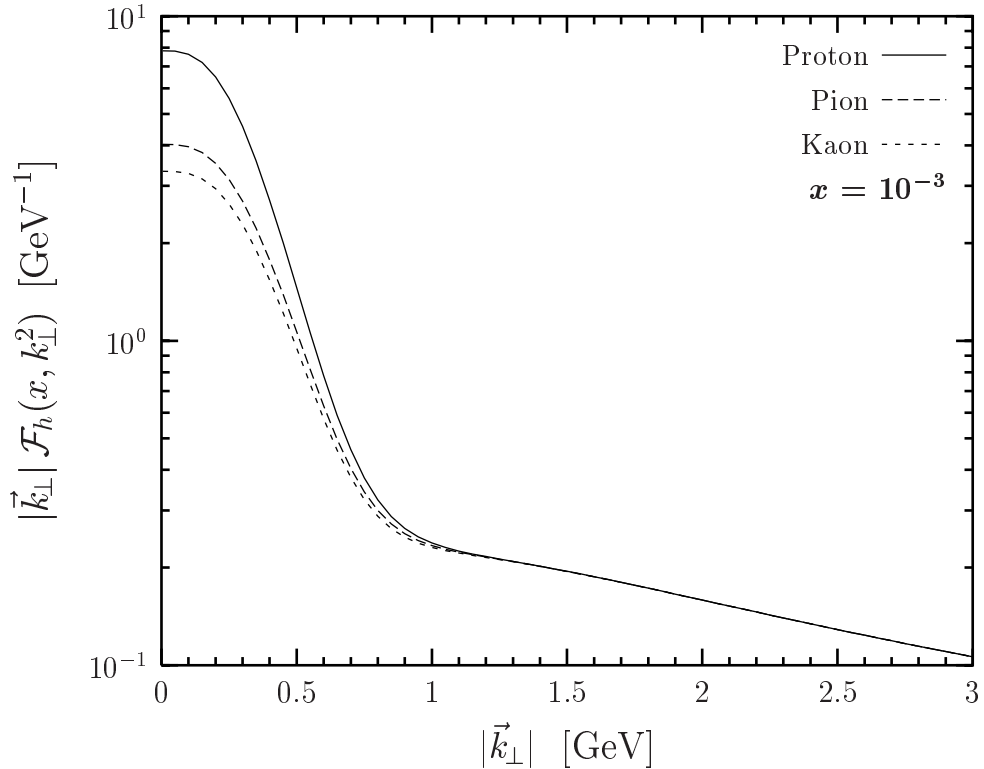


Figure 3.7: The unintegrated gluon distribution of the proton, pion, and kaon  $\mathcal{F}_h(x, k_\perp^2)$  times the transverse momentum  $|\vec{k}_\perp|$  as a function of  $|\vec{k}_\perp|$  at Bjorken-variable  $x = 10^{-3}$ .

in Fig. 3.7 for the chosen hadron extensions:  $S_p = 0.86$  fm,  $S_\pi = 0.607$  fm, and  $S_K = 0.55$  fm. At large momenta where the perturbative contribution dominates, the dependence on  $S_h$  vanishes as can be seen from (3.1.18) and the unintegrated gluon distributions of protons, pions, and kaons become identical. Of course, this behavior results from the wave function normalization being identical for protons, pions, and kaons with two valence constituents which are the quark and antiquark in the pion and kaon and the quark and diquark in the proton. At large  $|\vec{k}_\perp|$ , i.e., high resolution, the realistic description of protons as three-quark systems becomes necessary. In fact, the three-quark description of protons leads to a different perturbative contribution in (3.2.13): the quark counting factors of 2 (appropriate for mesons) in the square brackets in (3.1.11) are substituted by factors of 3 (appropriate for baryons) [34, 35]. At other values of  $x$ , the unintegrated gluon distributions of protons, pions and kaons show the same features.

Photons are particularly interesting because the transverse size of the quark-antiquark dipole into which a photon fluctuates is controlled by the photon virtual-

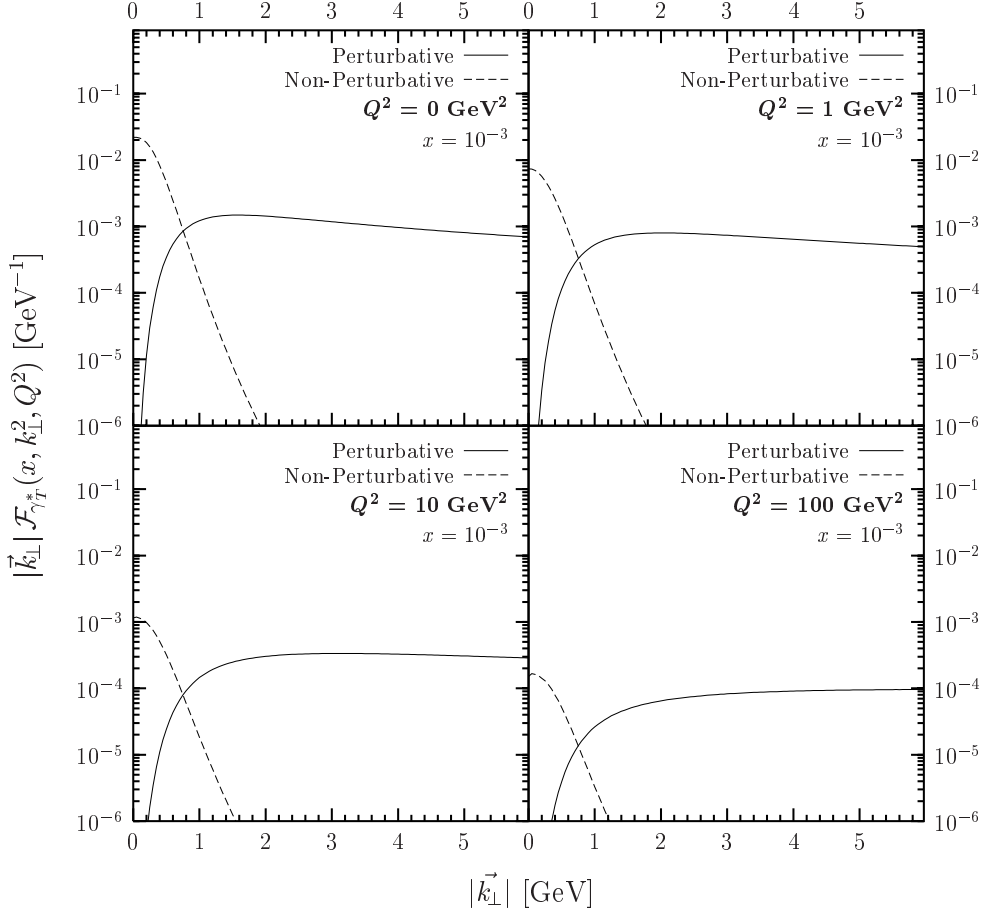


Figure 3.8: The unintegrated gluon distribution of the transverse polarized photon  $\mathcal{F}_{\gamma_T^*}(x, k_{\perp}^2, Q^2)$  times the transverse momentum  $|\vec{k}_{\perp}|$  as a function of  $|\vec{k}_{\perp}|$  at photon virtualities of  $Q^2 = 0, 1, 10$ , and  $100 \text{ GeV}^2$  and Bjorken-variable  $x = 10^{-3}$ .

ity  $Q^2$  (cf. Appendix B)

$$|\vec{r}_{\gamma_{T,L}^*}| \approx \frac{2}{Q^2 + 4m_u^2(Q^2)} , \quad (3.3.1)$$

where  $m_u(Q^2)$  is the running  $u$ -quark mass given in Appendix B. In Figs. 3.8 and 3.9, the unintegrated gluon distribution of transverse ( $T$ ) and longitudinal ( $L$ ) photons  $\mathcal{F}_{\gamma_{T,L}^*}(x, k_{\perp}^2, Q^2)$  times the transverse momentum  $|\vec{k}_{\perp}|$  is shown as a function of  $|\vec{k}_{\perp}|$  for various photon virtualities  $Q^2$  at  $x = 10^{-3}$ . With increasing  $Q^2$ , i.e., decreasing “photon size”  $|\vec{r}_{\gamma_{T,L}^*}|$ , the ratio of the perturbative to the non-perturbative contribution to  $\mathcal{F}_{\gamma_{T,L}^*}(x, k_{\perp}^2, Q^2)$  increases. This behavior has already been discussed in Sec. 3.1 on the level of dipole-dipole scattering, where decreasing dipole sizes increase the ratio of the perturbative to non-perturbative contribution, see Fig. 3.1.

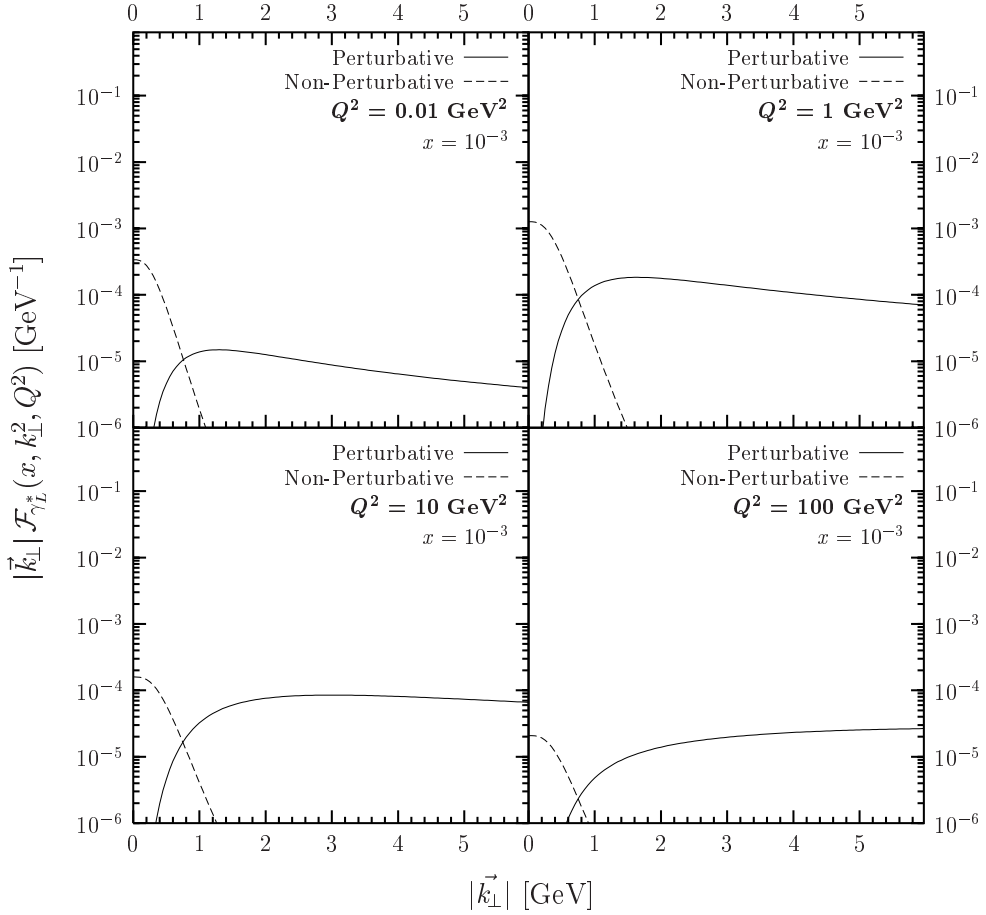


Figure 3.9: The unintegrated gluon distribution of the longitudinally polarized photon  $\mathcal{F}_{\gamma_L^*}(x, k_\perp^2, Q^2)$  times the transverse momentum  $|\vec{k}_\perp|$  as a function of  $|\vec{k}_\perp|$  at photon virtualities of  $Q^2 = 0.01, 1, 10$ , and  $100 \text{ GeV}^2$  and Bjorken-variable  $x = 10^{-3}$ .

Due to the different  $Q^2$ -dependence in the transverse and longitudinally polarized photon wave functions,  $\mathcal{F}_{\gamma_T^*}(x, k_\perp^2, Q^2)$  decreases continuously with increasing  $Q^2$  while  $\mathcal{F}_{\gamma_L^*}(x, k_\perp^2, Q^2)$  increases for  $Q^2 \lesssim 1 \text{ GeV}^2$  and decreases for  $Q^2 \gtrsim 1 \text{ GeV}^2$ .

In Fig. 3.10, the unintegrated gluon distributions of hadrons and photons discussed above are compared. The unintegrated gluon distribution of real ( $Q^2 = 0$ ) photons ( $|\vec{r}_{\gamma_T}| \approx S_h$ ) is suppressed by a factor of order  $\alpha$  in comparison to the one of the hadrons otherwise its shape is very similar. The suppression factor comes from the photon-dipole transition described by the photon wave functions given in Appendix B. The ratio of the perturbative to the non-perturbative contribution of unintegrated gluon distributions increases as one goes from hadrons to photons

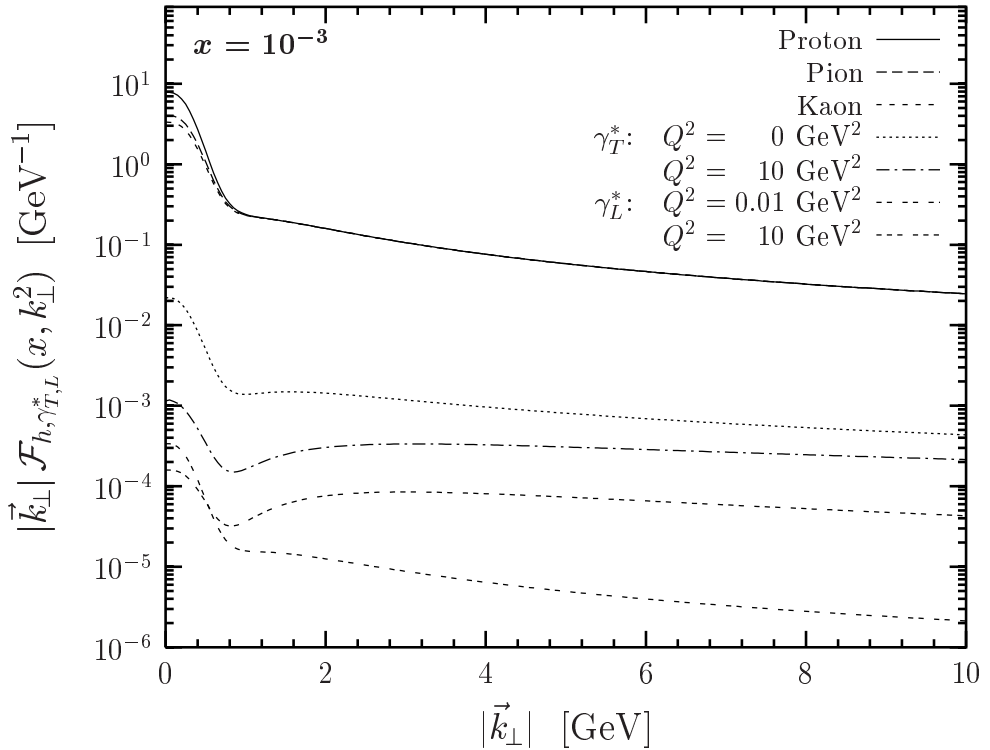


Figure 3.10: The unintegrated gluon distribution of the proton, pion, kaon, and transverse and longitudinally polarized photon  $\mathcal{F}_{h,\gamma_{T,L}^*}(x, k_\perp^2)$  times the transverse momentum  $|\vec{k}_\perp|$  as a function of  $|\vec{k}_\perp|$  at Bjorken-variable  $x = 10^{-3}$ . Results for transverse polarized photons are shown for photon virtualities of  $Q^2 = 0$  and  $10 \text{ GeV}^2$  and results for longitudinally polarized photons for photon virtualities of  $Q^2 = 0.01$  and  $10 \text{ GeV}^2$ .

with high virtuality  $Q^2$ . Since the wave functions of protons, pions, and kaons are normalized to the same value, the unintegrated gluon distributions of these hadrons are, as mentioned above, identical at large  $|\vec{k}_\perp|$  and do not depend on the hadron size. In contrast, the  $Q^2$ -dependence of the photon wave functions leads to  $Q^2$ -dependent, i.e., “photon size”-dependent, unintegrated gluon distributions at large  $|\vec{k}_\perp|$ . With increasing  $|\vec{k}_\perp|$ , the unintegrated gluon distributions of hadrons and photons become parallel in line with the vanishing dependence on the specific form of the wave function.

In Fig. 3.11, the integrated gluon distribution of the proton  $xG_p(x, Q^2)$  is shown as a function of Bjorken- $x$  at photon virtualities of  $Q^2 = 1, 5$ , and  $20 \text{ GeV}^2$ . Recall that the parameter  $x_0 = 2.4 \cdot 10^{-3}$  has been adjusted in the previous section such that the experimental data of  $xG_p(x, Q^2)$  at  $Q^2 = 1 \text{ GeV}^2$  [79] are reproduced. For  $x \gtrsim 10^{-3}$ ,  $xG_p(x, Q^2)$  is mainly determined by non-perturbative physics as can be

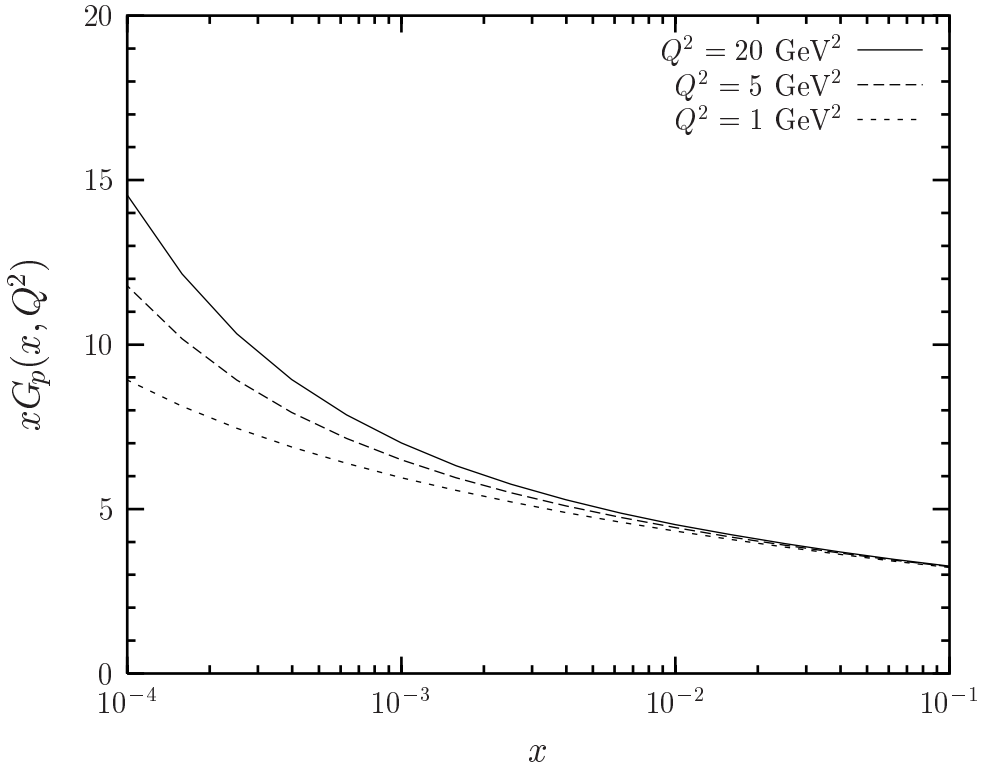


Figure 3.11: The gluon distribution of the proton  $xG_p(x, Q^2)$  as a function of Bjorken- $x$  at photon virtualities of  $Q^2 = 1, 5$ , and  $20 \text{ GeV}^2$ .

seen from Figs. 3.5 and 3.6. Perturbative physics becomes relevant for  $x \lesssim 10^{-3}$  and generates the steep increase of  $xG_p(x, Q^2)$  with decreasing  $x$  at fixed  $Q^2$ . Also the rise of  $xG_p(x, Q^2)$  with increasing  $Q^2$  at fixed  $x$  results from the perturbative contribution. For  $x \ll 10^{-4}$ , we show explicitly in Sec. 4.4 that multiple gluonic exchanges contained in the full  $T$ -matrix element (2.6.6) slow down the powerlike increase of  $xG_p(x, Q^2)$  with decreasing  $x$  in accordance with  $S$ -matrix unitarity constraints.

## 3.4 Comparison with Other Work

In this section, we compare the unintegrated gluon distribution of the proton extracted from our loop-loop correlation model (LLCM) with those obtained from the saturation model of Golec-Biernat and Wüsthoff (GBW) [72], the derivative of the Glück, Reya, and Vogt (GRV) parametrization of  $xG_p(x, Q^2)$  [87], and the approach of Ivanov and Nikolaev (IN) [85].

In the approach of Golec-Biernat and Wüsthoff [72], the unintegrated gluon distribution of the proton is extracted from the total dipole-proton cross section by inverting (3.2.7),

$$\mathcal{F}_p(x, k_\perp^2) = \frac{3 \sigma_0}{4 \pi^2 \alpha_s} R_0^2(x) k_\perp^2 \exp(-R_0^2(x) k_\perp^2) \quad \text{with} \quad R_0^2(x) = \frac{1}{Q_0^2} \left( \frac{x}{x_0} \right)^\lambda \quad (3.4.1)$$

where the parameter  $\sigma_0 = 29.12 \text{ mb}$ ,  $\alpha_s = 0.2$ ,  $Q_0 = 1 \text{ GeV}$ ,  $\lambda = 0.277$ , and  $x_0 = 0.41 \cdot 10^{-4}$  are obtained from a fit to the proton structure function  $F_2(x, Q^2)$  including charm quarks in the photon wave function. Note, however that the GBW approach uses the dipole-proton cross section of the GBW model on the lhs of (3.2.7) which implies multiple gluon exchanges while the rhs of (3.2.7) describes only two-gluon exchange as discussed in Sec. 3.1. Moreover, as demonstrated below, the large  $k_\perp^2$ -behavior of the unintegrated gluon distribution (3.4.1) deviates significantly from the DGLAP results. This mismatch motivated the recent modifications of the saturation model [88].

The unintegrated gluon distribution of the proton is also computed from the integrated gluon distribution  $xG_p(x, Q^2)$  by inverting (3.2.8)

$$\mathcal{F}_p(x, k_\perp^2) = \left. \frac{d x G_p(x, Q^2)}{d Q^2} \right|_{Q^2=k_\perp^2} . \quad (3.4.2)$$

Here, we use for the integrated gluon distribution  $xG_p(x, Q^2)$  the leading order (LO) parametrization of Glück, Reya, and Vogt (GRV) [87], which covers the kinematic region  $10^{-9} < x < 1$  and  $0.8 \text{ GeV}^2 < Q^2 < 10^6 \text{ GeV}^2$ .

Ivanov and Nikolaev [85] have constructed a two-component (soft + hard) ansatz for the unintegrated gluon distribution of the proton

$$\mathcal{F}_p(x, k_\perp^2) = \mathcal{F}_{\text{soft}}(x, k_\perp^2) \frac{k_s^2}{k_\perp^2 + k_s^2} + \mathcal{F}_{\text{hard}}(x, k_\perp^2) \frac{k_\perp^2}{k_\perp^2 + k_h^2} \quad (3.4.3)$$

with the soft and hard component

$$\mathcal{F}_{\text{soft}}(k_{\perp}^2) = a_{\text{soft}} C_F N_c \frac{\alpha_s(k_{\perp}^2)}{\pi} \frac{k_{\perp}^2}{(k_{\perp}^2 + \mu_{\text{soft}}^2)^2} \left[ 1 - \left( 1 + \frac{3 k_{\perp}^2}{\Lambda^2} \right)^{-2} \right] \quad (3.4.4)$$

$$\mathcal{F}_{\text{hard}}(x, k_{\perp}^2) = \mathcal{F}_{\text{pt}}^{(B)}(k_{\perp}^2) \frac{\mathcal{F}_{\text{pt}}(x, Q_c^2)}{\mathcal{F}_{\text{pt}}^{(B)}(Q_c^2)} \Theta(Q_c^2 - k_{\perp}^2) + \mathcal{F}_{\text{pt}}(x, k_{\perp}^2) \Theta(k_{\perp}^2 - Q_c^2) \quad (3.4.5)$$

where  $\mathcal{F}_{\text{pt}}^{(B)}(k_{\perp}^2)$  has the same form as (3.4.4) with the parameters  $a_{\text{pt}}$  and  $\mu_{\text{pt}}$  instead of  $a_{\text{soft}}$  and  $\mu_{\text{soft}}$  and  $\mathcal{F}_{\text{pt}}(x, k_{\perp}^2)$  is the derivative of the integrated gluon distribution (3.4.2). In the IN approach, the running coupling is given by  $\alpha_s(k_{\perp}^2) = \min\{0.82, (4\pi)/(\beta_0 \log[k_{\perp}^2/\Lambda_{QCD}^2])\}$ . With the GRV-parametrization [87] for the integrated gluon distribution, the structure function of the proton  $F_2(x, Q^2)$  has been described successfully using the following parameters:  $k_s^2 = 3 \text{ GeV}^2$ ,  $k_h^2 = (1 + 0.0018 \log(1/x)^4)^{0.5}$ ,  $a_{\text{soft}} = 2$ ,  $a_{\text{pt}} = 1$ ,  $\mu_{\text{soft}} = 0.1 \text{ GeV}$ ,  $\mu_{\text{pt}} = 0.75 \text{ GeV}$ ,  $Q_c^2 = 0.895 \text{ GeV}^2$ ,  $\beta_0 = 9$ , and  $\Lambda_{QCD} = 0.2 \text{ GeV}$ .

In Fig. 3.12, we show the LLCM, GBW, GRV, and IN results for the unintegrated gluon distribution of the proton  $\mathcal{F}_p(x, k_{\perp}^2)$  as a function of transverse momentum squared  $k_{\perp}^2$  for  $x = 10^{-1}, 10^{-2}, 10^{-3}$ , and  $10^{-4}$ . At small transverse momenta,  $k_{\perp}^2 \lesssim 0.1 \text{ GeV}^2$ , our model gives the largest values for  $\mathcal{F}_p(x, k_{\perp}^2)$ . As mentioned in the previous section, our LLCM unintegrated gluon distribution increases as  $1/\sqrt{k_{\perp}^2}$  with decreasing  $k_{\perp}^2$  as a consequence of the linear increase of the total dipole-proton cross section at large dipole sizes. In contrast, for  $k_{\perp}^2 \rightarrow 0$ , the unintegrated gluon distribution of GBW decreases as  $k_{\perp}^2$  and the one of IN as  $k_{\perp}^4$ . In the perturbative region,  $k_{\perp}^2 \gtrsim 1 \text{ GeV}^2$ , the unintegrated gluon distribution of the LLCM becomes smaller than the one of GRV and IN but is still larger than the one of GBW. Moreover, the LLCM, GRV, and IN unintegrated gluon distributions become parallel for  $x \lesssim 10^{-2}$  and drop as  $1/k_{\perp}^2$  for large  $k_{\perp}^2$ . This perturbative QCD behavior is not reproduced by the GBW unintegrated gluon distribution which decreases exponentially with increasing  $k_{\perp}^2$ .

The  $x$ -dependence of the LLCM, GBW, GRV, and IN unintegrated gluon distributions  $\mathcal{F}_p(x, k_{\perp}^2)$  is shown for transverse momenta squared  $k_{\perp}^2 = 0.1, 0.5, 10$ , and  $50 \text{ GeV}^2$  in Fig. 3.13. In the non-perturbative region,  $k_{\perp}^2 = 0.1 \text{ GeV}^2$  and  $k_{\perp}^2 = 0.5 \text{ GeV}^2$ , the LLCM, GBW, and IN unintegrated gluon distributions show a weak  $x$ -dependence. In the perturbative region,  $k_{\perp}^2 = 10 \text{ GeV}^2$  and  $k_{\perp}^2 = 50 \text{ GeV}^2$ , the  $x$ -dependence of the unintegrated gluon distributions becomes stronger. The LLCM, GRV, and IN unintegrated gluon distributions show nearly the same rise with decreasing  $x$ . In contrast, the GBW unintegrated gluon distribution increases much faster as  $x$  decreases.

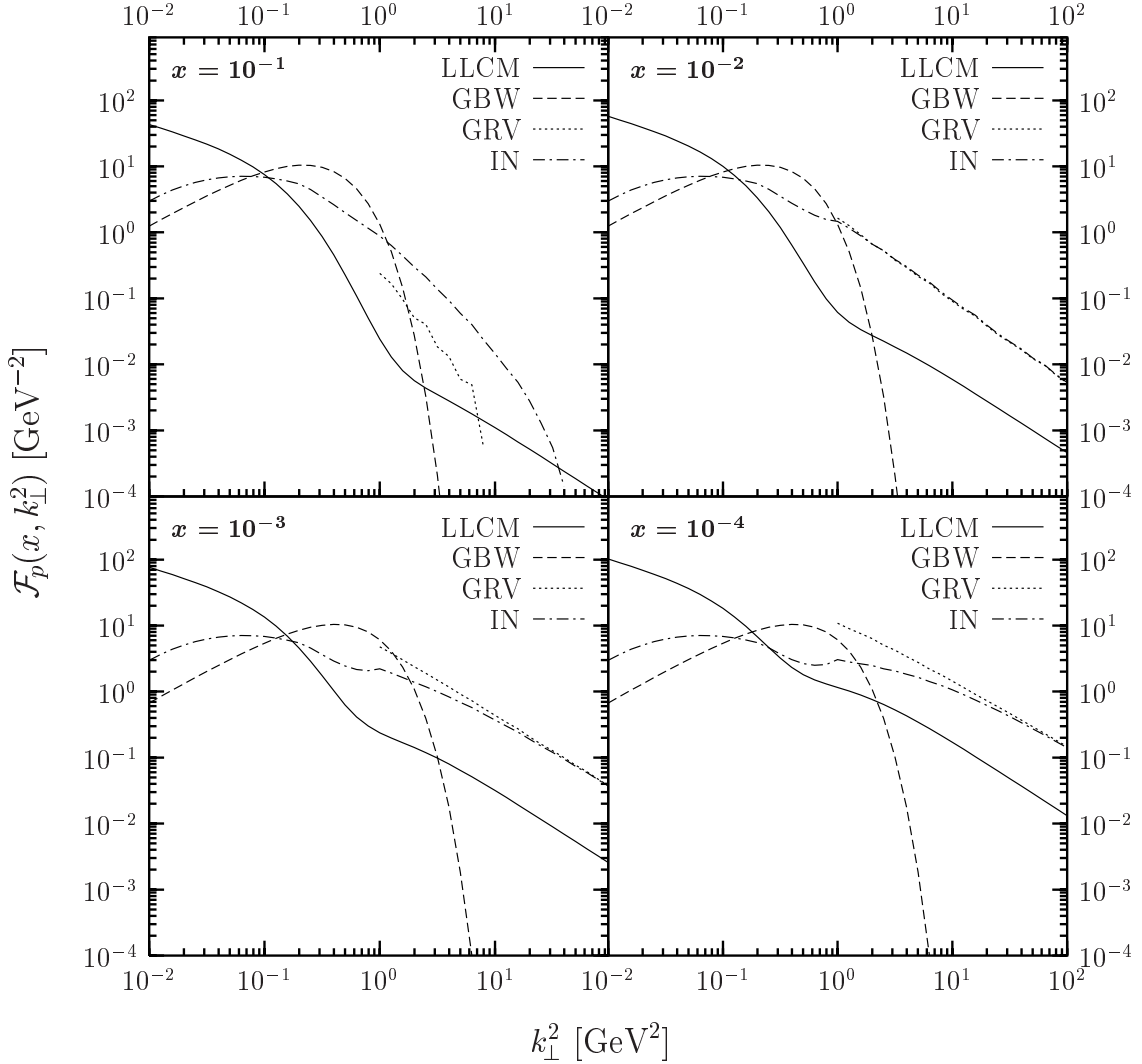


Figure 3.12: The unintegrated gluon distribution of the proton  $\mathcal{F}_p(x, k_\perp^2)$  as a function of transverse momentum squared  $k_\perp^2$  at Bjorken- $x$  values of  $10^{-1}$ ,  $10^{-2}$ ,  $10^{-3}$ , and  $10^{-4}$ . The different curves are obtained from our loop-loop correlation model (LLCM), the Golec-Biernat and Wüsthoff (GBW) model [72], the derivative of the Glück, Reya, and Vogt (GRV) parametrization of  $xG_p(x, Q^2)$  [87], and the Ivanov and Nikolaev (IN) approach [85].

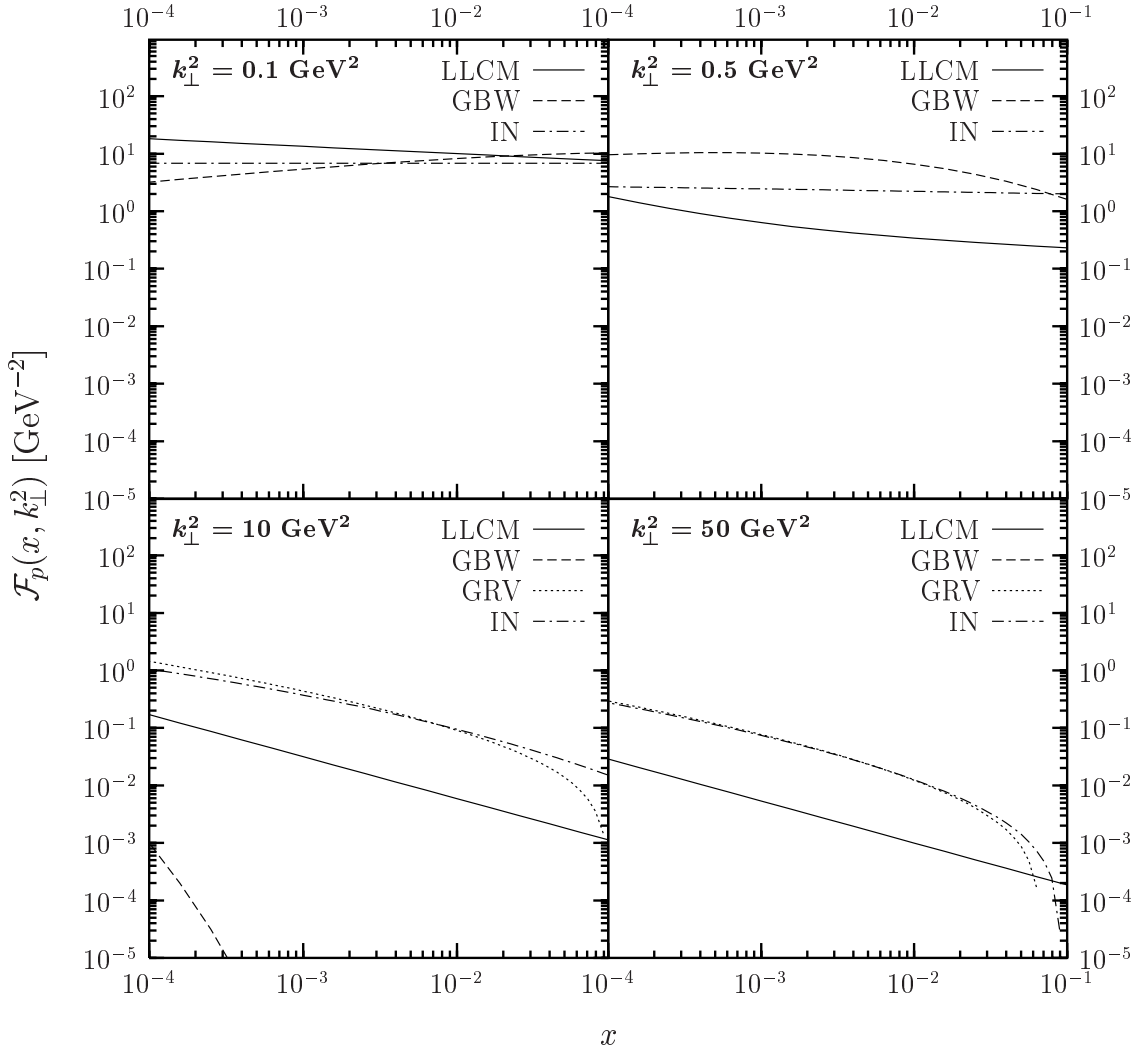


Figure 3.13: The unintegrated gluon distribution of the proton  $\mathcal{F}_p(x, k_\perp^2)$  as a function of Bjorken- $x$  at transverse momenta squared  $k_\perp^2 = 0.1, 0.5, 10, \text{ and } 50 \text{ GeV}^2$ . The different curves are obtained from our loop-loop correlation model (LLCM), the Golec-Biernat and Wüsthoff (GBW) model [72], the derivative of the Glück, Reya, and Vogt (GRV) parametrization of  $xG_p(x, Q^2)$  [87], and the Ivanov and Nikolaev (IN) approach [85]. Note that the GRV parametrization is only available for  $k_\perp^2 \geq 0.8 \text{ GeV}^2$ . Moreover, the GBW result for  $\mathcal{F}_p(x, k_\perp^2)$  is below  $10^{-5}$  for  $k_\perp^2 = 50 \text{ GeV}^2$ .

In addition to the one-scale unintegrated gluon distributions,  $\mathcal{F}(x, k_\perp^2)$ , discussed in this work, there exist also two-scale unintegrated gluon distributions,  $\mathcal{F}(x, k_\perp^2, \mu^2)$ . In the CCFM evolution equation [41], this additional scale  $\mu^2$  is related to the maximum angle allowed in the gluon emission. Two-scale unintegrated gluon distributions are obtained in the approach of Blümlein [89], Jung and Salam [90], Kimber, Martin, and Ryskin [91], and in the linked dipole chain (LDC) model [92, 93]. A comparison of their results can be found in [93, 94] where also the one-scale unintegrated gluon distributions of Kwiecinski, Martin and Stasto [95], and Ryskin and Shabelski [96] are discussed.



# Chapter 4

## Impact Parameter Profiles and Gluon Saturation

In this chapter we study saturation effects that manifest the unitarity of the  $S$ -matrix at high c.m. energies. We investigate the scattering amplitude in impact parameter space where the  $S$ -matrix unitarity limit becomes most explicit. In fact, the  $S$ -matrix unitarity imposes the *black disc limit* on the height of such impact parameter profiles. We show explicitly that our model respects the black disc limit. Furthermore, the width of the impact parameter profiles is shown to increase logarithmically at asymptotic energies as needed to guarantee the Froissart bound [7].

We compute the impact parameter profiles for hadron-hadron and longitudinal photon-proton scattering. Concrete energy values are determined at which the profiles saturate at the black disc limit for small impact parameters. The impact parameter profiles provide an intuitive geometrical picture for the energy dependence of the scattering process as they illustrate the evolution of the opacity and size of the interacting particles with increasing c.m. energy. We use the explicit black disc limit of the profiles in the following chapter to localize saturation effects in experimental observables.

Using a leading twist, next-to-leading order DGLAP relation, we estimate the *impact parameter dependent gluon distribution* of the proton  $xG(x, Q^2, |\vec{b}_\perp|)$  from the profile function for longitudinal photon-proton scattering. We find a low- $x$  saturation of  $xG(x, Q^2, |\vec{b}_\perp|)$  as a manifestation of the  $S$ -matrix unitarity. The implications on the integrated gluon distribution  $xG(x, Q^2)$  are studied and compared with complementary investigations of gluon saturation.

The results shown in this chapter are obtained with the  $T$ -matrix element given

in (2.6.6), the model parameters explained in Sec. 2.7, and the hadron and photon wave functions discussed extensively in Appendix B.

## 4.1 S-Matrix Unitarity and Impact Parameter Profiles

In this section we show that our model respects the *S*-matrix unitarity limit in impact parameter space of the scattering amplitude.

The impact parameter dependence of the scattering amplitude is given by  $\mathcal{T}(s, |\vec{b}_\perp|)$ ,

$$T(s, t = -\vec{q}_\perp^2) = 4s \int d^2 b_\perp e^{i\vec{q}_\perp \cdot \vec{b}_\perp} \mathcal{T}(s, |\vec{b}_\perp|) \quad (4.1.1)$$

and in particular by the *profile function*

$$J(s, |\vec{b}_\perp|) = 2 \operatorname{Im} \mathcal{T}(s, |\vec{b}_\perp|) , \quad (4.1.2)$$

which describes the *blackness* or *opacity* of the interacting particles as a function of the impact parameter  $|\vec{b}_\perp|$  and the c.m. energy  $\sqrt{s}$ . In fact, the profile function (4.1.2) determines every observable if the  $T$ -matrix is — as in our model — purely imaginary.

The *S*-matrix unitarity,  $SS^\dagger = S^\dagger S = 1\mathbb{I}$ , leads directly to the *unitarity condition* in impact parameter space [97, 98]

$$\operatorname{Im} \mathcal{T}(s, |\vec{b}_\perp|) = |\mathcal{T}(s, |\vec{b}_\perp|)|^2 + G_{inel}(s, |\vec{b}_\perp|) , \quad (4.1.3)$$

where  $G_{inel}(s, |\vec{b}_\perp|) \geq 0$  is the inelastic overlap function [99].<sup>1</sup> This unitarity condition imposes an absolute limit on the profile function

$$0 \leq 2|\mathcal{T}(s, |\vec{b}_\perp|)|^2 \leq J(s, |\vec{b}_\perp|) \leq 2 \quad (4.1.4)$$

and the inelastic overlap function,  $G_{inel}(s, |\vec{b}_\perp|) \leq 1/4$ . At high energies, however, the elastic amplitude is expected to be purely imaginary. Consequently, the solution of (4.1.3) reads

$$J(s, |\vec{b}_\perp|) = 1 \pm \sqrt{1 - 4G_{inel}(s, |\vec{b}_\perp|)} \quad (4.1.5)$$

and leads with the minus sign corresponding to the physical situation to the *reduced unitarity bound*

$$0 \leq J(s, |\vec{b}_\perp|) \leq 1 . \quad (4.1.6)$$

---

<sup>1</sup>Integrating (4.1.3) over the impact parameter space and multiplying by a factor of 4 one obtains the relation  $\sigma^{tot}(s) = \sigma^{el}(s) + \sigma^{inel}(s)$ .

Reaching the *black disc limit* or *maximum opacity* at a certain impact parameter  $|\vec{b}_\perp|$ ,  $J(s, |\vec{b}_\perp|) = 1$ , corresponds to maximal inelastic absorption  $G_{inel}(s, |\vec{b}_\perp|) = 1/4$  and equal elastic and inelastic contributions to the total cross section at that impact parameter.

In our model, every reaction is reduced to dipole-dipole scattering with well defined dipole sizes  $|\vec{r}_i|$  and longitudinal quark momentum fractions  $z_i$ . The unitarity condition in our model becomes, therefore, most explicit in the profile function

$$J_{DD}(s, |\vec{b}_\perp|, z_1, |\vec{r}_1|, z_2, |\vec{r}_2|) = \int \frac{d\phi_1}{2\pi} \int \frac{d\phi_2}{2\pi} \left[ 1 - S_{DD}(s, \vec{b}_\perp, z_1, \vec{r}_1, z_2, \vec{r}_2) \right], \quad (4.1.7)$$

where  $\phi_i$  describes the dipole orientation, i.e. the angle between  $\vec{r}_i$  and  $\vec{b}_\perp$ , and  $S_{DD}$  describes *elastic dipole-dipole scattering*

$$S_{DD} = \frac{2}{3} \cos\left(\frac{1}{3}\chi^{NP}(s)\right) \cos\left(\frac{1}{3}\chi^P(s)\right) + \frac{1}{3} \cos\left(\frac{2}{3}\chi^{NP}(s)\right) \cos\left(\frac{2}{3}\chi^P(s)\right) \quad (4.1.8)$$

with the purely real-valued eikonal functions  $\chi^{NP}(s)$  and  $\chi^P(s)$  defined in (2.6.4). Because of  $|S_{DD}| \leq 1$ , a consequence of the cosine functions in (4.1.8) describing multiple gluonic interactions,  $J_{DD}$  respects the absolute limit (4.1.4). Thus, the elastic dipole-dipole scattering respects the unitarity condition (4.1.3). At high energies, the arguments of the cosine functions in  $S_{DD}$  become so large that these cosines average to zero in the integration over the dipole orientations. This leads to the black disc limit  $J_{DD}^{max} = 1$  reached at high energies first for small impact parameters.

If one considers the scattering of two dipoles with fixed orientation, the inelastic overlap function obtained from the unitarity constraint (4.1.3),

$$\begin{aligned} & G_{inel}^{DD}(s, |\vec{b}_\perp|) \\ &= \frac{1}{4} \left( 1 - \left[ \frac{2}{3} \cos\left(\frac{1}{3}\chi^{NP}(s)\right) \cos\left(\frac{1}{3}\chi^P(s)\right) + \frac{1}{3} \cos\left(\frac{2}{3}\chi^{NP}(s)\right) \cos\left(\frac{2}{3}\chi^P(s)\right) \right]^2 \right), \end{aligned} \quad (4.1.9)$$

shows nonphysical behavior with increasing energy. This behavior is a consequence of artificially fixing the orientations of the dipoles. If one averages over the dipole orientations as in all high-energy reactions considered in this work, no unphysical behavior is observed.

## 4.2 Profile Function for Hadron-Hadron Scattering

In this section we show the c.m. energy and impact parameter dependence of the hadron-hadron scattering amplitude, determine the energy values at which saturation effects set in as a manifestation of the  $S$ -matrix unitarity, and compute the

logarithmic rise of the profile width at asymptotic c.m. energies which is equivalent to the Froissart bound [7].

The profile function for hadron-hadron (hh) scattering

$$J_{hh}(s, |\vec{b}_\perp|) = \int dz_1 d^2 r_1 \int dz_2 d^2 r_2 |\psi_h(z_1, \vec{r}_1)|^2 |\psi_h(z_2, \vec{r}_2)|^2 \left[ 1 - S_{DD}(s, \vec{b}_\perp, z_1, \vec{r}_1, z_2, \vec{r}_2) \right] \quad (4.2.1)$$

is obtained from (4.1.7) by weighting the dipole sizes  $|\vec{r}_i|$  and longitudinal quark momentum fractions  $z_i$  with the hadron wave functions  $|\psi_h(z_i, \vec{r}_i)|^2$  from Appendix B.

The profile functions for proton-proton, pion-proton, and kaon-proton scattering are shown in Fig. 4.1 for c.m. energies  $\sqrt{s}$  from 10 GeV to  $10^8$  GeV. The profiles are obtained with model parameters from Sec. 2.7 and the hadron extensions  $S_p = 0.86$  fm,  $S_\pi = 0.607$  fm, and  $S_K = 0.55$  fm used in the Gaussian hadron wave functions. Up to  $\sqrt{s} \approx 100$  GeV, the profiles have approximately a Gaussian shape. Above  $\sqrt{s} = 1$  TeV, they significantly develop into broader and higher profiles until the black disc limit is reached for  $\sqrt{s} \approx 10^6$  GeV and  $|\vec{b}_\perp| = 0$ . At this point, the cosine functions in  $S_{DD}$  average to zero

$$\int dz_1 d^2 r_1 \int dz_2 d^2 r_2 |\psi_h(z_1, \vec{r}_1)|^2 |\psi_h(z_2, \vec{r}_2)|^2 S_{DD}(\sqrt{s} \gtrsim 10^6 \text{ GeV}, |\vec{b}_\perp| = 0, \dots) \approx 0 \quad (4.2.2)$$

so that the hadron wave function normalizations determine the maximum opacity

$$J_{hh}^{max} = \int dz_1 d^2 r_1 \int dz_2 d^2 r_2 |\psi_h(z_1, \vec{r}_1)|^2 |\psi_h(z_2, \vec{r}_2)|^2 = 1. \quad (4.2.3)$$

Once the maximum opacity is reached at a certain impact parameter, the profile function saturates at that  $|\vec{b}_\perp|$  and extends towards larger impact parameters with increasing energy. Thus, the multiple gluonic interactions important to respect the S-matrix unitarity constraint (4.1.3) lead to saturation for  $\sqrt{s} \gtrsim 10^6$  GeV. The above behavior of the profile functions illustrates the evolution of the hadron with increasing c.m. energy. The hadron is gray and of small transverse size at small  $\sqrt{s}$  but becomes blacker and more transversally extended with increasing  $\sqrt{s}$  until it reaches the black disc limit in its center at  $\sqrt{s} \approx 10^6$  GeV. Beyond this energy, the hadron cannot become blacker in its central region but in its periphery with continuing transverse growth. Furthermore, the hadron boundary seems to stay diffusive as claimed also in [100].

The differences between the profile functions for  $pp$  ( $p\bar{p}$ ),  $\pi^\pm p$ , and  $K^\pm p$  scattering especially at low energies result from the different transverse hadron extensions,  $S_p = 0.86$  fm  $>$   $S_\pi = 0.607$  fm  $>$   $S_K = 0.55$  fm, cf. Appendix B. For the smaller pion and kaon extensions the short distance physics described by the perturbative

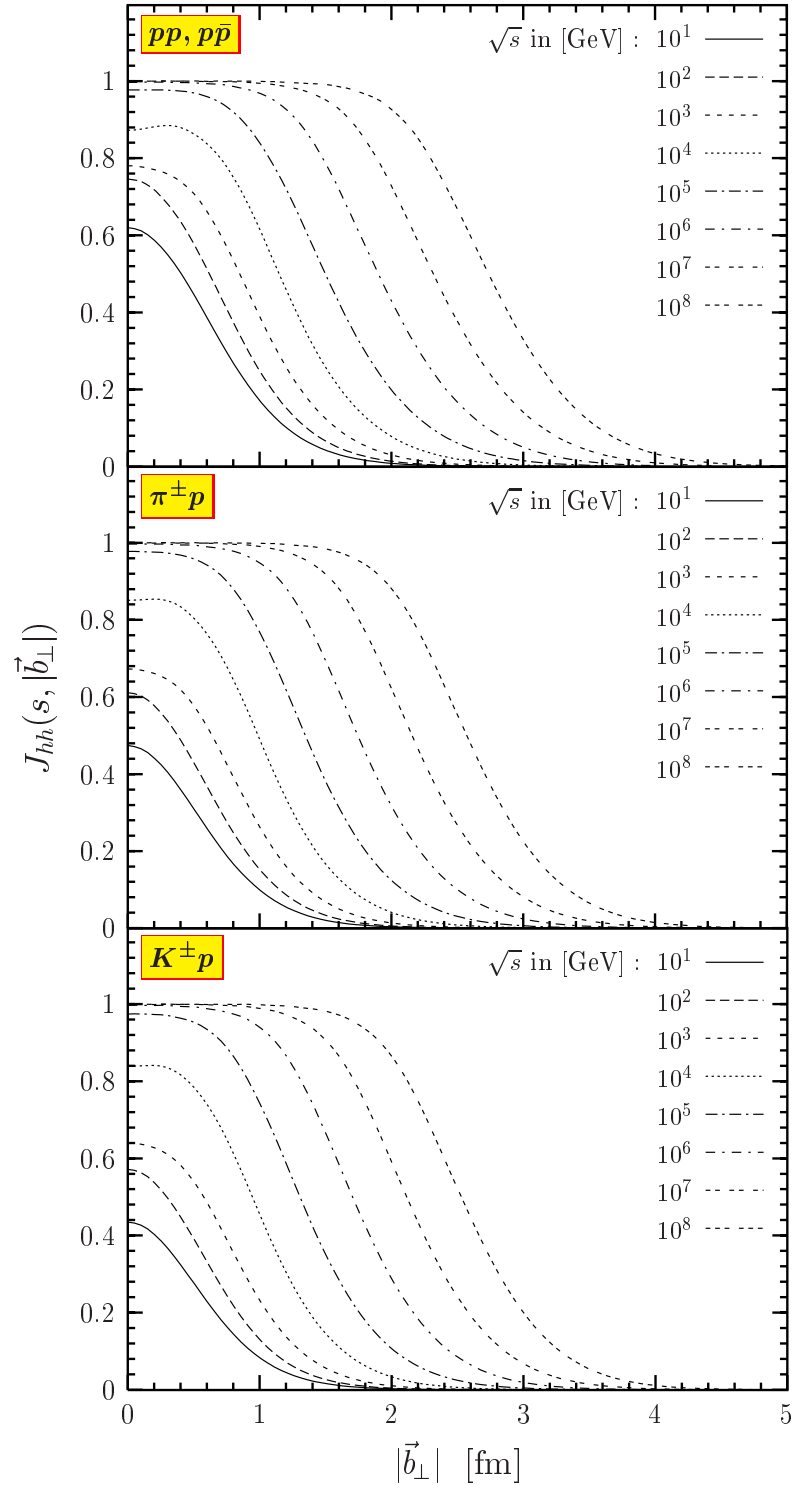


Figure 4.1: The profile function for proton-proton, pion-proton, and kaon-proton scattering  $J_{hh}(s, |\vec{b}_\perp|)$  is shown versus the impact parameter  $|\vec{b}_\perp|$  for c.m. energies  $\sqrt{s}$  from 10 GeV to  $10^8$  GeV. The unitarity limit (4.1.4) corresponds to  $J_{hh}(s, |\vec{b}_\perp|) = 2$  and the black disc limit (4.1.6) to  $J_{hh}(s, |\vec{b}_\perp|) = 1$ .

component becomes more important and leads to a stronger energy increase ( $\epsilon^P = 0.73 > \epsilon^{NP} = 0.125$ ) of the  $\pi^\pm p$  and  $K^\pm p$  profile functions as compared to the one of the  $pp$  ( $p\bar{p}$ ) scattering in the c.m. energy range  $10 \text{ GeV} \leq \sqrt{s} \leq 10^6 \text{ GeV}$ . The black disc limit (4.2.3) is identical for  $\pi p$ ,  $Kp$ , and  $pp$  ( $p\bar{p}$ ) scattering due to the same pion, kaon, and proton wave function normalization (B.1.2). The smaller size of pions and kaons in comparison to the one of protons demands, however, slightly higher c.m. energies to reach the black disc limit and yields narrower  $\pi^\pm p$  and  $K^\pm p$  profile widths for energies somewhat larger than  $\sqrt{s} = 10^6 \text{ GeV}$ . At asymptotic energies, however, the profile widths become universal (hadron size independent) as shown below.

According to our model the black disc limit will not be reached at LHC. Our prediction of  $\sqrt{s} \approx 10^6 \text{ GeV} = 10^3 \text{ TeV}$  for the onset of the black disc limit in proton-proton collisions is about two orders of magnitude beyond the LHC energy  $\sqrt{s} = 14 \text{ TeV}$ . This is in contrast, for example, with [101], where the value predicted for the onset of the black disc limit is  $\sqrt{s} = 2 \text{ TeV}$ , i.e. small enough to be reached at LHC. However, we feel confidence in our LHC prediction since our profile function  $J_{pp}(s, |\vec{b}_\perp|)$  yields good agreement with experimental data for cross sections up to the highest energies as shown in chapter 5.

The discussion in the previous section, the black disc limit in Eq. (4.2.3), and Fig. 4.1 show that our model respects the  $S$ -matrix unitarity in impact parameter space of the scattering amplitude. This, however, is not enough to guarantee the Froissart bound [7] for total hadronic cross sections at asymptotic c.m. energies. Since the latter are obtained by integrating the impact parameter profiles over all impact parameters, difficulties with the Froissart bound can arise if the black disc radius  $R(s)$ , i.e., the impact parameter range for which  $J_{hh}(s, |\vec{b}_\perp|) \approx 1$ , increases with growing c.m. energy faster than  $\ln(s)$ . A calculation of the energy dependence of  $R(s)$ , which agrees with the numerical results shown in chapter 5, shows below that the Froissart bound is respected in our model.

For impact parameters much larger than the dipole sizes involved in the interaction,  $|\vec{b}_\perp| \gg |\vec{r}_1|, |\vec{r}_2|$ , the leading term of the  $\chi^P$ -function (2.5.18) which is needed in the computation of  $R(s)$  reads

$$\begin{aligned} \chi^P(s, \vec{r}_1, \vec{r}_2, \vec{b}_\perp) = & \left( \frac{s \vec{r}_1^2 \vec{r}_2^2}{s_0 R_0^4} \right)^{\epsilon^P/2} \frac{g^2}{2\pi} \sqrt{\frac{\pi}{2}} \frac{e^{-m_G |\vec{b}_\perp|}}{\sqrt{m_G |\vec{b}_\perp|}} \left[ \left( \frac{1}{4|\vec{b}_\perp|^2} + \frac{m_G}{2|\vec{b}_\perp|} \right) |\vec{r}_1| |\vec{r}_2| \cos(\phi) \right. \\ & \left. - \left( \frac{5}{4|\vec{b}_\perp|^2} + \frac{2m_G}{|\vec{b}_\perp|} + m_G^2 \right) |\vec{r}_1| |\vec{r}_2| \cos(\phi_1) \cos(\phi_2) \right], \end{aligned}$$

(4.2.4)

where  $\phi$  denotes the angle between the dipoles  $\vec{r}_1$  and  $\vec{r}_2$  and  $\phi_i$  the angle between the impact parameter  $\vec{b}_\perp$  and dipole  $\vec{r}_i$ . To obtain the above result we have used the longitudinal momentum fractions  $z_1 = z_2 = 0.5$ . These values, however, do not affect the asymptotic behaviour of  $R(s)$ .

With the above energy and impact parameter dependence of the  $\chi^P$ -function, the black disc radius  $R(s)$  can now be obtained as follows: For c.m. energies  $\sqrt{s} \gg 10^6$  GeV, perturbative correlations  $\chi^P$  dominate the dipole-dipole scattering amplitude  $S_{DD}$  in (4.2.1) because of the stronger energy dependence ( $\epsilon^P = 0.73 > \epsilon^{NP} = 0.125$ ) as compared with non-perturbative correlations  $\chi^{NP}$ . Consequently,  $\cos(c\chi^P)$  oscillates much more than  $\cos(c\chi^{NP})$  in the integration over the dipole sizes and orientations ( $c = 1/3$  or  $2/3$ ), i.e., only  $\cos(c\chi^P)$  needs to be considered here. The condition for the black disc radius  $R(s)$  results from the fact that for  $|\vec{b}| \leq R(s)$  the functions  $\cos(c\chi^P)$  have to average to zero when integrated over the dipole orientations in the profile function (4.2.1). This is the case when the main contribution to the  $\chi^P$ -function (4.2.4) at large impact parameters fulfills the relation

$$\left( \frac{s}{s_0} \frac{\vec{r}_1^2 \vec{r}_2^2}{R_0^4} \right)^{\epsilon^P/2} \frac{g^2}{2\pi} \sqrt{\frac{\pi}{2}} \frac{e^{-m_G R(s)}}{\sqrt{m_G R(s)}} m_G^2 |\vec{r}_1| |\vec{r}_2| = C_0 \gg \pi. \quad (4.2.5)$$

Taking the logarithm on both sides of Eq (4.2.5), one obtains for the leading contribution to the black disc radius  $R(s)$  at ultra-high energies

$$R(s) = \frac{\epsilon^P}{2m_G} \ln \left( \frac{s}{\bar{s}_0} \right) = \frac{\epsilon^P}{M_{GB}^P} \ln \left( \frac{s}{\bar{s}_0} \right), \quad (4.2.6)$$

where  $\bar{s}_0$  denotes the reference energy,  $m_G$  the gluon mass, and  $M_{GB}^P = 2m_G$  the “glueball mass” obtained from our perturbative contribution [17]. The logarithmic increase of  $R(s)$  is equivalent to the Froissart bound [7] since  $\sigma_{hh}^{tot}(s) = 2\pi R(s)^2$  at asymptotic energies (see the following chapter).

For the derivation of the Froissart bound the powerlike energy dependence  $s^{\epsilon^P}$  as well as the exponential fall off  $\exp(-m_G b)$  are crucial. This provides an a posteriori justification for the powerlike energy ansatz used in this work. The exponential  $|\vec{b}_\perp|$ -decrease exists because of the non-zero gluon mass  $m_G$  which has been introduced in the gluon propagator as a cutoff to suppress the effect of perturbative physics in the non-perturbative region of small momenta.

The coefficient  $\epsilon^P/(2m_G)$  of the  $\ln(s)$  term contains the energy exponent  $\epsilon^P$  of the perturbative contribution and the semiperturbative parameter  $m_G$  which determines the interplay between perturbative and non-perturbative physics. This coefficient

is *universal* for all hadron interactions computed within our model. Different coefficients have been used in the literature: Lukaszuk and Martin [102] have used the factor  $\sqrt{\pi}/m_\pi$  ( $m_\pi$  is the pion mass), Heisenberg [103] has obtained by considering the dynamics of the scattering  $\sqrt{\pi}/(2m_\pi)$ , Ferreiro et al. [104] have deduced from the Color Glass Condensate model the result  $\sqrt{\pi/2}(4\ln(2)\alpha_s N_c)/(\pi m_\pi)$  with the BFKL-exponent  $4\ln(2)\alpha_s N_c/\pi$ , and Dosch et al. [105] have updated Heisenberg's approach to get  $\sqrt{\pi}/(2M_{GB})$ . So far the coefficient of the  $\ln(s)$  term is not conclusive.

A universal black disc radius  $R(s)$  means that all hadrons are of the same size at asymptotic energies. This behavior starts becoming visible in the profile functions shown in Fig. 4.1 at the highest energies. The universal increase exhibits itself most explicitly in total hadronic cross sections which we discuss extensively in chapter 5.

### 4.3 Profile Function for Photon-Proton Scattering

In this section we compute the photon-proton scattering amplitude which is very appropriate to study the dependence of profile functions on the size of the scattered particles by varying the photon virtuality.

The profile function for a longitudinal photon  $\gamma_L^*$  scattering off a proton  $p$

$$J_{\gamma_L^* p}(s, |\vec{b}_\perp|, Q^2) = \int dz_1 d^2 r_1 \int dz_2 d^2 r_2 |\psi_{\gamma_L^*}(z_1, \vec{r}_1, Q^2)|^2 |\psi_p(z_2, \vec{r}_2)|^2 \times [1 - S_{DD}(\vec{b}_\perp, s, z_1, \vec{r}_1, z_2, \vec{r}_2)] \quad (4.3.1)$$

is calculated with the longitudinal photon wave function  $|\psi_{\gamma_L^*}(z_i, \vec{r}_i, Q^2)|^2$  given in (B.2.2). In this way, the profile function (4.3.1) is ideally suited for the investigation of dipole size effects since the photon virtuality  $Q^2$  determines the transverse size of the dipole (3.3.1) into which the photon fluctuates before it interacts with the proton.

Figure 4.2 shows the  $|\vec{b}_\perp|$  dependence of the profile function  $J_{\gamma_L^* p}(s, |\vec{b}_\perp|, Q^2)$  divided by  $\alpha/\pi$  for c.m. energies  $\sqrt{s}$  from  $10\text{ GeV}$  to  $10^9\text{ GeV}$  and photon virtualities  $Q^2 = 1, 10, \text{ and } 100\text{ GeV}^2$ , where  $\alpha$  is the fine-structure constant. One clearly sees that the qualitative behavior of this rescaled profile function is similar to the one for hadron-hadron scattering. However, the black disc limit induced by the underlying dipole-dipole scattering depends on the photon virtuality  $Q^2$  and is given by the normalization of the longitudinal photon wave function

$$J_{\gamma_L^* p}^{max}(Q^2) = \int dz d^2 r |\psi_{\gamma_L^*}(z, \vec{r}, Q^2)|^2 \quad (4.3.2)$$

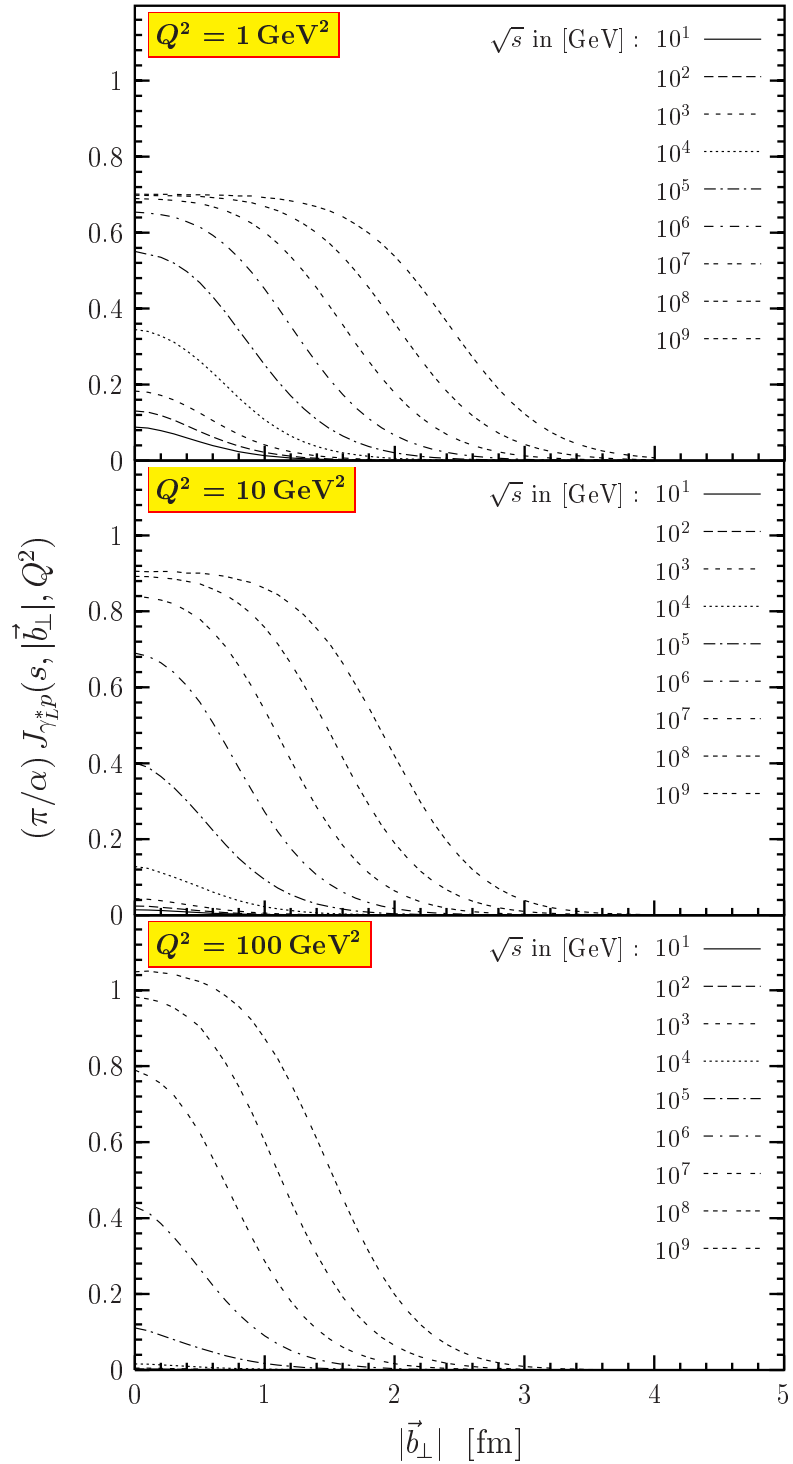


Figure 4.2: The profile function for a longitudinal photon scattering off a proton  $J_{\gamma_L^* p}^*(s, |\vec{b}_\perp|, Q^2)$  divided by  $\alpha/\pi$  is shown versus the impact parameter  $|\vec{b}_\perp|$  for photon virtualities  $Q^2 = 1, 10$ , and  $100 \text{ GeV}^2$  and c.m. energies  $\sqrt{s}$  from  $10 \text{ GeV}$  to  $10^9 \text{ GeV}$ . The value of the black disc limit  $J_{\gamma_L^* p}^{max}(Q^2)$  and the width of the profiles depend on  $Q^2$ .

since the proton wave function is normalized to one.

The photon virtuality  $Q^2$  does not only determine the absolute value of the black disc limit and the c.m. energy at which it is reached but also the width of the profiles at fixed  $\sqrt{s}$  as illustrated in Fig. 4.2. With increasing resolution  $Q^2$ , i.e. decreasing dipole sizes,  $|\vec{r}_{\gamma_L^*}|^2 \propto 1/Q^2$ , the absolute value of the black disc limit grows and higher energies are needed to reach this limit.<sup>2</sup> This can be seen most explicitly in Fig. 4.3 where the  $\sqrt{s}$  dependence of  $J_{\gamma_L^* p}(s, |\vec{b}_\perp| = 0, Q^2)$  divided by  $\alpha/\pi$  is presented for  $Q^2 = 1, 10$ , and  $100 \text{ GeV}^2$ . The growth of the absolute

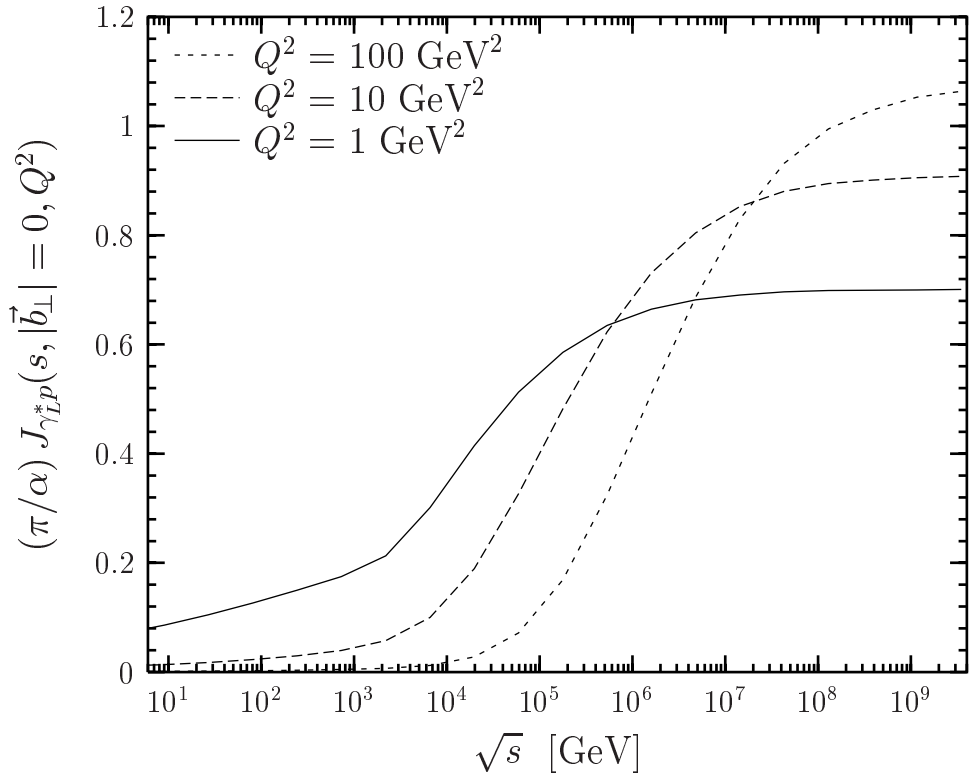


Figure 4.3: The profile function for a longitudinal photon scattering off a proton  $J_{\gamma_L^* p}(s, |\vec{b}_\perp|, Q^2)$  divided by  $\alpha/\pi$  is shown versus the c.m. energy  $\sqrt{s}$  at zero impact parameter ( $|\vec{b}_\perp| = 0$ ) for photon virtualities  $Q^2 = 1, 10$ , and  $100 \text{ GeV}^2$ .

value of the black disc limit is simply due to the normalization of the longitudinal photon wave function while the requirement of higher energies to reach this limit is due to the decreasing interaction strength with decreasing dipole size. The latter explains also why the energies needed to reach the black disc limit in  $\pi^\pm p$  and  $K^\pm p$

<sup>2</sup>Note that the Bjorken  $x$  at which the black disc limit is reached decreases with increasing photon virtuality  $Q^2$ . (See also Fig. 4.4)

scattering are slightly higher than in  $pp$  ( $\bar{p}p$ ) scattering. In comparison to the hadron-hadron profile function, Fig. 4.2 shows explicitly that the width of the  $\gamma_L^*p$  profiles at energies somewhat beyond the black disc limit decreases with decreasing photon size  $|\vec{r}_{\gamma_L^*}|^2 \propto 1/Q^2$ . Furthermore, comparing  $\gamma_L^*p$  scattering at  $Q^2 = 1 \text{ GeV}^2$  with  $pp$  scattering quantitatively, the black disc limit  $J_{\gamma_L^*p}^{\max}(Q^2 = 1 \text{ GeV}^2) = 0.00164$  is about three orders of magnitude smaller because of the photon wave function normalization ( $\propto \alpha/\pi$ ). At  $|\vec{b}_\perp| = 0$  it is reached at an energy of  $\sqrt{s} \approx 10^8 \text{ GeV}$ , which is about two orders of magnitude higher because of the smaller dipoles involved.

The way in which the profile function  $J_{\gamma_L^*p}(s, |\vec{b}_\perp|, Q^2)$  approaches the black disc limit at high energies depends on the shape of the proton and longitudinal photon wave function at small dipole sizes  $|\vec{r}_{1,2}|$ . At high energies, dipoles of typical sizes  $0 \leq |\vec{r}_{1,2}| \leq R_0(s_0/s)^{1/4}$  give the main contribution to  $S_{\gamma_L^*p} = 1 - J_{\gamma_L^*p}$  because of (2.6.4) and the fact that the contribution of the large dipole sizes averages to zero upon integration over the dipole orientations, cf. also (4.2.2). Since  $S_{\gamma_L^*p}$  is a measure of the proton transmittance, this means that only small dipoles can penetrate the proton at high energies. Increasing the energy further, even these small dipoles are absorbed and the black disc limit is reached. However, the dependence of the profile function on the short distance behavior of normalizable wave functions is weak which can be understood as follows. Because of color transparency, the eikonal functions  $\chi^{NP}(s)$  and  $\chi^P(s)$  are small for small dipole sizes  $0 \leq |\vec{r}_{1,2}| \leq R_0(s_0/s)^{1/4}$  at large  $\sqrt{s}$ . Consequently,  $S_{DD} \approx 1$  and

$$\begin{aligned} J_{\gamma_L^*p}(s, |\vec{b}_\perp|, Q^2) \\ \approx J_{\gamma_L^*p}^{\max}(Q^2) - 4\pi^2 \int_0^1 dz_1 \int_0^{r_c(s)} dr_1 r_1 |\psi_{\gamma_L^*}(z_1, r_1, Q^2)|^2 \int_0^1 dz_2 \int_0^{r_c(s)} dr_2 r_2 |\psi_p(z_2, r_2)|^2 \end{aligned} \quad (4.3.3)$$

where  $r_c(s) \approx R_0(s_0/s)^{1/4}$ . Clearly, the linear behavior from the phase space factors  $r_{1,2}$  dominates over the  $r_{1,2}$ -dependence of normalizable wave functions.<sup>3</sup> More generally, for any profile function involving normalizable wave functions, the way in which the black disc limit is approached depends only weakly on the short distance behavior of the wave functions.

---

<sup>3</sup>For our choice of the wave functions in (4.3.3), one sees very explicitly that the specific Gaussian behavior of  $|\psi_p(z_2, r_2)|^2$  and the logarithmic short distance behavior of  $|\psi_{\gamma_L^*}(z_1, r_1, Q^2)|^2$  is dominated by the phase space factors  $r_{1,2}$ .

## 4.4 A Scenario for Gluon Saturation

In this section we estimate the *impact parameter dependent gluon distribution* of the proton  $xG(x, Q^2, |\vec{b}_\perp|)$ . Using a leading twist, next-to-leading order QCD relation between  $xG(x, Q^2)$  and the longitudinal structure function  $F_L(x, Q^2)$ , we relate  $xG(x, Q^2, |\vec{b}_\perp|)$  to the profile function  $J_{\gamma_L^* p}(s = Q^2/x, |\vec{b}_\perp|, Q^2)$  and find low- $x$  saturation of  $xG(x, Q^2, |\vec{b}_\perp|)$  as a manifestation of  $S$ -matrix unitarity. The resulting  $xG(x, Q^2, |\vec{b}_\perp|)$  is, of course, only an estimate since our profile function contains also higher twist contributions. Furthermore, in the considered low- $x$  region, the leading twist, next-to-leading order QCD formula may be inadequate as higher twist contributions [106] and higher order QCD corrections [107, 108] are expected to become important. Nevertheless, still assuming a close relation between  $F_L(x, Q^2)$  and  $xG(x, Q^2)$  at low  $x$ , we think that our approach provides some insight into the gluon distribution as a function of the impact parameter and into its saturation.

The *gluon distribution* of the proton  $xG(x, Q^2)$  has the following meaning:  $xG(x, Q^2)dx$  gives the momentum fraction of the proton which is carried by the gluons in the interval  $[x, x+dx]$  as seen by probes of virtuality  $Q^2$ . The *impact parameter dependent gluon distribution*  $xG(x, Q^2, |\vec{b}_\perp|)$  is the gluon distribution  $xG(x, Q^2)$  at a given impact parameter  $|\vec{b}_\perp|$  so that

$$xG(x, Q^2) = \int d^2 b_\perp xG(x, Q^2, |\vec{b}_\perp|) . \quad (4.4.1)$$

In leading twist, next-to-leading order QCD, the gluon distribution  $xG(x, Q^2)$  is related to the structure functions  $F_L(x, Q^2)$  and  $F_2(x, Q^2)$  of the proton [109]

$$F_L(x, Q^2) = \frac{\alpha_s}{\pi} \left[ \frac{4}{3} \int_x^1 \frac{dy}{y} \left( \frac{x}{y} \right)^2 F_2(y, Q^2) + 2 \sum_f e_f^2 \int_x^1 \frac{dy}{y} \left( \frac{x}{y} \right)^2 \left( 1 - \frac{x}{y} \right) y G(y, Q^2) \right] \quad (4.4.2)$$

where  $\sum_f e_f^2$  is a flavor sum over the quark charges squared. For four active flavors and  $x \lesssim 10^{-3}$ , (4.4.2) can be approximated as follows [110]

$$xG(x, Q^2) \approx \frac{3}{5} 5.8 \left[ \frac{3\pi}{4\alpha_s} F_L(0.417x, Q^2) - \frac{1}{1.97} F_2(0.75x, Q^2) \right] . \quad (4.4.3)$$

For typical  $\Lambda_{QCD} = 100 - 300$  MeV and  $Q^2 = 50 - 100$  GeV $^2$ , the coefficient of  $F_L$  in (4.4.3),  $3\pi/(4\alpha_s) = \mathcal{O}(10)$ , is large compared to the one of  $F_2$ . Taking into account also the values of  $F_2$  and  $F_L$ , in this  $Q^2$  region and for  $x \lesssim 10^{-3}$ , the gluon distribution is mainly determined by the longitudinal structure function. The latter

can be expressed in terms of the profile function for longitudinal photon-proton scattering using the optical theorem (cf. (5.1.1))

$$F_L(x, Q^2) = \frac{Q^2}{4\pi^2\alpha} \sigma_{\gamma_L^* p}^{tot}(x, Q^2) = \frac{Q^2}{4\pi^2\alpha} 2 \int d^2 b_\perp J_{\gamma_L^* p}(x, |\vec{b}_\perp|, Q^2), \quad (4.4.4)$$

where the  $s$ -dependence of the profile function is rewritten in terms of the Bjorken scaling variable,  $x = Q^2/s$ . Neglecting the  $F_2$  term in (4.4.3), consequently, the gluon distribution reduces to

$$xG(x, Q^2) \approx 1.305 \frac{Q^2}{\pi^2\alpha_s} \frac{\pi}{\alpha} \int d^2 b_\perp J_{\gamma_L^* p}(0.417x, |\vec{b}_\perp|, Q^2). \quad (4.4.5)$$

Comparing (4.4.1) with (4.4.5), it seems natural to relate the integrand of (4.4.5) to the impact parameter dependent gluon distribution

$$xG(x, Q^2, |\vec{b}_\perp|) \approx 1.305 \frac{Q^2}{\pi^2\alpha_s} \frac{\pi}{\alpha} J_{\gamma_L^* p}(0.417x, |\vec{b}_\perp|, Q^2). \quad (4.4.6)$$

The black disc limit of the profile function for longitudinal photon-proton scattering (4.3.2) imposes accordingly an upper bound on  $xG(x, Q^2, |\vec{b}_\perp|)$

$$xG(x, Q^2, |\vec{b}_\perp|) \leq xG^{max}(Q^2) \approx 1.305 \frac{Q^2}{\pi^2\alpha_s} \frac{\pi}{\alpha} J_{\gamma_L^* p}^{max}(Q^2), \quad (4.4.7)$$

which is the low- $x$  saturation value of the gluon distribution  $xG(x, Q^2, |\vec{b}_\perp|)$  in our approach. With  $\pi J_{\gamma_L^* p}^{max}(Q^2)/\alpha \approx 1$  as shown in Fig. 4.3, a compact approximation of (4.4.7) is obtained

$$xG(x, Q^2, |\vec{b}_\perp|) \leq xG^{max}(Q^2) \approx \frac{Q^2}{\pi^2\alpha_s}, \quad (4.4.8)$$

which is consistent with the results in [108, 111, 112] and indicates strong color-field strengths  $G_{\mu\nu}^a \sim 1/\sqrt{\alpha_s}$  as well.

According to our relations (4.4.6) and (4.4.7), the *blackness* described by the profile function is a measure for the gluon density and the *black disc limit* corresponds to the maximum gluon density reached at the impact parameter under consideration. In accordance with the behavior of the profile function  $J_{\gamma_L^* p}$ , see Fig. 4.2, the gluon distribution  $xG(x, Q^2, |\vec{b}_\perp|)$  decreases with increasing impact parameter for given values of  $x$  and  $Q^2$ . The gluon density, consequently, has its maximum in the geometrical center of the proton, i.e. at zero impact parameter, and decreases towards the periphery. With decreasing  $x$  at given  $Q^2$ , the gluon distribution  $xG(x, Q^2, |\vec{b}_\perp|)$

increases and extends towards larger impact parameters just as the profile function  $J_{\gamma_L^* p}$  for increasing  $s$ . The saturation of the gluon distribution  $xG(x, Q^2, |\vec{b}_\perp|)$  sets in first in the center of the proton ( $|\vec{b}_\perp| = 0$ ) at very small Bjorken  $x$ .

In Fig. 4.4, the gluon distribution  $xG(x, Q^2, |\vec{b}_\perp| = 0)$  is shown as a function of  $x$  for  $Q^2 = 1, 10$ , and  $100 \text{ GeV}^2$ , where the relation (4.4.6) has been used also for low photon virtualities. Evidently, the gluon distribution  $xG(x, Q^2, |\vec{b}_\perp| = 0)$

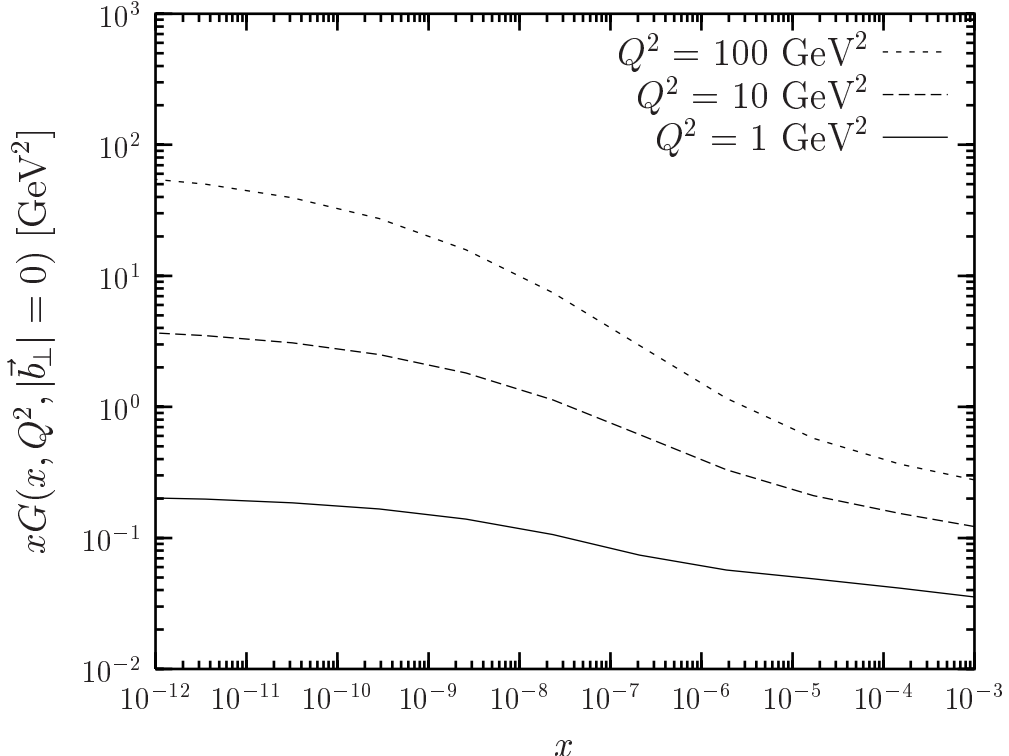


Figure 4.4: The gluon distribution of the proton at zero impact parameter  $xG(x, Q^2, |\vec{b}_\perp| = 0)$  is shown as a function of  $x$  for  $Q^2 = 1, 10$ , and  $100 \text{ GeV}^2$ . The results are obtained within the approximation (4.4.6).

saturates at very low values of  $x \lesssim 10^{-10}$  for  $Q^2 \gtrsim 1 \text{ GeV}^2$ . The photon virtuality  $Q^2$  determines the saturation value (4.4.7) and the Bjorken- $x$  at which it is reached (cf. also Fig. 4.2). For larger  $Q^2$ , the low- $x$  saturation value is larger and is reached at smaller values of  $x$ , as claimed also in [113]. Moreover, the growth of  $xG(x, Q^2, |\vec{b}_\perp| = 0)$  with decreasing  $x$  becomes stronger with increasing  $Q^2$ . This results from the stronger energy increase of the perturbative component,  $\epsilon^P = 0.73$ , that becomes more important with decreasing dipole size.

According to our approach, the onset of the  $xG(x, Q^2, |\vec{b}_\perp|)$ -saturation appears

for  $Q^2 \gtrsim 1 \text{ GeV}^2$  at  $x \lesssim 10^{-10}$ , which is far below the  $x$ -region accessible at HERA ( $x \gtrsim 10^{-6}$ ). Even for THERA ( $x \gtrsim 10^{-7}$ ), gluon saturation is not predicted for  $Q^2 \gtrsim 1 \text{ GeV}^2$ . Munier et al. have also shown in a recent publication [114] that the black disc limit is not reached in the energy range of HERA. However, since the HERA data can be described by models with and without saturation embedded [113], the present situation is not conclusive.<sup>4</sup>

Note that the  $S$ -matrix unitarity condition (4.1.3) together with (4.4.6) requires the saturation of the impact parameter dependent gluon distribution  $xG(x, Q^2, |\vec{b}_\perp|)$  but not the saturation of the integrated gluon distribution  $xG(x, Q^2)$ . Due to multiple gluonic interactions in our model, this requirement is fulfilled, as can be seen from Fig. 4.2 and relation (4.4.6). Indeed, approximating the gluon distribution  $xG(x, Q^2, |\vec{b}_\perp|)$  in the saturation regime of very low  $x$  by a step-function

$$xG(x, Q^2, |\vec{b}_\perp|) \approx xG^{max}(Q^2) \Theta(R(x, Q^2) - |\vec{b}_\perp|), \quad (4.4.9)$$

where  $R(x, Q^2)$  denotes the black disc radius (or the full width at half maximum of the profile function), one obtains with (4.4.1), (4.4.7) and (4.4.8) the integrated gluon distribution

$$xG(x, Q^2) \approx 1.305 \frac{Q^2 R^2(x, Q^2)}{\pi \alpha_s} \frac{\pi}{\alpha} J_{\gamma_L^* p}^{max}(Q^2) \approx \frac{Q^2 R^2(x, Q^2)}{\pi \alpha_s}, \quad (4.4.10)$$

which does not saturate because of the increase of the effective proton radius  $R(x, Q^2)$  with decreasing  $x$ . Nevertheless, although  $xG(x, Q^2)$  does not saturate, the saturation of  $xG(x, Q^2, |\vec{b}_\perp|)$  leads to a slow-down from powerlike to square logarithmic (see (4.2.6)) growth of  $xG(x, Q^2)$  towards small  $x$ .<sup>5</sup> Interestingly, our result (4.4.10) coincides with the result of Mueller and Qiu [108].

Finally, it must be emphasized that the low- $x$  saturation of  $xG(x, Q^2, |\vec{b}_\perp|)$ , required in our approach by the  $S$ -matrix unitarity, is realized by *multiple gluonic interactions*. In other approaches that describe the evolution of the gluon distribution with varying  $x$  and  $Q^2$ , *gluon recombination* leads to gluon saturation [107, 108, 116–118], which is reached when the probability of a gluon splitting up into two is equal to the probability of two gluons fusing into one. A more phenomenological understanding of saturation is attempted in [71, 119].

---

<sup>4</sup>So far, the most striking hint for saturation in the present HERA data at  $x \approx 10^{-4}$  and  $Q^2 < 2 \text{ GeV}^2$  has been the turnover of  $dF_2(x, Q^2)/d\ln(Q^2)$  towards small  $x$  in the Caldwell plot [115], which is still a controversial issue due to the correlation of  $Q^2$  and  $x$  values.

<sup>5</sup>This is analogous to the slow down of the total  $pp$  cross section at high c.m. energy as soon as the corresponding profile function  $J_{pp}(s, |\vec{b}_\perp|)$  reaches its black disc limit as shown in Sec. 5.1.



# Chapter 5

## Comparison with Data and Saturation Effects in Observables

In this chapter we show the phenomenological performance of our model. We compute total, differential, and elastic cross sections, structure functions, and diffractive slopes for hadron-hadron, photon-proton, and photon-photon scattering, compare the results with experimental data including cosmic ray data, and provide predictions for future experiments. Making use of the explicit saturation of the impact parameter profiles at the black disc limit, the corresponding energy values, and the logarithmic rise of the black disc radius studied in the preceding chapter, we show explicitly manifestations of  $S$ -matrix unitarity limits in experimental observables.

Using the  $T$ -matrix element given in (2.6.6), we compute the *pomeron* contribution to  $pp$ ,  $p\bar{p}$ ,  $\pi^\pm p$ ,  $K^\pm p$ ,  $\gamma^* p$ , and  $\gamma\gamma$  reactions in terms of the universal dipole-dipole scattering amplitude  $S_{DD}$ . This allows one to compare reactions induced by hadrons and photons in a systematic way. In fact, it is our aim to provide a unified description of all these reactions and to show in this way that the pomeron contribution to the above reactions is universal and can be traced back to the dipole-dipole scattering amplitude  $S_{DD}$ .

Our model describes pomeron ( $C = +1$  gluon exchange) but neither odderon ( $C = -1$  gluon exchange) nor reggeon exchange (quark-antiquark exchange) as discussed in Sec. 2.5. Only in the computation of the hadronic total cross sections the reggeon contribution is added [29, 120]. This improves the agreement with the data for  $\sqrt{s} \lesssim 100$  GeV and describes exactly the differences between hadron-hadron and antihadron-hadron reactions.

The model parameters have been adjusted in fits to the high-energy scattering

data shown in this chapter. The resulting parameter set given in Sec. 2.7 and Appendix B is used throughout this work.

## 5.1 Total Cross Sections

The total cross section for the high-energy reaction  $ab \rightarrow X$  is related via the *optical theorem* to the imaginary part of the forward elastic scattering amplitude and can also be expressed in terms of the profile function (4.1.2)

$$\sigma_{ab}^{tot}(s) = \frac{1}{s} \text{Im} T(s, t=0) = 2 \int d^2 b_\perp J_{ab}(s, |\vec{b}_\perp|), \quad (5.1.1)$$

where  $a$  and  $b$  label the initial particles whose masses were neglected as they are small in comparison to the c.m. energy  $\sqrt{s}$ .

We compute the pomeron contribution to the total cross section,  $\sigma_{ab}^{tot, P}(s)$ , from the  $T$ -matrix (2.6.6), as explained above, and add only here a reggeon contribution of the form [29, 120]

$$\sigma_{ab}^{tot, R}(s) = X_{ab} \left( \frac{s}{1 \text{ GeV}^2} \right)^{-0.4525}, \quad (5.1.2)$$

where  $X_{ab}$  depends on the reaction considered:  $X_{pp} = 56.08 \text{ mb}$ ,  $X_{p\bar{p}} = 98.39 \text{ mb}$ ,  $X_{\pi^+ p} = 27.56 \text{ mb}$ ,  $X_{\pi^- p} = 36.02 \text{ mb}$ ,  $X_{K^+ p} = 8.15 \text{ mb}$ ,  $X_{K^- p} = 26.36 \text{ mb}$ ,  $X_{\gamma p} = 0.129 \text{ mb}$ , and  $X_{\gamma\gamma} = 605 \text{ nb}$ . Accordingly, we obtain the total cross section

$$\sigma_{ab}^{tot}(s) = \sigma_{ab}^{tot, P}(s) + \sigma_{ab}^{tot, R}(s) \quad (5.1.3)$$

for  $pp$ ,  $p\bar{p}$ ,  $\pi^\pm p$ ,  $K^\pm p$ ,  $\gamma p$  and  $\gamma\gamma$  scattering.

The good agreement of the computed total cross sections with the experimental data is shown in Fig. 5.1. Here the solid lines represent the theoretical results for  $pp$ ,  $\pi^+ p$ ,  $K^+ p$ ,  $\gamma p$ , and  $\gamma\gamma$  scattering and the dashed lines the ones for  $p\bar{p}$ ,  $\pi^- p$ , and  $K^- p$  scattering. The dot-dashed line represents  $2\pi(\epsilon^P/2m_G)^2 \ln^2(s/\bar{s}_0)$  with  $\sqrt{\bar{s}} = 20 \text{ GeV}$ . The  $pp$ ,  $p\bar{p}$ ,  $\pi^\pm p$ ,  $K^\pm p$ ,  $\gamma p$  [3] and  $\gamma\gamma$  data [121] taken at accelerators are indicated by the closed circles while the closed squares (Fly's eye data) [122] and the open circles (Akeno data) [123] indicate cosmic ray data. Concerning the photon-induced reactions, only real photons are considered which are, of course, only transverse polarized.

The prediction for the total  $pp$  cross section at LHC ( $\sqrt{s} = 14 \text{ TeV}$ ) is  $\sigma_{pp}^{tot} = 114.2 \text{ mb}$  in good agreement with the cosmic ray data. Compared with other works, our LHC prediction is close to the one of Block et al. [124],  $\sigma_{pp}^{tot} = 108 \pm 3.4 \text{ mb}$ , but considerably larger than the one of Donnachie and Landshoff [29],  $\sigma_{pp}^{tot} = 101.5 \text{ mb}$ .

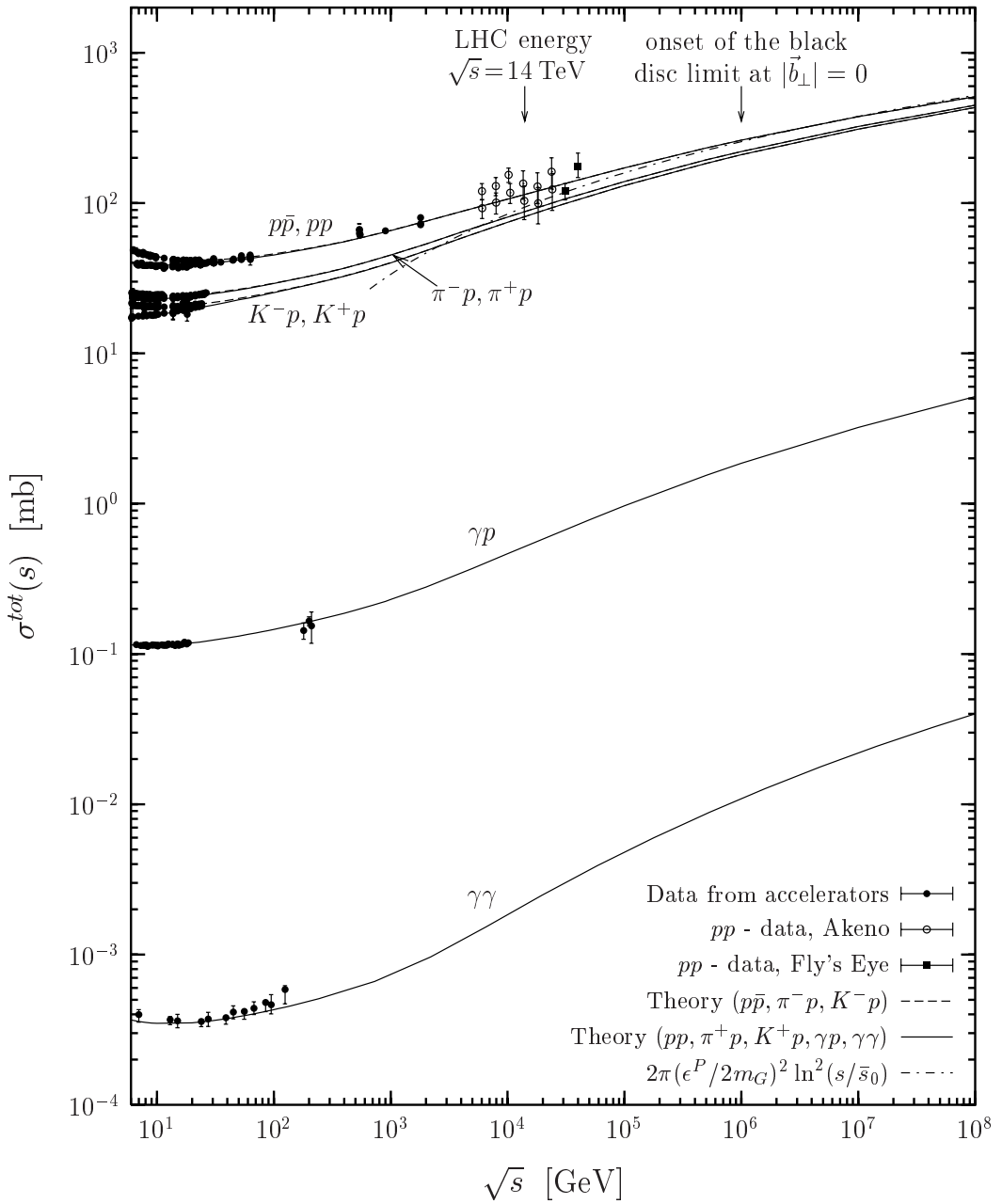


Figure 5.1: The total cross section  $\sigma^{tot}$  is shown as a function of the c.m. energy  $\sqrt{s}$  for  $pp$ ,  $p\bar{p}$ ,  $\pi^\pm p$ ,  $K^\pm p$ ,  $\gamma p$  and  $\gamma\gamma$  scattering. The solid lines represent the model results for  $pp$ ,  $\pi^+ p$ ,  $K^+ p$ ,  $\gamma p$  and  $\gamma\gamma$  scattering and the dashed lines the ones for  $p\bar{p}$ ,  $\pi^- p$ , and  $K^- p$  scattering. The dot-dashed line represents  $2\pi(\epsilon^P/2m_G)^2 \ln^2(s/\bar{s}_0)$  with  $\sqrt{\bar{s}} = 20$  GeV. The  $pp$ ,  $p\bar{p}$ ,  $\pi^\pm p$ ,  $K^\pm p$ ,  $\gamma p$  [3] and  $\gamma\gamma$  data [121] taken at accelerators are indicated by the closed circles while the closed squares (Fly's eye data) [122] and the open circles (Akemo data) [123] indicate cosmic ray data. The arrows at the top point to the LHC energy,  $\sqrt{s} = 14$  TeV, and to the onset of the black disc limit in  $pp$  ( $p\bar{p}$ ) reactions,  $\sqrt{s} \approx 10^6$  GeV.

The differences between  $ab$  and  $\bar{ab}$  reactions for  $\sqrt{s} \lesssim 100$  GeV result solely from the different reggeon contributions which die out rapidly as the energy increases. The pomeron contribution to  $ab$  and  $\bar{ab}$  reactions is, in contrast, identical and increases as the energy increases. It thus governs the total cross sections for  $\sqrt{s} \gtrsim 100$  GeV where the results for  $ab$  and  $\bar{ab}$  reactions coincide.

The differences between  $pp$  ( $p\bar{p}$ ),  $\pi^\pm p$ , and  $K^\pm p$  scattering result from the different transverse extension parameters,  $S_p = 0.86$  fm  $> S_\pi = 0.607$  fm  $> S_K = 0.55$  fm, cf. Appendix B. Since a smaller transverse extension parameter favors smaller dipoles, the total cross section becomes smaller, and the short distance physics described by the perturbative component becomes more important and leads to a stronger energy growth due to  $\epsilon^P = 0.73 > \epsilon^{NP} = 0.125$ . In fact, the ratios  $\sigma_{pp}^{tot}/\sigma_{\pi p}^{tot}$  and  $\sigma_{pp}^{tot}/\sigma_{Kp}^{tot}$  converge slowly towards unity with increasing energy as can already be seen in Fig. 5.1.

For real photons, the transverse size is governed by the constituent quark masses  $m_f(Q^2 = 0)$ , cf. Appendix B, where the light quarks have the strongest effect, i.e.  $\sigma_{\gamma p}^{tot} \propto 1/m_{u,d}^2$  and  $\sigma_{\gamma\gamma}^{tot} \propto 1/m_{u,d}^4$ . Furthermore, in comparison with hadron-hadron scattering, there is the additional suppression factor of  $\alpha$  for  $\gamma p$  and  $\alpha^2$  for  $\gamma\gamma$  scattering coming from the photon-dipole transition. In the  $\gamma\gamma$  reaction, also the box diagram contributes [120, 125] but is neglected since its contribution to the total cross section is less than 1% [74].

It is worthwhile mentioning that total cross sections for  $pp$  ( $p\bar{p}$ ),  $\pi^\pm p$ , and  $K^\pm p$  scattering do not depend on the width  $\Delta z_h$  of the longitudinal quark momentum distribution in the hadrons (B.1.1) since the underlying dipole-dipole scattering process is independent of the longitudinal quark momentum fraction  $z_i$  for  $t = 0$ . On the two-gluon-exchange level, this is shown analytically in chapter 3.

Saturation effects as a manifestation of the  $S$ -matrix unitarity can be seen in Fig. 5.1. Having investigated the profile function for hadron-hadron scattering, we know that this profile function becomes higher and broader with increasing energy until it saturates the black disc limit first for zero impact parameter ( $|\vec{b}_\perp| = 0$ ) at  $\sqrt{s} \approx 10^6$  GeV. Beyond this energy, the profile function cannot become higher but expands towards larger values of  $|\vec{b}_\perp|$ . Consequently, the total cross section (5.1.1) increases no longer due to the growing blackness at the center but only due to the transverse expansion of the hadrons. This tames the growth of the total hadronic cross sections as can be seen for c.m. energies beyond  $\sqrt{s} \approx 10^6$  GeV in Fig. 5.1.

At energies far beyond the onset of the black disc limit at zero impact parameter, the profile function can be approximated by

$$J_{ab}^{approx}(s, |\vec{b}_\perp|) = N_a N_b \Theta\left(R(s) - |\vec{b}_\perp|\right) \quad (5.1.4)$$

where  $N_{a,b}$  denotes the normalization of the wave functions of the scattered particles and  $R(s)$  the black disc radius defined in Sec. 4.2 that reflects the effective radii of the interacting particles. Thus, the energy dependence of the total cross section (5.1.1) is driven exclusively by the increase of the transverse extension of the particles  $R(s)$

$$\sigma_{ab}^{tot}(s) = 2\pi N_a N_b R(s)^2, \quad (5.1.5)$$

which is known as *geometrical scaling* [126, 127]. Introducing the analytical result for the black disc radius  $R(s)$  at asymptotic energies (4.2.6) in the above equation, one obtaines the  $\ln^2$ -growth

$$\sigma_{ab}^{tot}(s) = 2\pi N_a N_b \left( \frac{\epsilon^P}{2m_G} \right)^2 \ln^2 \left( \frac{s}{\bar{s}_0} \right), \quad (5.1.6)$$

which coincides with the Froissart bound [7]. For hadron wave function normalizations  $N_{a,b} = 1$ , the total cross section (5.1.6) is independent of the hadron species involved in the hadron-hadron scattering at asymptotic energies. The hadronic cross sections start joining already at the highest energies shown in Fig. 5.1. Also for photons of different virtuality  $Q_1^2$  and  $Q_2^2$  one can check that the ratio of the total cross sections  $\sigma_{\gamma^* p}^{tot}(Q_1^2)/\sigma_{\gamma^* p}^{tot}(Q_2^2)$  converges to unity at asymptotic energies in agreement with the conclusion in [128].

The total cross section (5.1.6) obtained with the values for  $\epsilon^P$  and  $m_G$  from Sec. 2.7,  $N_{a,b} = 1$ , and the c.m. energy  $\sqrt{\bar{s}_0} = 20$  GeV is shown as a dot-dashed line for  $\sqrt{s} \geq 600$  GeV in Fig. 5.1. Evidently, the so obtained logarithmic growth coincides with the numerical result for the  $pp$  cross section at high energies. In fact, a transition from a powerlike to an  $\ln^2$ -increase of total cross sections seems to set in at about  $\sqrt{s} = 10^6$  GeV as visible in Fig. 5.1. Following the recent publications [105, 129], already fits to available forward scattering data support the universal  $\ln^2(s)$ -dependence of the cross sections.

## 5.2 Proton Structure Function

The total cross section for the scattering of a transverse ( $T$ ) and longitudinally ( $L$ ) polarized photon off the proton,  $\sigma_{\gamma_{T,L}^* p}^{tot}(x, Q^2)$ , at photon virtuality  $Q^2$  and c.m. energy<sup>1</sup> squared,  $s = Q^2/x$ , is equivalent to the *structure functions* of the proton

$$F_{T,L}(x, Q^2) = \frac{Q^2}{4\pi^2 \alpha} \sigma_{\gamma_{T,L}^* p}^{tot}(x, Q^2) \quad (5.2.1)$$

---

<sup>1</sup>Here,  $\sqrt{s}$  refers to the c.m. energy in the  $\gamma^* p$  system.

and

$$F_2(x, Q^2) = F_T(x, Q^2) + F_L(x, Q^2) . \quad (5.2.2)$$

Reactions induced by virtual photons are particularly interesting because the transverse separation of the quark-antiquark pair that emerges from the virtual photon decreases as the photon virtuality increases, cf. Eq. (3.3.1). With increasing virtuality, one probes therefore smaller transverse distance scales of the proton.

In Fig. 5.2, the  $Q^2$ -dependence of the total  $\gamma^*p$  cross section

$$\sigma_{\gamma^*p}^{tot}(s, Q^2) = \sigma_{\gamma_T^*p}^{tot}(s, Q^2) + \sigma_{\gamma_L^*p}^{tot}(s, Q^2) \quad (5.2.3)$$

is presented, where the model results (solid lines) are compared with the experimental data for c.m. energies from  $\sqrt{s} = 20$  GeV up to  $\sqrt{s} = 245$  GeV. Note the indicated scaling factors at different  $\sqrt{s}$  values. The low energy data at  $\sqrt{s} = 20$  GeV are from [130] while the data at higher energies have been measured at HERA by the H1 [131] and ZEUS collaboration [132]. At  $Q^2 = 0.012$  GeV $^2$ , also the photo-production ( $Q^2 = 0$ ) data from [133] are displayed.

In the window shown in Fig. 5.2, the model results are in reasonable agreement with the experimental data. The total  $\gamma^*p$  cross section levels off towards small values of  $Q^2$  as soon as the photon size  $|\vec{r}_\gamma|$ , i.e the resolution scale, becomes comparable to the proton size. Our model reproduces this behavior by using the perturbative photon wave functions with  $Q^2$ -dependent quark masses,  $m_f(Q^2)$ , that interpolate between the current (large  $Q^2$ ) and the constituent (small  $Q^2$ ) quark masses as explained in detail in Appendix B. The decrease of  $\sigma_{\gamma^*p}^{tot}$  with increasing  $Q^2$  results from the decreasing dipole sizes since small dipoles do not interact as strongly as large dipoles.

The  $x$ -dependence of the computed proton structure function  $F_2(x, Q^2)$  is shown in Fig. 5.3 for  $Q^2 = 0.3, 2.5, 12$  and  $120$  GeV $^2$  in comparison to the data measured by the H1 [134] and ZEUS [135] detector. Within our model, the increase of  $F_2(x, Q^2)$  towards small Bjorken  $x$  becomes stronger with increasing  $Q^2$  in agreement with the trend in the HERA data. This behavior results from the fast energy growth of the perturbative component that becomes more important with increasing  $Q^2$  due to the smaller dipole sizes involved.

As can be seen in Fig. 5.3, the data show a stronger increase with decreasing  $x$  than the model outside the low- $Q^2$  region. This results from the weak energy boost of the non-perturbative component that dominates  $F_2(x, Q^2)$  in our model. In fact, even for large  $Q^2$  the non-perturbative contribution overwhelms the perturbative one, which explains also the overestimation of the data for  $x \gtrsim 10^{-3}$ .

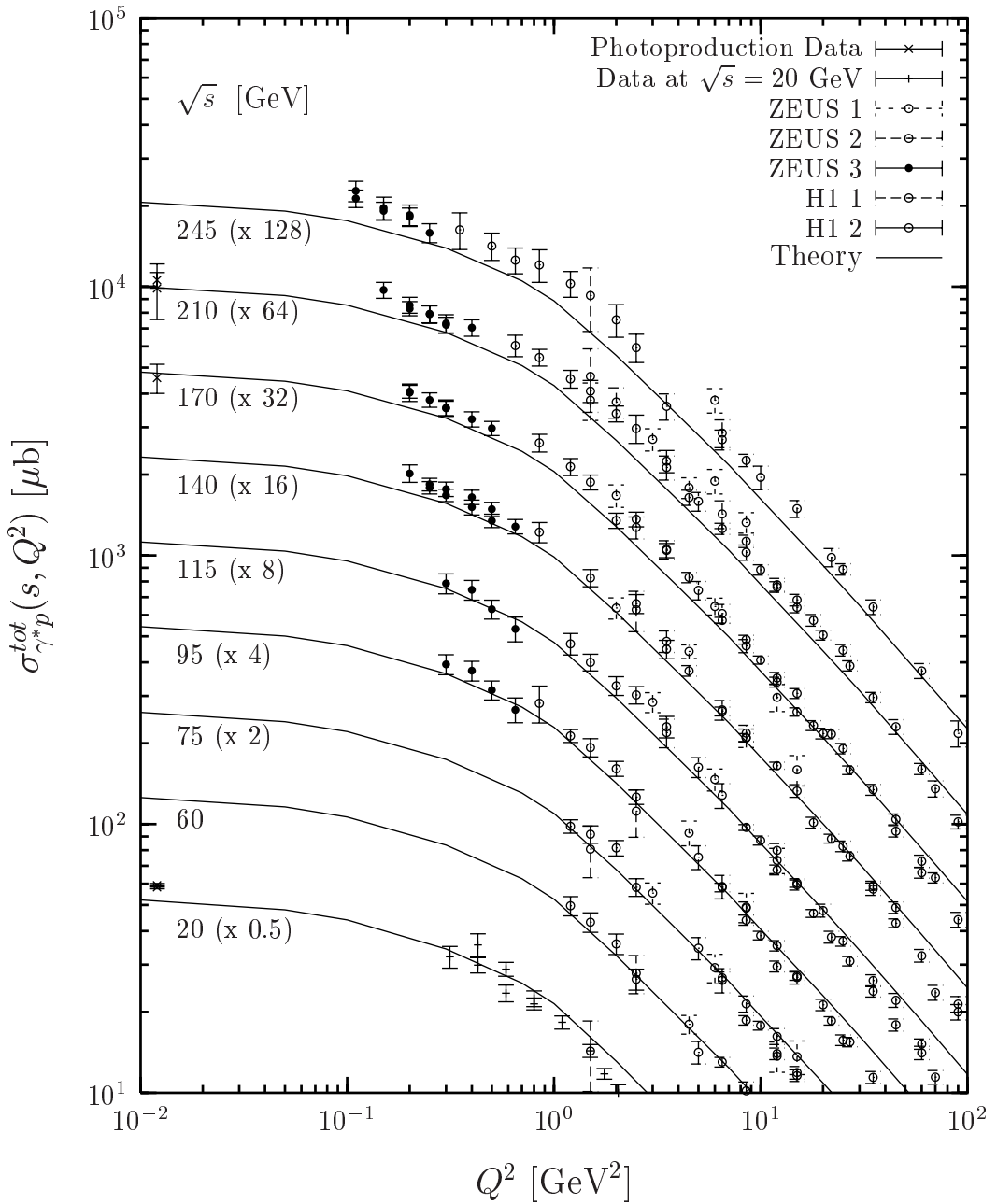


Figure 5.2: The total  $\gamma^*p$  cross section,  $\sigma_{\gamma^*p}^{tot}(s, Q^2)$ , is shown as a function of the photon virtuality  $Q^2$  for c.m. energies from  $\sqrt{s} = 20$  GeV to  $\sqrt{s} = 245$  GeV, where the model results (solid lines) and the experimental data at different  $\sqrt{s}$  values are scaled with the indicated factors. The low energy data at  $\sqrt{s} = 20$  GeV are from [130], the data at higher energies from the H1 [131] and ZEUS collaboration [132]. The photoproduction ( $Q^2 = 0$ ) data from [133] are displayed at  $Q^2 = 0.012$  GeV $^2$ .

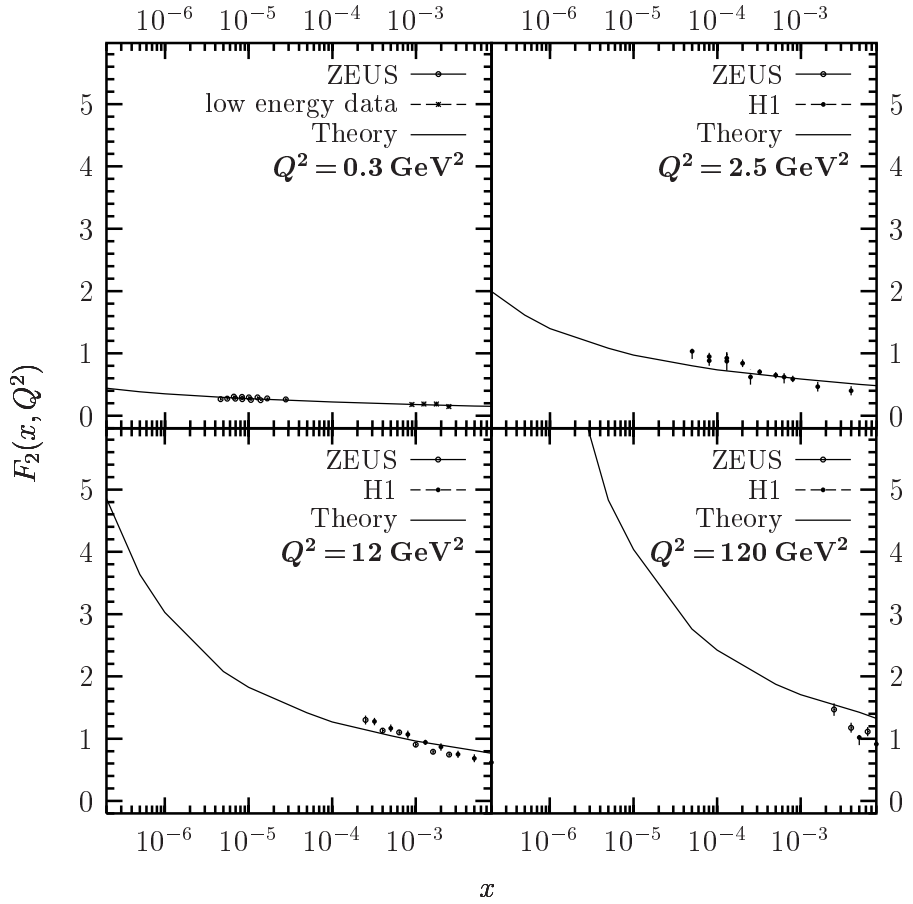


Figure 5.3: The  $x$ -dependence of the computed proton structure function  $F_2(x, Q^2)$  (solid line) is shown for  $Q^2 = 0.3, 2.5, 12$  and  $120 \text{ GeV}^2$  in comparison to the data measured by the H1 [134] and ZEUS [135] detector, and the low energy data at  $\sqrt{s} = 20 \text{ GeV}$  from [130].

This problem is typical for the SVM model applied to the scattering of a small size dipole off a proton. In an earlier application by Rüter [21], an additional cut-off was introduced to switch from the non-perturbative to the perturbative contribution as soon as one of the dipoles is smaller than  $r_{cut} = 0.16 \text{ fm}$ . This yields a better agreement with the data also for large  $Q^2$  but leads to a discontinuous dipole-proton cross section. In the model of Donnachie and Dosch [74], a similar SVM-based component is used also for dipoles smaller than  $R_c = 0.22 \text{ fm}$  with a strong energy boost instead of a perturbative component. Furthermore, their SVM-based component is tamed for large  $Q^2$  by an additional  $\alpha_s(Q^2)$  factor.

We did not follow these lines in order to keep a continuous,  $Q^2$ -independent dipole-proton cross section and, therefore, cannot improve the agreement with the  $F_2(x, Q^2)$  data without losing quality in the description of hadronic observables.

Since our non-perturbative component relies on lattice QCD, we are more confident in describing non-perturbative physics and, thus, put more emphasis on the hadronic observables. Admittedly, our model misses details of the proton structure that become visible with increasing  $Q^2$ . In comparison, most other existing models provide neither the profile functions nor a simultaneous description of hadronic and  $\gamma^*$ -induced processes. For example, the phenomenological model of Golec-Biernat and Wüsthoff [71, 72] provides a successful and economical description of the  $\gamma^*p$  reactions but cannot be applied to hadron-hadron reactions.

### 5.3 Slope Parameter $B$ of Elastic Forward Scattering

The *local slope* of elastic scattering  $B(s, t)$  is defined as

$$B(s, t) := \frac{d}{dt} \left( \ln \left[ \frac{d\sigma^{el}}{dt}(s, t) \right] \right) \quad (5.3.1)$$

and, thus, characterizes the diffractive peak of the differential elastic cross section  $d\sigma^{el}/dt(s, t)$  discussed below. Here, we concentrate on the slope for elastic forward ( $t = 0$ ) scattering also called *slope parameter*

$$B(s) := B(s, t = 0) = \frac{1}{2} \frac{\int d^2 b_\perp |\vec{b}_\perp|^2 J(s, |\vec{b}_\perp|)}{\int d^2 b_\perp J(s, |\vec{b}_\perp|)} = \frac{1}{2} \langle b^2 \rangle, \quad (5.3.2)$$

which measures the rms interaction radius  $\langle b^2 \rangle$  of the scattered particles, and does not depend on the opacity.

We compute the slope parameter with the profile function from the  $T$ -matrix (2.6.6) and neglect the reggeon contributions, which are relevant only at small c.m. energies, so that the same result is obtained for  $ab$  and  $\bar{a}\bar{b}$  scattering.

In Fig. 5.4, the resulting slope parameter  $B(s)$  is shown as a function of  $\sqrt{s}$  for  $pp$  and  $p\bar{p}$  scattering (solid line) and compared with the  $pp$  (open circles) and  $p\bar{p}$  (closed circles) data from [136–138]. As expected from the opacity independence of the slope parameter (5.3.2), saturation effects as seen in the total cross sections do not occur. Indeed, one observes an approximate  $B(s) \propto R^2(s) \propto \ln^2(s)$  growth for  $\sqrt{s} \gtrsim 10^4$  GeV. This behavior agrees, of course, with the transverse expansion of  $J_{pp}(s, |\vec{b}_\perp|)$  for increasing  $\sqrt{s}$  shown in Fig. 4.1. Analogous results are obtained also for  $\pi p$  and  $Kp$  scattering.

For the good agreement of our model with the data, the finite width of the longitudinal quark momentum distribution in the hadrons, i.e.  $\Delta z_p$ ,  $\Delta z_\pi$ , and  $\Delta z_K \neq 0$

in (B.1.1), is important as the numerator in (5.3.2) depends on this width. In fact,  $B(s)$  comes out more than 10% smaller with  $\Delta z_p$ ,  $\Delta z_\pi$ , and  $\Delta z_K = 0$ . The  $\Delta z_h$ -dependence of the non-forward scattering amplitude computed analytically on the two-gluon exchange level is shown explicitly in Appendix D. Furthermore, a strong growth of the perturbative component,  $\epsilon^P = 0.73$ , is important to achieve the increase of  $B(s)$  for  $\sqrt{s} \gtrsim 500$  GeV indicated by the data.

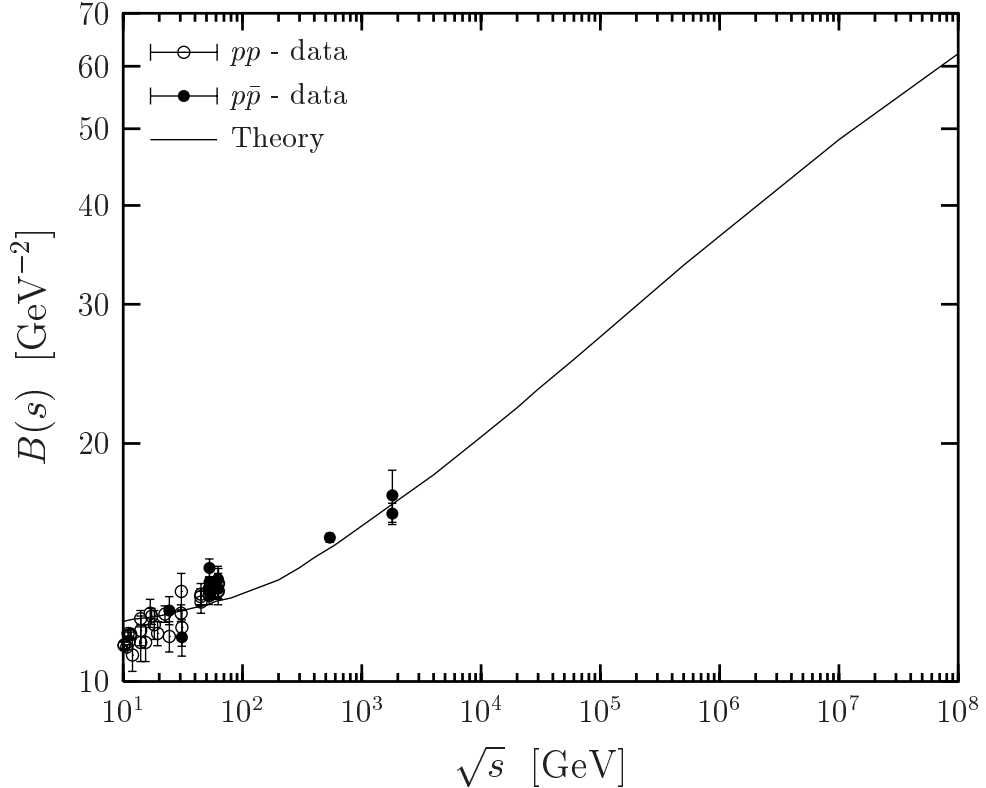


Figure 5.4: The elastic slope parameter  $B(s)$  is shown as a function of the c.m. energy  $\sqrt{s}$  for  $pp$  and  $p\bar{p}$  forward ( $t = 0$ ) scattering. The solid line represents the model result that is compared with the data for  $pp$  (open circles) and  $p\bar{p}$  (closed circles) reactions from [136–138].

It must be emphasized that only the simultaneous fit of the total cross section and the slope parameter provides the correct shape of the profile function  $J(s, |\vec{b}_\perp|)$ . This shape leads then automatically to a good description of the differential elastic cross section  $d\sigma^{el}/dt(s, t)$  as demonstrated below. Astonishingly, only few phenomenological models provide a satisfactory description of both quantities [70, 124]. In the approach of [14], for example, the total cross section is described correctly while the slope parameter exceeds the data by more than 20% already at  $\sqrt{s} = 23.5$  GeV and,

thus, indicates deficiencies in the form of  $J(s, |\vec{b}_\perp|)$ .

## 5.4 Differential Elastic Cross Sections

The *differential elastic cross section* obtained from the squared absolute value of the  $T$ -matrix element

$$\frac{d\sigma^{el}}{dt}(s, t) = \frac{1}{16\pi s^2} |T(s, t)|^2 \quad (5.4.1)$$

can be expressed for our purely imaginary  $T$ -matrix (2.6.6) in terms of the profile function

$$\frac{d\sigma^{el}}{dt}(s, t) = \frac{1}{4\pi} \left[ \int d^2 b_\perp e^{i\vec{q}_\perp \cdot \vec{b}_\perp} J(s, |\vec{b}_\perp|) \right]^2. \quad (5.4.2)$$

and is, thus, very sensitive to the transverse extension *and* opacity of the scattered particles. Equation (5.4.2) reminds of optical diffraction, where  $J(s, |\vec{b}_\perp|)$  describes the distribution of an absorber that causes the diffraction pattern observed for incident plane waves.

In Fig. 5.5, the differential elastic cross section computed for  $pp$  and  $p\bar{p}$  scattering (solid line) is shown as a function of  $|t| = \vec{q}_\perp^2$  at  $\sqrt{s} = 23.5, 30.7, 44.7, 63, 546$ , and 1800 GeV and compared with experimental data (open circles), where the  $pp$  data at  $\sqrt{s} = 23.5, 30.7, 44.7$ , and 63 GeV were measured at the CERN ISR [126], the  $p\bar{p}$  data at  $\sqrt{s} = 546$  GeV at the CERN  $SppS$  [137], and the  $p\bar{p}$  data at  $\sqrt{s} = 1.8$  TeV at the Fermilab Tevatron [138, 139]. The prediction of our model for the  $pp$  differential elastic cross section at the CERN LHC,  $\sqrt{s} = 14$  TeV, is given in Fig. 5.6.

For all energies, the model reproduces the experimentally observed diffraction pattern, i.e the characteristic *diffraction peak* at small  $|t|$  and the *dip* structure at medium  $|t|$ . As the energy increases, also the *shrinking of the diffraction peak* is described which reflects the rise of the slope parameter  $B(s, t = 0)$  already discussed above. The shrinking of the diffraction peak comes along with a dip structure that moves towards smaller values of  $|t|$  as the energy increases. This motion of the dip is also described approximately.

The dip in the theoretical curves reflects a change of sign in the  $T$ -matrix element (2.6.6). As the latter is purely imaginary, it is not surprising that there are deviations from the data in the dip region. Here, the real part is expected to be important [139] which is in the small  $|t|$  region negligible in comparison to the imaginary part.

The difference between the  $pp$  and  $p\bar{p}$  data, a deep dip for  $pp$  but only a bump

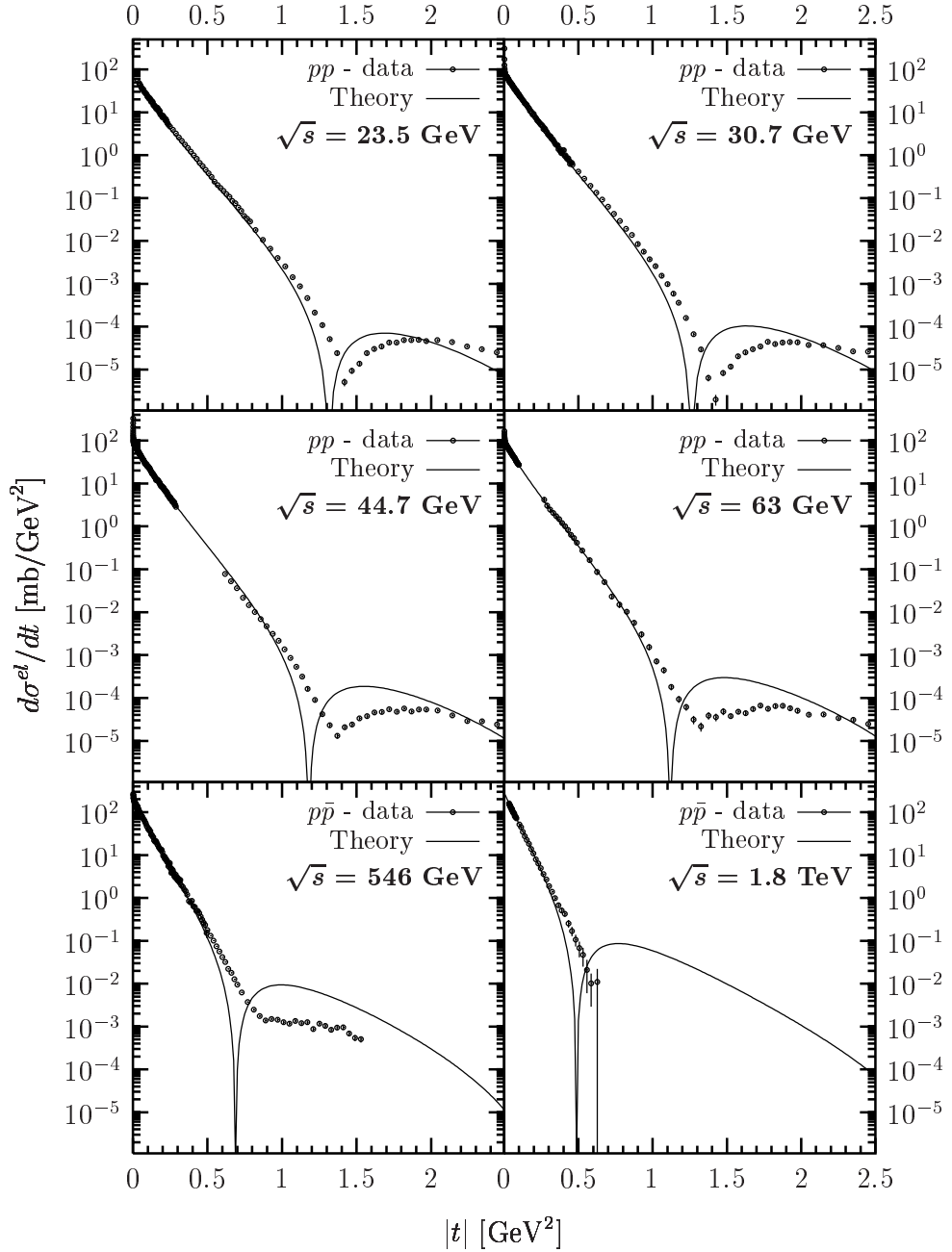


Figure 5.5: The differential elastic cross section for  $pp$  and  $p\bar{p}$  scattering is shown as a function of  $|t|$  up to  $2.5 \text{ GeV}^2$ . The result of our model, indicated by the solid line, is compared for  $\sqrt{s} = 23.5, 30.7, 44.7$ , and  $63 \text{ GeV}$  with the CERN ISR  $pp$  data [126], for  $\sqrt{s} = 546 \text{ GeV}$  with the CERN  $SppS$   $p\bar{p}$  data [137], and for  $\sqrt{s} = 1.8 \text{ TeV}$  with the Fermilab Tevatron  $p\bar{p}$  data [138, 139], all indicated by the open circles with error bars.

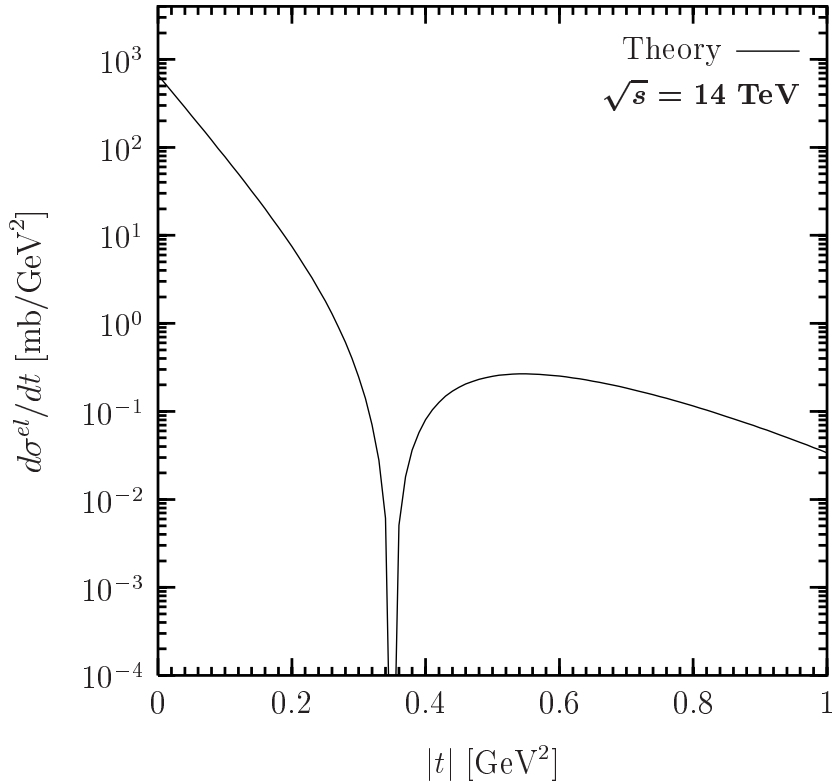


Figure 5.6: The prediction of our model for the  $pp$  differential elastic cross section at LHC ( $\sqrt{s} = 14$  TeV) is shown as a function of momentum transfer  $|t|$  up to  $1\text{ GeV}^2$ .

or shoulder for  $p\bar{p}$  reactions, requires a  $C = -1$  contribution. Besides the reggeon contribution at small energies,<sup>2</sup> one expects here an additional perturbative  $C = -1$  contribution such as three-gluon exchange [140, 141] or an odderon [142–144]. In fact, allowing a finite size diquark in the (anti-)proton an odderon appears that supports the dip in  $pp$  but leads to the shoulder in  $p\bar{p}$  reactions [144].

For the differential elastic cross section at the LHC energy,  $\sqrt{s} = 14$  TeV, the above findings suggest an accurate prediction in the small- $|t|$  region but a dip at a position smaller than the predicted value at  $|t| \approx 0.35\text{ GeV}^2$ . Our confidence in the validity of the model at small  $|t|$  is supported additionally by the total cross section that fixes  $d\sigma^{el}/dt(s, t = 0)$  and is in agreement with the cosmic ray data shown in Fig. 5.1. Concerning our prediction for the dip position, it is close to the value  $|t| \approx 0.41\text{ GeV}^2$  of [124] but significantly below the value  $|t| \approx 0.55\text{ GeV}^2$  of [14]. Beyond the dip position, the height of the computed shoulder is always above the

<sup>2</sup>Zooming in on the result for  $\sqrt{s} = 23.5\text{ GeV}$ , one finds further an underestimation of the data for all  $|t|$  before the dip, which is correct as it leaves room for the reggeon contribution being non-negligible at small energies.

data and, thus, very likely to exceed also the LHC data. In comparison with other works, the height of our shoulder is similar to the one of [124] but almost one order of magnitude above the one of [14].

Considering Figs. 5.5 and 5.6 more quantitatively in the small- $|t|$  region, one can use the well known parametrization of the differential elastic cross section in terms of the slope parameter  $B(s)$  and the *curvature*  $C(s)$

$$d\sigma^{el}/dt(s, t) = d\sigma^{el}/dt(s, t = 0) \exp [B(s)t + C(s)t^2] . \quad (5.4.3)$$

Using  $B(s)$  from the preceding section and assuming for the moment  $C(s) = 0$ , one achieves a good description at small momentum transfers and energies, which is consistent with the approximate Gaussian shape of  $J_{pp}(s, |\vec{b}_\perp|)$  at small energies shown in Fig. 4.1. The dip, of course, is generated by the deviation from the Gaussian shape at small impact parameters. According to (5.4.3), the shrinking of the diffraction peak with increasing energy reflects simply the increasing interaction radius described by  $B(s)$ .

For small energies  $\sqrt{s}$ , our model reproduces the experimentally observed change in the slope at  $|t| \approx 0.25 \text{ GeV}^2$  [145] that is characterized by a positive curvature. For LHC, we find clearly a negative value for the curvature in agreement with [124] but in contrast to [14]. The change of sign in the curvature reflects the transition of  $J(s, |\vec{b}_\perp|)$  from the approximate Gaussian shape at low energies to the approximate step-function shape (5.1.4) at high energies.

Important for the good agreement with the data is the longitudinal quark momentum distribution in the proton. Besides the slope parameter, which characterizes the diffraction peak, also the dip position is very sensitive to the distribution width  $\Delta z_p$ , i.e. with  $\Delta z_p = 0$  the dip position appears at more than 10% lower values of  $|t|$ . In the earlier SVM approach [14], the reproduction of the correct dip position was possible without the  $z$ -dependence of the hadronic wave functions but a deviation from the data in the low- $|t|$  region had to be accepted. In this low- $|t|$  region, we achieved a definite improvement with the new correlation functions (2.4.10) and the minimal surfaces used in our model.

The differential elastic cross section computed for  $\pi^\pm p$  and  $K^\pm p$  reactions has the same behavior as the one for  $pp$  ( $p\bar{p}$ ) reactions. The only difference comes from the different  $z$ -distribution widths,  $\Delta z_\pi$  and  $\Delta z_K$ , and the smaller extension parameters,  $S_\pi$  and  $S_K$ , which shift the dip position to higher values of  $|t|$ . This is illustrated in Fig. 5.7, where the model results (solid line) for the  $\pi^\pm p$  and  $K^\pm p$  differential elastic cross section as a function of  $|t|$  are shown at  $\sqrt{s} = 19.5 \text{ GeV}$  in comparison with experimental data (closed circles) from [146]. The deviations from the data towards large  $|t|$  leave room for odderon and reggeon contributions. Indeed, with a

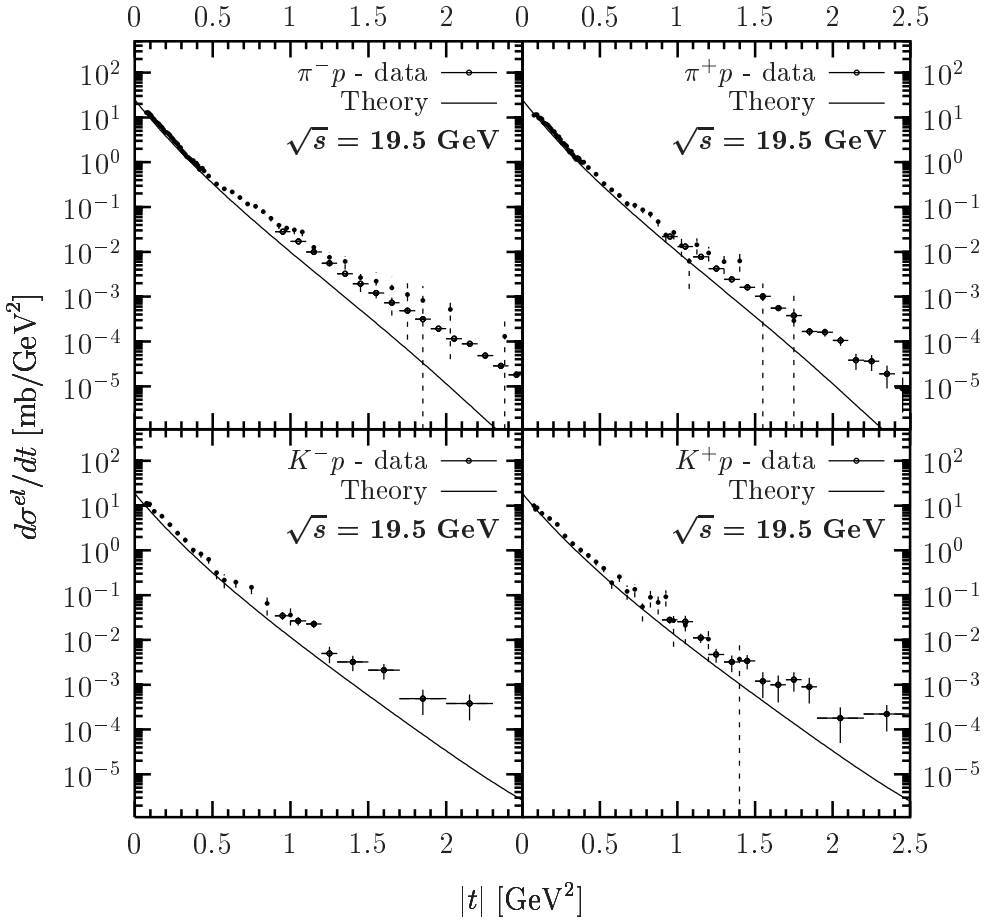


Figure 5.7: The differential elastic cross section  $d\sigma^{el}/dt(s, t)$  is shown versus the momentum transfer  $|t|$  for  $\pi^\pm p$  and  $K^\pm p$  reactions at the c.m. energy  $\sqrt{s} = 19.5$  GeV. The model results (solid line) are compared with the data (closed circles with error bars) from [146].

finite diquark size in the proton, an odderon occurs that improves the description of the data at large values of  $|t|$  [147].

## 5.5 Elastic Cross Sections $\sigma^{el}$ , $\sigma^{el}/\sigma^{tot}$ , and $\sigma^{tot}/B$

The *elastic cross section* obtained by integrating the differential elastic cross section

$$\sigma^{el}(s) = \int_0^{-\infty} dt \frac{d\sigma^{el}}{dt}(s, t) = \int_0^{-\infty} dt \frac{1}{16\pi s^2} |T(s, t)|^2 \quad (5.5.1)$$

reduces for our purely imaginary  $T$ -matrix (2.6.6) to

$$\sigma^{el}(s) = \int d^2 b_\perp |J(s, |\vec{b}_\perp|)|^2. \quad (5.5.2)$$

Due to the squaring, it exhibits the saturation of  $J(s, |\vec{b}_\perp|)$  at the black disc limit more clearly than  $\sigma^{tot}(s)$ . Even more transparent is the saturation in the following ratios given here for a purely imaginary  $T$ -matrix

$$\frac{\sigma^{el}}{\sigma^{tot}}(s) = \frac{\int d^2 b_\perp |J(s, |\vec{b}_\perp|)|^2}{2 \int d^2 b_\perp J(s, |\vec{b}_\perp|)}, \quad (5.5.3)$$

$$\frac{\sigma^{tot}}{B}(s) = \frac{\left(2 \int d^2 b_\perp J(s, |\vec{b}_\perp|)\right)^2}{\int d^2 b_\perp |\vec{b}_\perp|^2 J(s, |\vec{b}_\perp|)}, \quad (5.5.4)$$

which are directly sensitive to the opacity of the particles. This sensitivity can be illustrated within the approximation

$$T(s, t) = i s \sigma^{tot}(s) \exp[B(s)t/2] \quad (5.5.5)$$

that leads to the differential cross section (5.4.3) with  $C(s) = 0$ , i.e. an exponential decrease over  $|t|$  with a slope  $B(s)$ . As the purely imaginary  $T$ -matrix element (5.5.5) is equivalent to

$$J(s, |\vec{b}_\perp|) = (\sigma^{tot}/4\pi B) \exp[-|\vec{b}_\perp|^2/2B] = (4\sigma^{el}/\sigma^{tot}) \exp[-|\vec{b}_\perp|^2/2B], \quad (5.5.6)$$

one finds that the above ratios are a direct measure for the opacity at zero impact parameter

$$J(s, |\vec{b}_\perp| = 0) = (\sigma^{tot}/4\pi B) = (4\sigma^{el}/\sigma^{tot}). \quad (5.5.7)$$

For a general purely imaginary  $T$ -matrix,  $T(s, t) = i s \sigma^{tot} g(|t|)$  with an arbitrary real-valued function  $g(|t|)$ ,  $J(s, |\vec{b}_\perp| = 0)$  is given by  $(\sigma^{el}/\sigma^{tot})$  times a pure number which depends on the shape of  $g(|t|)$ .

We compute the elastic cross section  $\sigma^{el}$  and the ratios  $\sigma^{el}/\sigma^{tot}$  and  $\sigma^{tot}/B$  in our model without taking into account reggeons. In Fig. 5.8, the results for  $pp$  and  $p\bar{p}$  reactions (solid lines) are compared with the experimental data (open and closed circles). The data for the elastic cross section are taken from [3] and the data for  $\sigma^{tot}$  and  $B$  from the references given in previous sections. For  $pp$  ( $p\bar{p}$ ) scattering, we indicate explicitly the prediction for LHC at  $\sqrt{s} = 14$  TeV and the onset of the black disc limit at  $\sqrt{s} = 10^6$  GeV. The model results for  $\pi p$  and  $Kp$  reactions are presented as dashed and dotted line, respectively. For the ratios, the asymptotic limits are indicated: Since the maximum opacity or black disc limit governs the  $\sqrt{s} \rightarrow \infty$  behavior,  $\sigma^{el}/\sigma^{tot}$  ( $\sigma^{tot}/B$ ) cannot exceed 0.5 ( $8\pi$ ) in hadron-hadron scattering.

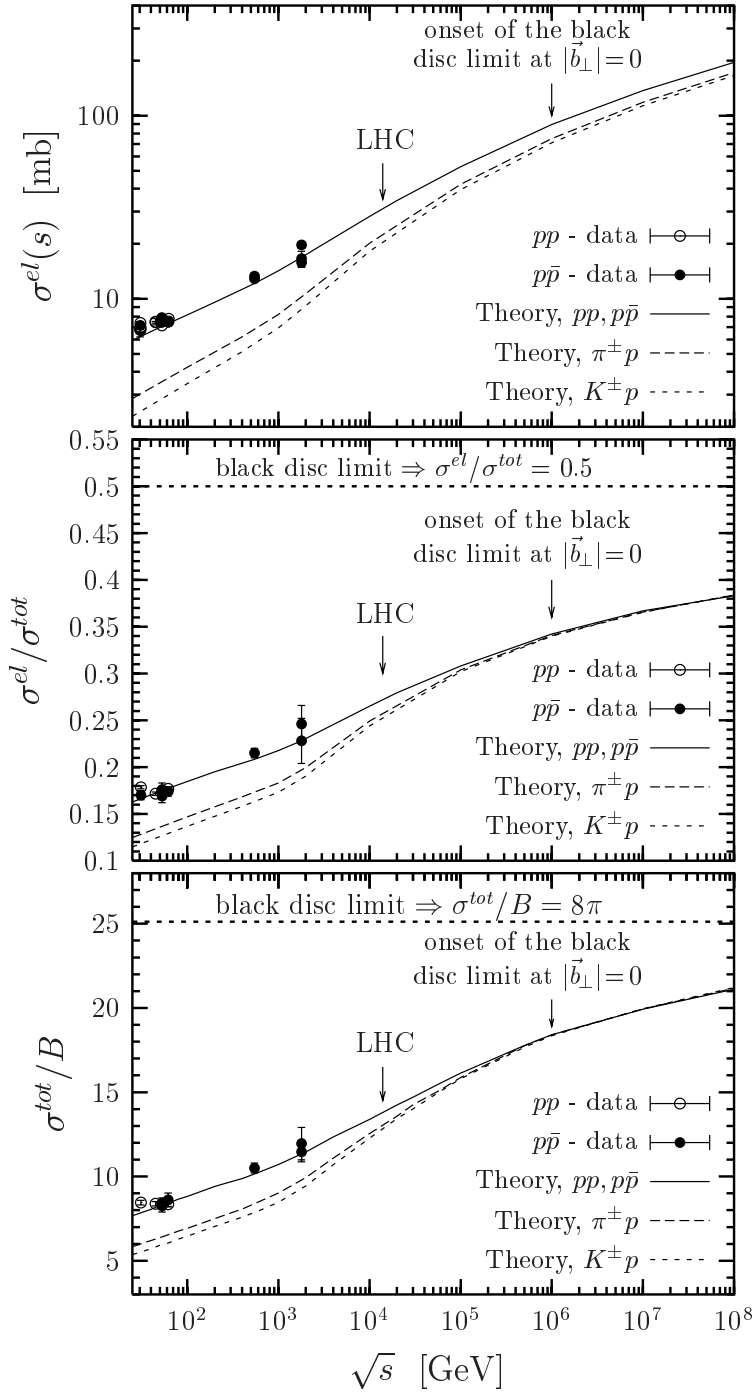


Figure 5.8: The elastic cross section  $\sigma^{el}$  and the ratios  $\sigma^{el}/\sigma^{tot}$  and  $\sigma^{tot}/B$  are shown as a function of the c.m. energy  $\sqrt{s}$ . The model results for  $pp$  ( $p\bar{p}$ ),  $\pi p$ , and  $Kp$  scattering are represented by the solid, dashed and dotted lines, respectively. The experimental data for the  $pp$  and  $p\bar{p}$  reactions are indicated by the open and closed circles, respectively. The data for the elastic cross section are taken from [3] and the data for  $\sigma^{tot}$  and  $B$  from the references given in previous sections.

In the investigation of  $pp$  ( $p\bar{p}$ ) scattering, our theoretical curves confront successfully the experimental data for the elastic cross section and both ratios. At low energies, the data are underestimated as reggeon contributions are not taken into account. Again, the agreement is comparable to the one achieved in [124] and better than in the approach of [14], where  $\sigma^{el}$  comes out too small due to an underestimation of  $d\sigma^{el}/dt$  in the low- $|t|$  region.

Concerning the energy dependence,  $\sigma^{el}$  shows a similar behavior as  $\sigma^{tot}$  but with a more pronounced flattening around  $\sqrt{s} \gtrsim 10^6$  GeV. This flattening is even stronger for the ratios, drawn on a linear scale, and reflects very clearly the onset of the black disc limit. As expected from the simple approximation (5.5.7),  $\sigma^{el}/\sigma^{tot}$  and  $\sigma^{tot}/B$  show a similar functional dependence on  $\sqrt{s}$ . At the highest energy shown,  $\sqrt{s} = 10^8$  GeV, both ratios are still below the indicated asymptotic limits, which reflects that  $J(s, |\vec{b}_\perp|)$  still deviates from the step-function shape (5.1.4). The ratios  $\sigma^{el}/\sigma^{tot}$  and  $\sigma^{tot}/B$  reach their upper limits 0.5 and  $8\pi$ , respectively, at asymptotic energies,  $\sqrt{s} \rightarrow \infty$ , where the hadrons become infinitely large, completely black discs.

In comparision to the  $pp$  ( $p\bar{p}$ ) result for  $\sigma^{el}$ , the  $\pi p$  and  $Kp$  elastic cross sections are smaller due to the smaller pion and kaon sizes or the corresponding narrower profile functions shown in Fig. 4.1. For  $pp$  ( $p\bar{p}$ ),  $\pi p$ , and  $Kp$  scattering, the ratios  $\sigma^{el}/\sigma^{tot}$  and  $\sigma^{tot}/B$  representing the opacity of the interacting hadrons in their center (cf. Fig. 4.1 at  $|\vec{b}_\perp| = 0$ ) converge for  $\sqrt{s} \geq 10^6$  GeV as shown in Fig. 5.8. This follows from the identical normalizations of the hadron wave functions that lead to an identical black disc limit for hadron-hadron reactions approached in the center of the hadrons at  $\sqrt{s} \approx 10^6$  GeV.

# Chapter 6

## Conclusions and Outlook

We have developed a model that combines perturbative and non-perturbative QCD to compute high-energy reactions of hadrons and photons. We have investigated the QCD structure of non-perturbative interactions in momentum space. A decomposition of the QCD string into stringless dipoles has been found, confinement effects have been shown explicitly in high-energy scattering and a microscopic structure of unintegrated gluon distributions of hadrons and photons has been obtained. Saturation effects that manifest the unitarity of the  $S$ -matrix have been studied in impact parameter space of the scattering amplitude. We have displayed explicitly the saturation of the impact parameter profiles for proton-proton and photon-proton scattering at the black disc limit at high c.m. energies. The impact parameter dependent gluon distribution of the proton is found to saturate at small Bjorken  $x$ . We have compared the model results for  $pp$ ,  $\pi p$ ,  $Kp$ ,  $\gamma^* p$  and  $\gamma\gamma$  reactions with experimental data and have shown saturation effects in experimental observables.

The simplicity of minimal surfaces introduced in our model has allowed us to show for the first time the QCD structure of the non-perturbative dipole-dipole interaction in momentum space. This contribution divides into two parts: The first part describes the non-perturbative interaction between the quarks and antiquarks of the two dipoles and exhibits the structure known from perturbative two-gluon exchange [34, 35]. The second part describes the interaction between the strings of the two dipoles and has a new structure originating from the geometry of the strings.

The contribution of the confining string to the total dipole-hadron cross section  $\sigma_{Dh}(x, |\vec{r}_D|)$  has been studied. For small dipole sizes,  $|\vec{r}_D| \rightarrow 0$ , the string contribution shows color transparency,  $\sigma_{Dh}(x, |\vec{r}_D|) \propto r_D^2$ , as known for the perturbative contribution. For large dipole sizes,  $|\vec{r}_D| \gtrsim 0.5$  fm, the non-perturbative contribution increases linearly with increasing dipole size,  $\sigma_{Dh}(x, |\vec{r}_D|) \propto |\vec{r}_D|$ , in contrast to

the perturbative contribution which gives an  $|\vec{r}_D|$ -independent dipole-hadron cross section. This linear increase is generated by the interaction of the string of the dipole with the hadron: the longer the string, the larger the geometric cross section with the hadron. String breaking, expected to stop the linear increase for  $|\vec{r}_D| \gtrsim 1$  fm, is excluded in our model that works in the quenched approximation. The  $|\vec{k}_\perp|$ -factorization, known in perturbative physics, has been found to be valid also for the non-perturbative dipole-hadron interaction.

The most outstanding result of this work is the following feature of the QCD string that confines the quark and antiquark in the dipole: The QCD string of length  $|\vec{r}_D|$  can be exactly represented as an integral over stringless dipoles of sizes  $\xi|\vec{r}_D|$  with  $0 \leq \xi \leq 1$  and dipole number density  $n(\xi) = 1/\xi^2$ . A similar behavior has been observed for the perturbatively computed wave function of a  $q\bar{q}$  onium state in the large- $N_c$  limit where the numerous emitted gluons inside the onium state represent dipoles [36, 37]. The decomposition of the string into stringless dipoles has allowed us to rewrite the string-hadron scattering process as an incoherent superposition of dipole-hadron scattering processes and to extract the unintegrated gluon distribution of hadrons and photons, respectively, from our dipole-hadron and dipole-photon cross section via  $|\vec{k}_\perp|$ -factorization.

We have shown explicitly the microscopic structure of the unintegrated gluon distribution in hadrons and photons. For small momenta  $|\vec{k}_\perp|$ , the unintegrated gluon distributions of hadrons  $\mathcal{F}_h(x, k_\perp^2)$  are dominated by non-perturbative physics and behave as  $S_h^2/|\vec{k}_\perp|$  where  $S_h$  denotes the hadron extension. The  $1/|\vec{k}_\perp|$ -behavior is a string manifestation as it originates from the linear increase of the total dipole-hadron cross section at large dipole sizes. For large momenta,  $|\vec{k}_\perp| \gtrsim 1$  GeV, the unintegrated gluon distributions of the hadrons are dominated by perturbative physics and show the  $1/k_\perp^2$ -behavior induced by the gluon propagator. In the perturbative region of large momenta the valence constituents are resolved and the dependence of the unintegrated gluon distribution on the hadron extension  $S_h$  vanishes. In contrast, the unintegrated gluon distribution of photons depends on the “photon size” for large  $|\vec{k}_\perp|$  because of the  $Q^2$ -dependent normalization of photon wave functions.

The  $x$ -dependence of the unintegrated gluon distribution of hadrons and photons has been introduced phenomenologically into our model. Motivated by experimental observations, we have given a strong energy dependence to the perturbative contribution and a weak one to the non-perturbative contribution. Consequently, with decreasing  $x$  the perturbative contribution increases much stronger than the non-perturbative contribution and extends into the small- $|\vec{k}_\perp|$  region. A similar hard-to-soft diffusion is seen also in the approach of Ivanov and Nikolaev [85] while a soft-to-hard diffusion is obtained in the approach of the color glass condensate [86]. Considering the integrated gluon distribution of the proton  $xG_p(x, Q^2)$ , our non-

perturbative contribution dominates for  $x \gtrsim 10^{-3}$  while the perturbative contribution becomes relevant for  $x \lesssim 10^{-3}$  and generates the steep increase of  $xG_p(x, Q^2)$  with decreasing  $x$  at fixed  $Q^2$ . Also the rise of  $xG_p(x, Q^2)$  with increasing  $Q^2$  at fixed  $x$  results from the strong energy dependence of the perturbative contribution.

We have compared the unintegrated gluon distribution of the proton  $\mathcal{F}_p(x, k_\perp^2)$  extracted from our loop-loop correlation model (LLCM) with those obtained from the saturation model of Golec-Biernat and Wüsthoff (GBW) [72], the derivative of the Glück, Reya, and Vogt (GRV) parametrization of  $xG_p(x, Q^2)$  [87], and the approach of Ivanov and Nikolaev (IN) [85]. For  $k_\perp^2 \rightarrow 0$ , the unintegrated gluon distribution of GBW decreases as  $k_\perp^2$  and the one of IN as  $k_\perp^4$  in contrast to the  $1/\sqrt{k_\perp^2}$ -decrease found in our model. In the perturbative region, the LLCM, GRV, and IN unintegrated gluon distributions become parallel for  $x \lesssim 10^{-2}$  and drop as  $1/k_\perp^2$  with increasing  $k_\perp^2$ . This perturbative QCD behavior is not reproduced by the GBW unintegrated gluon distribution which decreases exponentially with increasing  $k_\perp^2$ . The  $x$ -dependence of the considered unintegrated gluon distributions is weak in the non-perturbative region and becomes stronger as  $k_\perp^2$  increases.

We have studied saturation effects of the scattering amplitude in impact parameter space. The impact parameter profiles have been found to respect the black disc limit which is imposed by the  $S$ -matrix unitarity. We have computed the impact parameter profiles for hadron-hadron and longitudinal photon-proton scattering. They have shown the following behavior for the evolution of the opacity and size of the interaction particles with increasing energy: The particles become larger and blacker as the energy increases. At energies beyond the black disc limit, the opacity saturates while the expansion of the scattered particles continues. The absolute value of the black disc limit and the energy at which it is reached depend on the normalization of the wave functions and the size of the interacting particles, respectively. For asymptotic energies a universal result is obtained: the size of each particle increases logarithmically with energy as required to guarantee the Froissart bound [7].

We have estimated the impact parameter dependent gluon distribution of the proton  $xG(x, Q^2, |\vec{b}_\perp|)$ . We have shown a low- $x$  saturation of  $xG(x, Q^2, |\vec{b}_\perp|)$  as a manifestation of the  $S$ -matrix unitarity realized by multiple gluonic interactions. The gluon density is found to decrease from the center towards the periphery of the proton. The saturation value and the increase of  $xG(x, Q^2, |\vec{b}_\perp| = 0)$  towards small  $x$  depend on the photon virtuality  $Q^2$ . In contrast, at fixed  $Q^2$ , the integrated gluon distribution  $xG(x, Q^2)$  does not saturate because of the growing proton radius with decreasing  $x$ . In agreement with other investigations of gluon saturation [108, 111, 112], we have found a slow down of  $xG(x, Q^2)$  from a powerlike to a squared logarithmic rise for Bjorken  $x$  values beyond the black disc limit in  $xG(x, Q^2, |\vec{b}_\perp|)$ .

The energies at which the saturation effects set in are model dependent. In our approach the impact parameter profiles saturate the black disc limit at zero impact parameter for  $\sqrt{s} \gtrsim 10^6$  GeV in proton-proton scattering and for  $\sqrt{s} \gtrsim 10^7$  GeV in longitudinal photon-proton scattering when  $Q^2 \gtrsim 1$  GeV $^2$ . The saturation of  $xG(x, Q^2, |\vec{b}_\perp|)$  occurs in our approach for  $Q^2 \gtrsim 1$  GeV $^2$  at values of  $x \lesssim 10^{-10}$  which is far below the HERA and THERA range. Munier et al. [114] have also claimed that the black disc limit is not reached in the energy range of HERA.

We have computed total cross sections  $\sigma^{tot}$  for proton-proton, pion-proton, kaon-proton, photon-proton, and photon-photon reactions. A stronger energy rise of total cross sections has been obtained going from large to small-size particles involved in the interaction. This comes, of course, from the strong energy dependence of the perturbative component that becomes increasingly important with decreasing particle sizes. The growth of the total cross sections becomes weaker for c.m. energies  $\sqrt{s} \gtrsim 10^6$  GeV due to the onset of the black disc limit at  $|\vec{b}_\perp| = 0$  in the profile functions. In fact, a transition from a powerlike to an  $\ln^2(s)$ -increase of total cross sections of hadrons and photons is found to set in at  $\sqrt{s} \approx 10^6$  GeV. For asymptotic energies, the total hadronic cross sections become universal, i.e., independent of the hadron species considered, and increase in agreement with the Froissart bound [7]. We predict for proton-proton scattering at LHC ( $\sqrt{s} = 14$  TeV) a total cross section of  $\sigma_{pp}^{tot} = 114.2$  mb which is in good agreement with the cosmic ray data.

For differential elastic cross sections  $d\sigma^{el}/dt$  of proton-proton, pion-proton and kaon-proton scattering, the diffraction pattern and also the shrinkage of the diffraction peak with increasing energy has been shown in good agreement with experimental data at small momentum transfers  $|t|$ . Around the dip region, where a real part is expected to be important, deviations from the data have reflected that our  $T$ -matrix is purely imaginary. The smaller size of the pion and kaon as compared to the proton has become visible in the shift of the dip towards larger values of  $|t|$  in the differential elastic cross sections. A differential elastic cross section with a negative curvature,  $C < 0$ , and a dip at  $|t| \approx 0.35$  GeV $^2$  is predicted for LHC. The total elastic cross section, obtained by integrating the differential elastic cross section over the momentum transfer  $|t|$ , has shown similar features as the total hadronic cross section discussed above. It takes a value of  $\sigma^{el} \approx 30$  mb at the LHC energy.

We have also studied the slope parameter  $B(s)$  of the forward differential elastic cross section for proton-proton scattering and the ratios  $\sigma^{el}/\sigma^{tot}$  and  $\sigma^{tot}/B$  for proton-proton, pion-proton and kaon-proton reactions. The slope parameter and the ratios are a measure of the squared hadron extension and hadron opacity, respectively. We have found an  $\ln^2(s)$ -increase for the slope parameter at large c.m. energies. The ratios have shown a universal behavior already for c.m. energies  $\sqrt{s} \geq 10^6$  GeV. This behavior reflects most explicitly the saturation of the impact

parameter profiles at the black disc limit. The slope parameter at LHC is predicted to be  $B = 21.26 \text{ GeV}^{-2}$ .

The mentioned observables, namely, total cross sections, the structure function of the proton, slope parameters, differential elastic cross sections, elastic cross sections and the ratios  $\sigma^{el}/\sigma^{tot}$  and  $\sigma^{tot}/B$  for proton-proton, pion-proton, kaon-proton, photon-proton, and photon-photon reactions are in good agreement with experimental data over a wide c.m. energy range. We have provided a unified description of these reactions using a universal mechanism for the interaction and energy dependence. This mechanism seems to be appropriate and required by experimental data.

In spite of the success of our combined perturbative and non-perturbative QCD approach to high-energy scattering, there are still several shortcomings and limitations of our model in its present form that leave room for future improvements:

- Our approach does not generate energy dependent cross sections because of the missed gluon radiation. Thus, for a fundamental understanding of the energy dependence of high-energy reactions one has to implement quantum evolution in our model analogous to complementary approaches [75]. Attempts aiming at a description of high-energy scattering from the QCD Lagrangian have been recently reported: In [148] structure functions of deep inelastic scattering at small Bjorken  $x$  are related to an effective Euclidean field theory. Here one hopes that the limit  $x \rightarrow 0$  corresponds to critical behavior in the effective theory. In another recent formalism, the energy dependence of the proton structure function has been related successfully to critical properties of an effective near light-cone Hamiltonian in a non-perturbative lattice approach [149].
- Our model works in the quenched approximation since dynamical fermion production is neglected. In addition also gluon vacuum polarization is missed. These shortcomings, of course, exclude string breaking in color-dipoles in the fundamental and adjoint representation, respectively. To be consistent with lattice QCD simulations [26, 80], dynamical fermion and gluon production have to be introduced. Suggestions along these lines can be found in [11].
- The Gaussian approximation of the functional integrals leads to a dependence of cross sections on the choice of the surface that is bounded the Wegner-Wilson loops. It is a challenge to find the right surface that is favored by the Gaussian approximation. There are several indications supporting the minimal surfaces used in this work. Nevertheless, the minimal surfaces are not chosen by a variational principle and are not dynamical. Interpreting the surfaces as the worldsheets of the QCD strings, this means that our model can neither describe quantum fluctuations or excitations of the string nor string flips be-

tween two interacting color-dipoles. Accordingly, our model cannot reproduce the Lüscher term (excitation of the string) in the static quark-antiquark potential recently confirmed on the lattice [68]. Interesting new developments towards a dynamical surface choice and a theory for the dynamics of the confining strings can be found in [54].

- Our ansatz for the gluon field strength correlator does not include explicitly the dependence on the path connecting the two gluon field strengths which has been recently measured on the lattice [55]. In addition, the non-perturbative correlator, being appropriate to describe the scattering between large-size particles, overestimates the scattering between small-size particles as shown in deep inelastic scattering at high photon virtualities. Moreover, our decomposition of the correlator into a perturbative plus a non-perturbative component is not mandatory. Here it is not clear how to reconcile non-perturbative correlations with perturbative gluon exchange. Methods complementary to our simple two component ansatz can be found in [49, 52–54].
- The static limit of our model becomes most explicit in the computation of the QCD van der Waals interaction between two static color-dipoles. A wrong result for the van der Waals potential is obtained from our model because of the energy degeneracy between the intermediate octet states and the initial (final) singlet states in the static limit. For a meaningful investigation of QCD van der Waals forces within our model, one has to go beyond the static limit and to describe the limited lifetime of the intermediate octet states appropriately.

Several other applications and extensions of the model can be investigated in the future. The two most natural continuations of this work would be

- to compute the vector meson production. Some work in this direction has already been done.
- to generalize our model from two to many particle interactions, i.e. from the present particle-particle to particle-nucleus or nucleus-nucleus interactions. This would mean an extension of the model from the loop-loop correlation  $\langle W_{r_1}[C_1]W_{r_2}[C_2] \rangle$  to multiple loop correlations  $\langle W_{r_1}[C_1] \cdots W_{r_n}[C_n] \rangle$ . There are already some first attempts in this direction.

# Appendix A

## Conventions

For completeness the notational conventions used in this work are listed below.

### A.1 Units

We work in natural units,

$$\hbar = c = 1 . \quad (\text{A.1.1})$$

The conversion constant reads  $\hbar c = 197.32705 \text{ MeV fm}$ .

### A.2 Lorentz Vectors

Following the notations of the textbooks [150, 151], we write the contravariant position four-vector  $x^\mu$  in its instant form

$$x^\mu = (x^0, x^1, x^2, x^3) = (t, x, y, z) = (x^0, \vec{x}_\perp, x^3) = (x^0, \vec{x}). \quad (\text{A.2.1})$$

The covariant position four-vector

$$x_\mu = g_{\mu\nu} x^\nu = (x_0, x_1, x_2, x_3) = (t, -x, -y, -z) \quad (\text{A.2.2})$$

is obtained from the contravariant vector by the metric tensor

$$g_{\mu\nu} = g^{\mu\nu} = \begin{pmatrix} +1 & 0 & 0 & 0 \\ 0 & -1 & 0 & 0 \\ 0 & 0 & -1 & 0 \\ 0 & 0 & 0 & -1 \end{pmatrix} . \quad (\text{A.2.3})$$

Of course, implicit summation over repeated Lorentz indices is understood. The scalar product of  $x^\mu$  with four-momentum  $p^\mu = (p^0, p^1, p^2, p^3) = (E, \vec{p})$  is

$$x \cdot p = x^\mu p_\mu = x^0 p_0 + x^1 p_1 + x^2 p_2 + x^3 p_3 = tE - \vec{x} \cdot \vec{p}. \quad (\text{A.2.4})$$

### A.3 Light-Cone Coordinates

For the light-cone coordinates, we employ the convention that has been used by Lepage and Brodsky [152] and write the contravariant position four-vector as

$$x^\mu = (x^+, x^-, x^1, x^2) = (x^+, x^-, \vec{x}_\perp) \quad (\text{A.3.1})$$

with time-like ('light-cone time') and space-like ('light-cone position') components

$$x^+ = x^0 + x^3 \quad \text{and} \quad x^- = x^0 - x^3, \quad (\text{A.3.2})$$

respectively. The covariant position four-vector is again obtained by lowering the indices with the metric tensor,  $x_\mu = g_{\mu\nu}x^\nu$ , that has the following form in the Lepage-Brodsky light-cone coordinates

$$g^{\mu\nu} = \begin{pmatrix} 0 & 2 & 0 & 0 \\ 2 & 0 & 0 & 0 \\ 0 & 0 & -1 & 0 \\ 0 & 0 & 0 & -1 \end{pmatrix} \quad \text{and} \quad g_{\mu\nu} = \begin{pmatrix} 0 & \frac{1}{2} & 0 & 0 \\ \frac{1}{2} & 0 & 0 & 0 \\ 0 & 0 & -1 & 0 \\ 0 & 0 & 0 & -1 \end{pmatrix}. \quad (\text{A.3.3})$$

This form was required by the Lorentz-invariance of the scalar product. The scalar product of the position four-vector with the momentum four-vector is written as

$$x \cdot p = x^\mu p_\mu = x^+ p_+ + x^- p_- + x^1 p_1 + x^2 p_2 = \frac{1}{2}(x^+ p^- + x^- p^+) - \vec{x}_\perp \vec{p}_\perp. \quad (\text{A.3.4})$$

The measure for a four-dimensional space-time integration,  $d^4x$ , expressed in light-cone coordinates reads

$$d^4x = dx^0 dx^1 dx^2 dx^3 = \frac{1}{2} dx^+ dx^- d^2 x_\perp. \quad (\text{A.3.5})$$

# Appendix B

## Wave Functions

The light-cone wave functions  $\psi_i(z_i, \vec{r}_i)$  provide the distribution of transverse size and orientation  $\vec{r}_i$  and longitudinal quark momentum fraction  $z_i$  to the light-like Wegner-Wilson loops  $W[C_i]$  that represent the scattering color-dipoles. In this way, they specify the projectiles as mesons, baryons described as quark-diquark systems, or photons that fluctuate into a quark-antiquark pair before the interaction.

### B.1 Hadron Wave Function

In this work mesons and baryons are assumed to have a quark-antiquark and quark-diquark valence structure, respectively. As quark-diquark systems are equivalent to quark-antiquark systems [153], this allows us to model not only mesons but also baryons as color-dipoles represented by Wegner-Wilson loops. We use for the hadron wave function the phenomenological Gaussian Wirbel-Stech-Bauer ansatz [44]

$$\psi_h(z_i, \vec{r}_i) = \sqrt{\frac{z_i(1-z_i)}{2\pi S_h^2 N_h}} e^{-(z_i - \frac{1}{2})^2/(4\Delta z_h^2)} e^{-|\vec{r}_i|^2/(4S_h^2)}, \quad (\text{B.1.1})$$

where the hadron wave function normalization to unity

$$\int dz_i d^2 r_i |\psi_i(z_i, \vec{r}_i)|^2 = 1, \quad (\text{B.1.2})$$

requires the normalization constant

$$N_h = \int_0^1 dz_i z_i(1-z_i) e^{-(z_i - \frac{1}{2})^2/(2\Delta z_h^2)}. \quad (\text{B.1.3})$$

Table B.1: Hadron Parameters

Hadron	$\Delta z_h$	$S_h$ [fm]
$p, \bar{p}$	0.3	0.86
$\pi^\pm$	2	0.607
$K^\pm$	0.57	0.55

The different hadrons considered — protons, pions, and kaons — are specified by  $\Delta z_h$  and  $S_h$  providing the width for the distributions of the longitudinal momentum fraction carried by the quark  $z_i$  and transverse spatial extension  $|\vec{r}_i|$ , respectively. In this work the extension parameter  $S_h$  is a fit parameter that should resemble approximately the electromagnetic radius of the corresponding hadron [23], while  $\Delta z_h = w/(\sqrt{2} m_h)$  [44] is fixed by the hadron mass  $m_h$  and the value  $w = 0.35 - 0.5$  GeV extracted from experimental data. We find for (anti-)protons  $\Delta z_p = 0.3$  and  $S_p = 0.86$  fm, for pions  $\Delta z_\pi = 2$  and  $S_\pi = 0.607$  fm, and for kaons  $\Delta z_K = 0.57$  and  $S_K = 0.55$  fm which are the values used in the main text. For convenience they are summarized in Table B.1.

Concerning the quark-diquark structure of the baryons, the more conventional three-quark structure of a baryon would complicate the model significantly but would lead to similar predictions once the model parameters are readjusted [13]. In fact, there are also physical arguments that favor the quark-diquark structure of the baryon such as the  $\delta I = 1/2$  enhancement in semi-leptonic decays of baryons [153] and the strong attraction in the scalar diquark channel in the instanton vacuum [154].

## B.2 Photon Wave Function

The photon wave function  $\psi_\gamma(z_i, \vec{r}_i, Q^2)$  describes the fluctuation of a photon with virtuality  $Q^2$  into a quark-antiquark pair with longitudinal quark momentum fraction  $z_i$  and spatial transverse size and orientation  $\vec{r}_i$ . The computation of the corresponding transition amplitude  $\langle q\bar{q}(z_i, \vec{r}_i) | \gamma^*(Q^2) \rangle$  can be performed conveniently in light-cone perturbation theory [155] and leads to the following squared wave functions for transverse ( $T$ ) and longitudinally ( $L$ ) polarized photons [69]

$$|\psi_{\gamma_T^*}(z_i, \vec{r}_i, Q^2)|^2 = \frac{3\alpha}{2\pi^2} \sum_f e_f^2 \{ [z_i^2 + (1-z_i)^2] \epsilon_f^2 K_1^2(\epsilon_f |\vec{r}_i|) + m_f^2 K_0^2(\epsilon_f |\vec{r}_i|) \} \quad (\text{B.2.1})$$

$$|\psi_{\gamma_L^*}(z_i, \vec{r}_i, Q^2)|^2 = \frac{3\alpha}{2\pi^2} \sum_f e_f^2 \left\{ 4Q^2 z_i^2 (1-z_i)^2 K_0^2(\epsilon_f |\vec{r}_i|) \right\}, \quad (\text{B.2.2})$$

where  $\alpha$  is the fine-structure constant,  $e_f$  is the electric charge of the quark with flavor  $f$ , and  $K_0$  and  $K_1$  are the modified Bessel functions (McDonald functions). In the above expressions,

$$\epsilon_f^2 = z_i(1-z_i)Q^2 + m_f^2 \quad (\text{B.2.3})$$

controls the transverse size(-distribution) of the emerging dipole,  $|\vec{r}_i| \propto 1/\epsilon_f$ , that depends on the quark flavor through the current quark mass  $m_f$ .

For small  $Q^2$ , the perturbatively derived wave functions, (B.2.1) and (B.2.2), are not appropriate since the resulting large color-dipoles, i.e.  $|\vec{r}_i| \propto 1/m_f \gg 1 \text{ fm}$ , should encounter non-perturbative effects such as confinement and chiral symmetry breaking. To take these effects into account the vector meson dominance (VMD) model [156] is usually used. However, the transition from the “partonic” behavior at large  $Q^2$  to the “hadronic” one at small  $Q^2$  can be modelled as well by introducing  $Q^2$ -dependent quark masses,  $m_f = m_f(Q^2)$ , that interpolate between the current quarks at large  $Q^2$  and the constituent quarks at small  $Q^2$  [20]. Following this approach, we use (B.2.1) and (B.2.2) also in the low- $Q^2$  region but with the running quark masses

$$m_{u,d}(Q^2) = 0.178 \text{ GeV} \left( 1 - \frac{Q^2}{Q_{u,d}^2} \right) \Theta(Q_{u,d}^2 - Q^2), \quad (\text{B.2.4})$$

$$m_s(Q^2) = 0.121 \text{ GeV} + 0.129 \text{ GeV} \left( 1 - \frac{Q^2}{Q_s^2} \right) \Theta(Q_s^2 - Q^2), \quad (\text{B.2.5})$$

and the fixed charm quark mass

$$m_c = 1.25 \text{ GeV}, \quad (\text{B.2.6})$$

where the parameters  $Q_{u,d}^2 = 1.05 \text{ GeV}^2$  and  $Q_s^2 = 1.6 \text{ GeV}^2$  are taken directly from [20] while we reduced the values for the constituent quark masses  $m_f(Q^2 = 0)$  of [20] by about 20%. The smaller constituent quark masses are necessary in order to reproduce the total cross sections for  $\gamma^* p$  and  $\gamma^* \gamma^*$  reactions at low  $Q^2$ . Similar running quark masses are obtained in a QCD-motivated model of the spontaneous chiral symmetry breaking in the instanton vacuum [157] that improve the description of  $\gamma^* p$  scattering at low  $Q^2$  [158].



# Appendix C

## Correlation Functions

In this appendix we describe explicitly the way from the simple exponential correlation functions in Euclidean space-time (2.4.10) to their transverse Fourier transforms in Minkowski space-time, (2.5.11) and (2.5.16). The first step in this procedure is the Fourier transformation of the exponential correlation functions (2.4.10) in four-dimensional Euclidean space-time

$$\begin{aligned}
\tilde{D}^E(K^2) &= \tilde{D}_1^E(K^2) = \int d^4Z D^E(Z^2/a^2) e^{iKZ} \\
&= \int_0^\infty d|Z| |Z|^3 \int_0^\pi d\phi_3 \sin^2\phi_3 \int_0^\pi d\phi_2 \sin\phi_2 \int_0^{2\pi} d\phi_1 D^E(Z^2/a^2) e^{-i|K||Z|\cos\phi_3} \\
&= \frac{4\pi^2}{|K|} \int_0^\infty d|Z| |Z|^2 D^E(Z^2/a^2) J_1(|K||Z|) = \frac{12\pi^2}{a(K^2 + a^{-2})^{\frac{5}{2}}} , \quad (\text{C.0.1})
\end{aligned}$$

where  $J_1$  is the 1st order Bessel function of the first kind. Here the Euclidean metric  $-\delta_{\mu\nu}$  and four-dimensional polar coordinates and the corresponding four-volume element  $d^4Z = d|Z| |Z|^3 d\phi_3 \sin^2\phi_3 d\phi_2 \sin\phi_2 d\phi_1$  have been used. With (C.0.1), one obtains

$$\tilde{D}'_1^E(K^2) := \frac{d}{dK^2} \tilde{D}_1^E(K^2) = -\frac{30\pi^2}{a(K^2 + a^{-2})^{\frac{7}{2}}} . \quad (\text{C.0.2})$$

Now, (C.0.1) and (C.0.2) are analytically continued to Minkowski space-time,  $K_4 \rightarrow ik^0$  or equivalently  $-\delta_{\mu\nu} \rightarrow g_{\mu\nu} = \text{diag}(1, -1, -1, -1)$ ,

$$\tilde{D}(k^2) = -\frac{12\pi^2 i}{a(-k^2 + a^{-2})^{\frac{5}{2}}} , \quad \tilde{D}'_1(k^2) = -\frac{30\pi^2 i}{a(-k^2 + a^{-2})^{\frac{7}{2}}} . \quad (\text{C.0.3})$$

Setting  $k^0 = k^3 = 0$ , which is enforced in the computation of  $\chi$  by  $\delta$ -functions, one finds  $k^2 = -\vec{k}_\perp^2$  and consequently

$$\tilde{D}^{(2)}(\vec{k}_\perp^2) = -\frac{12\pi^2 i}{a(\vec{k}_\perp^2 + a^{-2})^{\frac{5}{2}}}, \quad \tilde{D}'^{(2)}_1(\vec{k}_\perp^2) = -\frac{30\pi^2 i}{a(\vec{k}_\perp^2 + a^{-2})^{\frac{7}{2}}}. \quad (\text{C.0.4})$$

The transverse Fourier transformation (2.5.9) of these two expressions is the remaining step that leads directly to (2.5.11) and (2.5.16).

# Appendix D

## Non-Forward $T$ -Matrix Element

In this appendix we calculate the perturbative and non-confining contribution to the non-forward ( $t \neq 0$ )  $T$ -matrix element. We show explicitly that the non-forward  $T$ -matrix element depends on the parameters which control the  $z_i$ -distribution of the wave functions. These parameter are essential for a good description of differential elastic cross sections and the slope parameter as shown in Chapter 5.

The confining contribution to the non-forward ( $t \neq 0$ )  $T$ -matrix element is not presented. It is much more complicated since some of the integrations cannot be performed analytically. Nevertheless, we find numerically that it shows the same features concerning the  $z_i$ -distributions as the perturbative and non-confining contributions.

The perturbative contribution to the non-forward  $T$ -matrix element in the small- $\chi$  limit (2.6.3),

$$T^P(s_0, t) = \frac{2is_0}{9} \int d^2 b_\perp e^{i\vec{q}_\perp \vec{b}_\perp} \int dz_1 d^2 r_1 \int dz_2 d^2 r_2 |\psi_1(z_1, \vec{r}_1)|^2 |\psi_2(z_2, \vec{r}_2)|^2 (\chi^P)^2 , \quad (\text{D.0.1})$$

reduces upon integration over the impact parameter  $|\vec{b}_\perp|$  to

$$\begin{aligned} T^P(s_0, t) &= \frac{32is_0}{9} \int d^2 k_\perp \alpha_s(k_\perp^2) i\tilde{D}'_P^{(2)}(k_\perp^2) \alpha_s((\vec{k}_\perp + \vec{q}_\perp)^2) i\tilde{D}'_P^{(2)}((\vec{k}_\perp + \vec{q}_\perp)^2) \\ &\times \int_0^1 dz_1 \int_0^1 dz_2 \left[ H_1(z_1^2 q_\perp^2) - H_1((z_1 \vec{q}_\perp + \vec{k}_\perp)^2) \right] \left[ H_2(z_2^2 q_\perp^2) - H_2((z_2 \vec{q}_\perp + \vec{k}_\perp)^2) \right] \end{aligned} \quad (\text{D.0.2})$$

with

$$H_i((z_i \vec{q}_\perp + \vec{k}_\perp)) := \int d^2 r_i |\psi_i(z_i, \vec{r}_i)|^2 e^{i\vec{r}_i(z_i \vec{q}_\perp + \vec{k}_\perp)} . \quad (\text{D.0.3})$$

and  $|\psi_i(z_i, \vec{r}_i)|^2$  denoting hadron or photon wave functions.

The non-confining contribution to the non-forward  $T$ -matrix element in the small- $\chi$  limit (2.6.3),

$$T_{nc}^{NP}(s_0, t) = \frac{2is_0}{9} \int d^2 b_\perp e^{i\vec{q}_\perp \cdot \vec{b}_\perp} \int dz_1 d^2 r_1 \int dz_2 d^2 r_2 |\psi_1(z_1, \vec{r}_1)|^2 |\psi_2(z_2, \vec{r}_2)|^2 (\chi_{nc}^{NP})^2, \quad (\text{D.0.4})$$

becomes analogously

$$T_{nc}^{NP}(s_0, t) = \frac{8is_0}{9} \left( \frac{\pi^2 G_2 (1 - \kappa)}{24} \right)^2 \int \frac{d^2 k_\perp}{(2\pi)^2} i\tilde{D}'^{(2)}(k_\perp^2) i\tilde{D}'^{(2)}((\vec{k}_\perp + \vec{q}_\perp)^2) \quad (\text{D.0.5})$$

$$\times \int_0^1 dz_1 \int_0^1 dz_2 \left[ H_1(z_1^2 q_\perp^2) - H_1((z_1 \vec{q}_\perp + \vec{k}_\perp)^2) \right] \left[ H_2(z_2^2 q_\perp^2) - H_2((z_2 \vec{q}_\perp + \vec{k}_\perp)^2) \right]$$

with  $H_{1,2}$  defined in (D.0.3).

For  $t = -q_\perp^2 \neq 0$ , both contributions (D.0.2) and (D.0.5) depend on the shape of the  $z_i$ -distribution of the wave function, i.e., for the Gaussian hadron wave function (B.1.1), the contributions depend on the width  $\Delta z_h$ . This  $\Delta z_h$ -dependence is transferred to the differential elastic cross section  $d\sigma^{el}/dt(s, t)$  given in (5.4.1) and its local slope  $B(s, t)$  given in (5.3.1). At  $t = 0$ , the dependence on the shape of the  $z_i$ -distribution of the wave functions disappears because of the normalization of the  $z_i$ -distribution as can be seen immediately from (D.0.3). Therefore, in our model the total cross sections – related via the optical theorem to the forward ( $t = 0$ )  $T$ -matrix element – do not depend on the parameter that characterize the  $z_i$ -distribution of the wave function.

# Bibliography

- [1] K. G. Wilson, Phys. Rev. D **10** (1974) 2445.
- [2] H. J. Rothe, World Sci. Lect. Notes Phys. **59** (1997) 1.
- [3] D. E. Groom *et al.* [Particle Data Group], Eur. Phys. J. C **15** (2000) 1.
- [4] C. Adloff *et al.* [H1 Collaboration], Nucl. Phys. B **497** (1997) 3;  
C. Adloff *et al.* [H1 Collaboration], Eur. Phys. J. C **19** (2001) 269;  
J. Breitweg *et al.* [ZEUS Collaboration], Phys. Lett. B **407** (1997) 432;  
J. Breitweg *et al.* [ZEUS Collaboration], Phys. Lett. B **487** (2000) 53.
- [5] C. Adloff *et al.* [H1 Collaboration], Eur. Phys. J. C **21** (2001) 33.
- [6] J. Breitweg *et al.* [ZEUS Collaboration], Z. Phys. C **75** (1997) 215;  
C. Adloff *et al.* [H1 Collaboration], Phys. Lett. B **483** (2000) 23.
- [7] M. Froissart, Phys. Rev. **123** (1961) 1053;  
A. Martin, Phys. Rev. **129** (1963) 1432; Nuovo Cim. A **42** (1965) 930;  
L. Lukaszuk and A. Martin, Nuovo Cim. A **47** (1967) 265.
- [8] A. I. Shoshi, F. D. Steffen and H. J. Pirner, Nucl. Phys. A **709** (2002) 131.
- [9] F. J. Wegner, J. Math. Phys. **12** (1971) 2259.
- [10] O. Nachtmann, Annals Phys. **209** (1991) 436.
- [11] O. Nachtmann, in “Perturbative and Nonperturbative Aspects of Quantum Field Theory”, edited by H. Latal and W. Schweiger (Springer Verlag, Berlin, Heidelberg 1997) [hep-ph/9609365].
- [12] A. Krämer and H. G. Dosch, Phys. Lett. B **252** (1990) 669.
- [13] H. G. Dosch, E. Ferreira and A. Krämer, Phys. Rev. D **50** (1994) 1992.
- [14] E. R. Berger and O. Nachtmann, Eur. Phys. J. C **7** (1999) 459.

- [15] I. Arefeva, *Theor. Math. Phys.* **43** (1980) 353;  
 N. E. Bralic, *Phys. Rev. D* **22** (1980) 3090;  
 P. M. Fishbane, S. Gasiorowicz and P. Kaus, *Phys. Rev. D* **24** (1981) 2324;  
 L. Diosi, *Phys. Rev. D* **27** (1983) 2552;  
 Y. A. Simonov, *Sov. J. Nucl. Phys.* **48** (1988) 878 [*Yad. Fiz.* **48** (1988) 1381].
- [16] H. G. Dosch, *Phys. Lett. B* **190** (1987) 177;  
 H. G. Dosch and Y. A. Simonov, *Phys. Lett. B* **205** (1988) 339;  
 Y. A. Simonov, *Nucl. Phys. B* **307** (1988) 512.
- [17] A. I. Shoshi, F. D. Steffen, H. G. Dosch and H. J. Pirner, “Confining QCD Strings, Casimir Scaling, and a Euclidean Approach to High-Energy Scattering,” arXiv:hep-ph/0211287.
- [18] M. Rueter and H. G. Dosch, *Phys. Lett. B* **380** (1996) 177;  
 H. G. Dosch, T. Gousset, G. Kulzinger and H. J. Pirner, *Phys. Rev. D* **55** (1997) 2602;  
 M. Rueter and H. G. Dosch, *Phys. Rev. D* **57** (1998) 4097;  
 G. Kulzinger, H. G. Dosch and H. J. Pirner, *Eur. Phys. J. C* **7** (1999) 73.
- [19] H. G. Dosch, T. Gousset, G. Kulzinger and H. J. Pirner, *Phys. Rev. D* **55** (1997) 2602.
- [20] H. G. Dosch, T. Gousset and H. J. Pirner, *Phys. Rev. D* **57** (1998) 1666.
- [21] M. Rueter, *Eur. Phys. J. C* **7** (1999) 233.
- [22] U. D’Alesio, A. Metz and H. J. Pirner, *Eur. Phys. J. C* **9** (1999) 601.
- [23] H. G. Dosch, O. Nachtmann, T. Paulus and S. Weinstock, *Eur. Phys. J. C* **21** (2001) 339.
- [24] A. Di Giacomo and H. Panagopoulos, *Phys. Lett. B* **285** (1992) 133;  
 A. Di Giacomo, E. Meggiolaro and H. Panagopoulos, *Nucl. Phys. B* **483** (1997) 371;  
 M. D’Elia, A. Di Giacomo and E. Meggiolaro, *Phys. Lett. B* **408** (1997) 315;  
 G. S. Bali, N. Brambilla and A. Vairo, *Phys. Lett. B* **421** (1998) 265.
- [25] E. Meggiolaro, *Phys. Lett. B* **451** (1999) 414.
- [26] G. S. Bali, *Phys. Rept.* **343** (2001) 1.
- [27] H. G. Dosch, M. Eidemüller and M. Jamin, *Phys. Lett. B* **452** (1999) 379.

- [28] A. Donnachie and P. V. Landshoff, Phys. Lett. B **437** (1998) 408;  
 A. Donnachie and P. V. Landshoff, “New data and the hard pomeron,” hep-ph/0105088.
- [29] A. Donnachie and P. V. Landshoff, Phys. Lett. B **296** (1992) 227.
- [30] L. Del Debbio, A. Di Giacomo and Y. A. Simonov, Phys. Lett. B **332** (1994) 111.
- [31] M. Rueter and H. G. Dosch, Z. Phys. C **66** (1995) 245.
- [32] S. Deldar, Phys. Rev. D **62** (2000) 034509.
- [33] G. S. Bali, Phys. Rev. D **62** (2000) 114503.
- [34] F. E. Low, Phys. Rev. D **12** (1975) 163;  
 S. Nussinov, Phys. Rev. Lett. **34** (1975) 1286.
- [35] J. F. Gunion and D. E. Soper, Phys. Rev. D **15** (1977) 2617.
- [36] A. H. Mueller, Nucl. Phys. B **415** (1994) 373.
- [37] A. H. Mueller and B. Patel, Nucl. Phys. B **425** (1994) 471.
- [38] N. N. Nikolaev and B. G. Zakharov, Phys. Lett. B **332** (1994) 177;  
 A. Szczerba, N. N. Nikolaev, W. Schafer and J. Speth, Phys. Lett. B **500** (2001) 254.
- [39] J. Nemchik, N. N. Nikolaev, E. Predazzi, B. G. Zakharov and V. R. Zoller, J. Exp. Theor. Phys. **86** (1998) 1054.
- [40] E. A. Kuraev, L. N. Lipatov and V. S. Fadin, Sov. Phys. JETP **45** (1977) 199;  
 I. I. Balitsky and L. N. Lipatov, Sov. J. Nucl. Phys. **28** (1978) 822.
- [41] M. Ciafaloni, Nucl. Phys. B **296** (1988) 49;  
 S. Catani, F. Fiorani and G. Marchesini, Phys. Lett. B **234** (1990) 339.
- [42] V. N. Gribov and L. N. Lipatov, Yad. Fiz. **15** (1972) 781;  
 L. N. Lipatov, Sov. J. Nucl. Phys. **20** (1975) 94;  
 G. Altarelli and G. Parisi, Nucl. Phys. B **126** (1977) 298;  
 Y. L. Dokshitzer, Sov. Phys. JETP **46** (1977) 641.
- [43] A. A. Migdal, Phys. Rept. **102** (1983) 199.
- [44] M. Wirbel, B. Stech and M. Bauer, Z. Phys. C **29** (1985) 637.
- [45] J. Ambjorn, P. Olesen and C. Peterson, Nucl. Phys. B **240** (1984) 533.

- [46] K. Kallio and H. D. Trottier, “Adjoint ‘quarks’ on coarse anisotropic lattices: Implications for string breaking in full QCD,” hep-lat/0001020.
- [47] N. G. Van Kampen, *Physica* **74** (1997) 215, 239;  
 N. G. Van Kampen, *Phys. Rep.* **C24** (1976) 172;  
 A. Y. Dubin and Y. S. Kalashnikova, *Phys. Atom. Nucl.* **58** (1995) 1967 [*Yad. Fiz.* **58** (1995) 2078].
- [48] M. Rueter and H. G. Dosch, *Z. Phys. C* **66** (1995) 245.
- [49] A. Di Giacomo, H. G. Dosch, V. I. Shevchenko and Y. A. Simonov, “Field correlators in QCD: Theory and applications,” hep-ph/0007223.
- [50] P. Cvitanovic, “Group Theory, part I,” Nordita Classics Illustrated (1984); see also <http://www.nbi.dk/GroupTheory/Welcome.html>.
- [51] J. Häkkinen and H. Kharraziha, *Comput. Phys. Commun.* **100** (1997) 311 [arXiv:hep-ph/9603229].
- [52] Y. A. Simonov, *Phys. Atom. Nucl.* **58** (1995) 107.
- [53] V. I. Shevchenko and Y. A. Simonov, *Phys. Lett. B* **437** (1998) 131.
- [54] V. I. Shevchenko and Y. A. Simonov, *Phys. Rev. D* **66** (2002) 056012.
- [55] A. Di Giacomo and E. Meggiolaro, “On the dependence of the gauge-invariant field-strength correlators in QCD on the shape of the Schwinger string,” hep-lat/0203012.
- [56] M. A. Shifman, A. I. Vainshtein and V. I. Zakharov, *Nucl. Phys. B* **147** (1979) 385;  
 M. A. Shifman, A. I. Vainshtein and V. I. Zakharov, *Nucl. Phys. B* **147** (1979) 448.
- [57] E. Meggiolaro, *Z. Phys. C* **76** (1997) 523; *Eur. Phys. J. C* **4** (1998) 101; *Nucl. Phys. B* **625** (2002) 312.
- [58] A. I. Shoshi, F. D. Steffen, H. G. Dosch and H. J. Pirner, *Phys. Rev. D* **66** (2002) 094019.
- [59] L. S. Brown and W. I. Weisberger, *Phys. Rev. D* **20** (1979) 3239.
- [60] J. B. Kogut, *Rev. Mod. Phys.* **51** (1979) 659, Sec. VI.
- [61] For a review on heavy quarkonium phenomenology, see e.g. W. Kwong, J. L. Rosner and C. Quigg, *Ann. Rev. Nucl. Part. Sci.* **37** (1987) 325.

[62] P. Goddard, J. Goldstone, C. Rebbi and C. B. Thorn, Nucl. Phys. B **56** (1973) 109;  
 K. Johnson and C. B. Thorn, Phys. Rev. D **13** (1976) 1934.

[63] V. I. Shevchenko and Y. A. Simonov, Phys. Rev. Lett. **85** (2000) 1811.

[64] V. I. Shevchenko and Y. A. Simonov, “On Casimir Scaling in QCD,” hep-ph/0104135.

[65] D. Chen, R. C. Brower, J. W. Negele and E. V. Shuryak, Nucl. Phys. Proc. Suppl. **73** (1999) 512.

[66] S. Gusken, Nucl. Phys. Proc. Suppl. **63** (1998) 16;  
 S. Aoki *et al.* [CP-PACS Collaboration], Nucl. Phys. Proc. Suppl. **73** (1999) 216.

[67] A. I. Shoshi, F. D. Steffen and H. J. Pirner, “Gluon saturation and S-matrix unitarity,” arXiv:hep-ph/0205343.

[68] M. Lüscher and P. Weisz, JHEP **0207** (2002) 049.

[69] N. N. Nikolaev and B. G. Zakharov, Z. Phys. C **49** (1991) 607.

[70] B. Z. Kopeliovich, I. K. Potashnikova, B. Povh and E. Predazzi, Phys. Rev. D **63** (2001) 054001.

[71] K. Golec-Biernat and M. Wüsthoff, Phys. Rev. D **59** (1999) 014017;

[72] K. Golec-Biernat and M. Wüsthoff, Phys. Rev. D **60** (1999) 114023.

[73] J. R. Forshaw, G. Kerley and G. Shaw, Phys. Rev. D **60** (1999) 074012.

[74] A. Donnachie and H. G. Dosch, Phys. Rev. D **65** (2002) 014019.

[75] E. A. Kuraev, L. N. Lipatov and V. S. Fadin, Sov. Phys. JETP **45** (1977) 199 [Zh. Eksp. Teor. Fiz. **72** (1977) 377];  
 I. I. Balitsky and L. N. Lipatov, Sov. J. Nucl. Phys. **28** (1978) 822 [Yad. Fiz. **28** (1978) 1597].

[76] U. D’Alesio, A. Metz and H. J. Pirner, Eur. Phys. J. C **9** (1999) 601.

[77] W. Magnus, F. Oberhettinger and R. P. Soni, “Formulas and Theorems for the Special Functions of Mathematical Physics,” 3rd edition, edited by B. Eckmann and B. L. van der Werden (Springer Verlag, Berlin, Heidelberg, New York 1996).

[78] S. Wolfram, “The Mathematica Book,” 4th edition, edited by G. Beck, J. Grehens and J. Walsh (Wolfram Research Inc., Cambridge University Press, 1999).

[79] H. Abramowicz and A. Caldwell, Rev. Mod. Phys. **71** (1999) 1275; J. Breitweg *et al.* [ZEUS Collaboration], Eur. Phys. J. C **7** (1999) 609; C. Adloff *et al.* [H1 Collaboration], Eur. Phys. J. C **21** (2001) 33.

[80] E. Laermann, C. DeTar, O. Kaczmarek and F. Karsch, Nucl. Phys. Proc. Suppl. **73** (1999) 447.

[81] S. Catani, M. Ciafaloni and F. Hautmann, Phys. Lett. B **242** (1990) 97; Nucl. Phys. B **366** (1991) 135.

[82] N. N. Nikolaev and B. G. Zakharov, Phys. Lett. B **332** (1994) 184.

[83] B. Blaettel, G. Baym, L. L. Frankfurt and M. Strikman, Phys. Rev. Lett. **70** (1993) 896.

[84] N. N. Nikolaev and B. G. Zakharov, Phys. Lett. B **332** (1994) 184; L. Frankfurt, W. Koepf and M. Strikman, Phys. Rev. D **54** (1996) 3194.

[85] I. P. Ivanov and N. N. Nikolaev, Phys. Rev. D **65** (2002) 054004.

[86] E. Iancu, A. Leonidov and L. McLerran, “The Colour Glass Condensate: An Introduction,” hep-ph/0202270.

[87] M. Glück, E. Reya and A. Vogt, Eur. Phys. J. C **5** (1998) 461.

[88] J. Bartels, K. Golec-Biernat and H. Kowalski, Phys. Rev. D **66** (2002) 014001.

[89] J. Blümlein, “On the  $k_\perp$  dependent gluon density of the proton,” hep-ph/9506403.

[90] H. Jung, “CCFM prediction on forward jets and F2: Parton level predictions and a new hadron level Monte Carlo generator CASCADE,” hep-ph/9908497; H. Jung and G. P. Salam, Eur. Phys. J. C **19** (2001) 351.

[91] M. A. Kimber, A. D. Martin and M. G. Ryskin, Phys. Rev. D **63** (2001) 114027.

[92] B. Andersson, G. Gustafson and J. Samuelsson, Nucl. Phys. B **467** (1996) 443; B. Andersson, G. Gustafson and H. Kharraziha, Phys. Rev. D **57** (1998) 5543.

[93] G. Gustafson, L. Lonnblad and G. Miu, “Gluon Distribution Functions in the  $k_\perp$ -Factorization Approach,” hep-ph/0206195.

[94] B. Anderson *et al.* [Small x Collaboration], “Small x Phenomenology: Summary and Status,” hep-ph/0204115.

[95] J. Kwiecinski, A. D. Martin and A. M. Stasto, Phys. Rev. D **56** (1997) 3991.

[96] M. G. Ryskin and Y. M. Shabelski, Z. Phys. C **66** (1995) 151.

[97] U. Amaldi, M. Jacob and G. Matthiae, Ann. Rev. Nucl. Part. Sci. **26** (1976) 385.

[98] R. Castaldi and G. Sanguinetti, Ann. Rev. Nucl. Part. Sci. **33** (1983) 351.

[99] L. Van Hove, Rev. Mod. Phys. **36** (1964) 655.

[100] L. Frankfurt, V. Guzey, M. McDermott and M. Strikman, Phys. Rev. Lett. **87** (2001) 192301;  
L. Frankfurt, V. Guzey, M. McDermott and M. Strikman, “Electron nucleus collisions at THERA,” hep-ph/0104252.

[101] P. Desgrolard, L. Jenkovszkii, and B. Struminsky, Eur. Phys. J. C **11** (1999) 144.

[102] L. Lukaszuk and A. Martin, Nuovo Cim. A **52** (1967) 122.

[103] W. Heisenberg, Z. Phys. 133 (1952) 65.

[104] E. Ferreiro, E. Iancu, K. Itakura and L. McLerran, Nucl. Phys. A **710** (2002) 373.

[105] H. G. Dosch, P. Gauron and B. Nicolescu, “Heisenberg’s universal  $\ln^{**2}(s)$  increase of total cross sections,” arXiv:hep-ph/0206214.

[106] A. D. Martin and M. G. Ryskin, Phys. Lett. B **431** (1998) 395;  
J. Bartels, K. Golec-Biernat and K. Peters, Eur. Phys. J. C **17** (2000) 121.

[107] L. V. Gribov, E. M. Levin and M. G. Ryskin, Phys. Rept. **100** (1983) 1.

[108] A. H. Mueller and J. Qiu, Nucl. Phys. B **268** (1986) 427.

[109] A. D. Martin, R. G. Roberts and W. J. Stirling, Phys. Rev. D **37** (1988) 1161.

[110] A. M. Cooper-Sarkar, G. Ingelman, K. R. Long, R. G. Roberts and D. H. Saxon, Z. Phys. C **39** (1988) 281;  
A. M. Cooper-Sarkar, R. C. Devenish and M. Lancaster, “Measurement of  $F_L(x, Q^2)$  at low  $x$ , and extraction of the gluon distribution,” in 1992 Proc. Workshop on Physics at HERA vol. 1 (1991) p. 155, ed. W. Buchmüller and G. Ingelman.

[111] A. H. Mueller, Nucl. Phys. B **558** (1999) 285.

- [112] E. Iancu and L. D. McLerran, Phys. Lett. B **510** (2001) 145.
- [113] E. Gotsman, E. Ferreira, E. Levin, U. Maor and E. Naftali, Phys. Lett. B **500** (2001) 87.
- [114] S. Munier, “Dipole proton S-matrix derived from diffractive meson electroproduction,” arXiv:hep-ph/0111454.
- [115] H. Abramowicz and A. Caldwell, Rev. Mod. Phys. **71** (1999) 1275.
- [116] L. D. McLerran and R. Venugopalan, Phys. Rev. D **49** (1994) 2233;  
 L. D. McLerran and R. Venugopalan, Phys. Rev. D **49** (1994) 3352;  
 A. Ayala, J. Jalilian-Marian, L. D. McLerran and R. Venugopalan, Phys. Rev. D **53** (1996) 458.
- [117] J. Jalilian-Marian, A. Kovner and H. Weigert, Phys. Rev. D **59** (1999) 014015;  
 J. Jalilian-Marian, A. Kovner, A. Leonidov and H. Weigert, Phys. Rev. D **59** (1999) 014014;  
 J. Jalilian-Marian, A. Kovner, A. Leonidov and H. Weigert, Nucl. Phys. B **504** (1997) 415;  
 J. Jalilian-Marian, A. Kovner, L. D. McLerran and H. Weigert, Phys. Rev. D **55** (1997) 5414.
- [118] E. Iancu, A. Leonidov and L. D. McLerran, Nucl. Phys. A **692** (2001) 583;  
 E. Ferreiro, E. Iancu, A. Leonidov and L. McLerran, “Nonlinear gluon evolution in the color glass condensate. II,” hep-ph/0109115.
- [119] A. Capella, E. G. Ferreiro, C. A. Salgado and A. B. Kaidalov, Phys. Rev. D **63** (2001) 054010;  
 A. Capella, E. G. Ferreiro, C. A. Salgado and A. B. Kaidalov, Nucl. Phys. B **593** (2001) 336.
- [120] A. Donnachie, H. G. Dosch and M. Rueter, Eur. Phys. J. C **13** (2000) 141.
- [121] G. Abbiendi *et al.* [OPAL Collaboration], Eur. Phys. J. C **14** (2000) 199;  
 M. Acciarri *et al.* [L3 Collaboration], Phys. Lett. B **519** (2001) 33.
- [122] R. M. Baltrusaitis *et al.*, Phys. Rev. Lett. **52** (1984) 1380;  
 T. K. Gaisser, U. Sukhatme and G. B. Yodh, Phys. Rev. D **36** (1987) 1350.
- [123] M. Honda *et al.*, Phys. Rev. Lett. **70** (1993) 525;  
 N. N. Nikolaev, Phys. Rev. D **48** (1993) 1904.
- [124] M. M. Block, E. M. Gregores, F. Halzen and G. Pancheri, Phys. Rev. D **60** (1999) 054024.

[125] V. M. Budnev, A. N. Vall and V. V. Serebryakov, *Yad. Fiz.* **21** (1975) 1033.

[126] U. Amaldi and K. R. Schubert, *Nucl. Phys. B* **166** (1980) 301.

[127] R. Castaldi and G. Sanguinetti, *Ann. Rev. Nucl. Part. Sci.* **33** (1983) 351.

[128] D. Schildknecht, B. Surrow and M. Tentyukov, *Mod. Phys. Lett. A* **16** (2001) 1829.

[129] P. Gauron and B. Nicolescu, *Phys. Lett. B* **486** (2000) 71;  
 B. Nicolescu, *Nucl. Phys. Proc. Suppl.* **99A** (2001) 47;  
 J. R. Cudell *et al.*, *Phys. Rev. D* **65** (2002) 074024.

[130] A. C. Benvenuti *et al.* [BCDMS Collaboration], *Phys. Lett. B* **223** (1989) 485;  
 M. Arneodo *et al.* [New Muon Collaboration], *Nucl. Phys. B* **483** (1997) 3;  
 M. R. Adams *et al.* [E665 Collaboration], *Phys. Rev. D* **54** (1996) 3006.

[131] S. Aid *et al.* [H1 Collaboration], *Nucl. Phys. B* **470** (1996) 3;  
 C. Adloff *et al.* [H1 Collaboration], *Nucl. Phys. B* **497** (1997) 3.

[132] M. Derrick *et al.* [ZEUS Collaboration], *Z. Phys. C* **69** (1996) 607;  
 M. Derrick *et al.* [ZEUS Collaboration], *Z. Phys. C* **72** (1996) 399;  
 J. Breitweg *et al.* [ZEUS Collaboration], *Phys. Lett. B* **407** (1997) 432.

[133] D. O. Caldwell *et al.*, *Phys. Rev. Lett.* **40** (1978) 1222;  
 M. Derrick *et al.* [ZEUS Collaboration], *Z. Phys. C* **63** (1994) 391;  
 S. Aid *et al.* [H1 Collaboration], *Z. Phys. C* **69** (1995) 27.

[134] I. Abt *et al.* [H1 Collaboration], *Nucl. Phys. B* **407** (1993) 515;  
 T. Ahmed *et al.* [H1 Collaboration], *Nucl. Phys. B* **439** (1995) 471.

[135] M. Derrick *et al.* [ZEUS Collaboration], *Phys. Lett. B* **316** (1993) 412;  
 M. Derrick *et al.* [ZEUS Collaboration], *Z. Phys. C* **65** (1995) 379.

[136] U. Amaldi *et al.*, *Phys. Lett. B* **36** (1971) 504;  
 U. Amaldi *et al.*, *Phys. Lett. B* **66** (1977) 390;  
 M. Ambrosio *et al.* [CERN-Naples-Pisa-Stony Brook Collaboration], *Phys. Lett. B* **115** (1982) 495;  
 N. Amos *et al.*, *Phys. Lett. B* **128** (1983) 343;  
 N. Amos *et al.*, *Nucl. Phys. B* **262** (1985) 689;  
 N. A. Amos *et al.* [E710 Collaboration], *Phys. Rev. Lett.* **61** (1988) 525;  
 V. D. Apokin *et al.*, *Sov. J. Nucl. Phys.* **25** (1977) 51;  
 V. Bartenev *et al.*, *Phys. Rev. Lett.* **29** (1972) 1755;  
 G. G. Beznogikh *et al.*, *Nucl. Phys. B* **54** (1973) 78;

A. Breakstone *et al.* [AMES-BOLOGNA-CERN-DORTMUND-HEIDELBERG-WARSAW COLLABORATION Collaboration], Nucl. Phys. B **248** (1984) 253;  
 R. E. Breedon *et al.* [UA6 Collaboration], Phys. Lett. B **216** (1989) 459;  
 C. Bromberg, T. Ferbel, T. Jensen and P. Slattery, Phys. Rev. D **15** (1977) 64;  
 J. P. Burq *et al.*, Phys. Lett. B **109** (1982) 124;  
 R. L. Cool, K. Goulianos, S. L. Segler, H. Sticker and S. N. White, Phys. Rev. D **24** (1981) 2821;  
 N. Amos *et al.*, Phys. Rev. Lett. **47** (1981) 1191.

[137] M. Bozzo *et al.* [UA4 Collaboration], Phys. Lett. B **147** (1984) 385.

[138] N. A. Amos *et al.* [E710 Collaboration], Phys. Rev. Lett. **63** (1989) 2784.

[139] N. A. Amos *et al.* [E-710 Collaboration], Phys. Lett. B **243** (1990) 158.

[140] M. Fukugita and J. Kwiecinski, Phys. Lett. B **83** (1979) 119.

[141] A. Donnachie and P. V. Landshoff, Nucl. Phys. B **231** (1984) 189; Phys. Lett. B **123** (1983) 345.

[142] L. Lukaszuk and B. Nicolescu, Lett. Nuovo Cim. **8** (1973) 405;  
 K. Kang and B. Nicolescu, Phys. Rev. D **11** (1975) 2461.

[143] M. Rueter, H. G. Dosch and O. Nachtmann, Phys. Rev. D **59** (1999) 014018.

[144] H. G. Dosch, C. Ewerz and V. Schatz, “The odderon in high energy elastic p-p scattering,” hep-ph/0201294.

[145] G. Barbiellini *et al.*, Phys. Lett. B **39** (1972) 663;  
 G. Giacomelli and M. Jacob, Phys. Rept. **55** (1979) 1.

[146] C. W. Akerlof *et al.*, Phys. Rev. D **14** (1976) 2864;  
 R. Rubinste in *et al.*, Phys. Rev. D **30** (1984) 1413.

[147] E. Berger, “Diffractive high energy scattering in nonperturbative QCD,” PhD thesis, Heidelberg University (1999).

[148] A. Hebecker, E. Meggiolaro and O. Nachtmann, Nucl. Phys. B **571** (2000) 26;  
 O. Nachtmann, “Effective field theory approach to structure functions at small x(Bj),” hep-ph/0206284.

[149] H. J. Pirner, Phys. Lett. B **521** (2001) 279;  
 H. J. Pirner and F. Yuan, Phys. Rev. D **66** (2002) 034020.

[150] J. D. Bjørken and S. D. Drell, “Relativistic Quantum Mechanics,” *McGraw-Hill, New York (1964)*; J.D.Bjørken and S. D. Drell, “Relativistic Quantum Fields.” *McGraw-Hill, New York (1965)*.

[151] M. E. Peskin and D. V. Schroeder, “An Introduction to quantum field theory,” *Reading, USA: Addison-Wesley (1995) 842 p.*

[152] G. P. Lepage and S. J. Brodsky, Phys. Rev. D **22** (1980) 2157.

[153] H. G. Dosch, M. Jamin and B. Stech, Z. Phys. C **42**, 167 (1989).

[154] T. Schäfer, E. V. Shuryak and J. J. Verbaarschot, Nucl. Phys. B **412** (1994) 143.

[155] J. D. Bjorken, J. B. Kogut and D. E. Soper, Phys. Rev. D **3** (1971) 1382; G. P. Lepage and S. J. Brodsky, Phys. Rev. D **22** (1980) 2157.

[156] T. H. Bauer, R. D. Spital, D. R. Yennie and F. M. Pipkin, Rev. Mod. Phys. **50** (1978) 261 [Erratum-ibid. **51** (1978) 407].

[157] V. Y. Petrov, P. V. Pobylitsa, M. V. Polyakov, I. Bornig, K. Goeke and C. Weiss, Phys. Rev. D **57** (1998) 4325.

[158] A. D. Martin, M. G. Ryskin and A. M. Stasto, Nucl. Phys. Proc. Suppl. **74** (1999) 121; Eur. Phys. J. C **7** (1999) 643.

# Acknowledgments

First of all, I would like to express my gratitude to my adviser Professor Hans-Jürgen Pirner for suggesting this work to me, for numerous stimulating and insightful discussions, for constant supervision and patient guidance, and for supporting me to give talks at several conferences. His insightful advices have been essential for the successful accomplishment of this research work. I appreciate very much the friendly atmosphere in the Theory Group of Professor Pirner.

Next, I wish to thank Professor Jörg Hüfner for his interest in my work, for sharing his views, for willingness to referee this thesis, and for taking part in the oral examination. Special thanks to him for organizing the fridays “tee meeting”, to his wife for preparing the delicious cakes, and to both for the tasty dinner and the enjoyable evening at their home.

I want to thank Professor Hans-Günter Dosch for numerous discussions, his advice, and the fruitful collaboration.

I am grateful to Dr. habil. Hilmar Forkel for several insightful discussions on physics and other topics.

I want to express my gratitude to Dr. Yuri Ivanov for his continual support in computational issues. Without Yuri’s help most of the formulas of this thesis could not have been turned into numbers. I was lucky to share the office with Yuri.

Now, I come to two colleagues and good friends of mine: Alberto Polleri and Frank Steffen. Alberto earns special thanks for the discussions about the physics, for the invitation to his extremely good organized marriage, for the delicious dinner at his home, for the nice time in New York, and particularly for the fun we had outside of the physics in Heidelberg. The friendship with Frank started after some time of close scientific collaboration. Special thanks to Frank for this close and fruitful collaboration. I wish to thank him also for the numerous discussions during lunch, for the donated photos made during the holidays in Corsica, and for the really good time which we had during the last three years.

Kai Schwenzer deserves a special thank since he took me to the student’s cafeteria on my first day in Heidelberg and offered to me the first coffee in this city. I will never forget the fun we had in Cargese.

I also thank Jörg Raufiesen, Alberto Accardi, and Yuan Feng for interesting discussions, Carlo Ewerz and Otto Nachtmann for suggestions which have helped me

in finding the right perspective in many cases, and Stephane Munier for discussions and proof-reading of the abstract and introduction of the thesis. Sonja Bartsch, Carnelia Merkel, and Melanie Steiert earn gratitude for the administrative support, the careful reading of the manuscript, and the friendly atmosphere which they create in the institute.

I want to thank my parents and brothers in a very special way for their support, care, love, and advice. They are extremely important in my life.

Finally, I am very thankful to my love, Hava, for all the wonderful moments, for her support, and especially for her love. She is of particular importance in my life.